Available online at www.sciencedirect.com
ScienceDirect
Geochimica et Cosmochimica Acta 71 (2007) 95–128
Geochimica
www.elsevier.com/locate/gca

Natural speciation of Ni, Zn, Ba, and As in ferromanganese coatings on quartz using X-ray fluorescence, absorption, and diffraction

Alain Manceau *, Martine Lanson, Nicolas Geoffroy

Environmental Geochemistry Group, LGIT, University Joseph Fourier and CNRS, 38041 Grenoble Cedex 9, France

Received 22 May 2006; accepted in revised form 22 August 2006

Abstract

The mineralogy of natural ferromanganese coatings on quartz grains and the crystal chemistry of associated trace elements Ni, Zn, Ba, and As were characterized by X-ray microfluorescence, X-ray diffraction, and EXAFS spectroscopy. Fe is speciated as ferrihydrite and Mn as vernadite. The two oxides form alternating Fe- and Mn-rich layers that are irregularly distributed and not always continuous. Unlike naturally abundant Fe–vernadite, in which Fe and Mn are mixed at the nanoscale, the ferrihydrite and vernadite are physically segregated and the trace elements clearly partitioned at the microscopic scale. Vernadite consists of two populations of interstratified one-water layer (7 Å phyllomanganate) and two-water layer (10 Å phyllomanganate) crystallites. In one population, 7 Å layers dominate, and in the other 10 Å layers dominate. The three trace metals Ni, Zn, and Ba are associated with vernadite and the metalloid As with ferrihydrite. In vernadite, nickel is both substituted isomorphically for Mn in the manganese layer and sorbed at vacant Mn layer sites in the interlayer. The partitioning of Ni is pH-dependent, with a strong preference for the first site at circumneutral pH and for the second at acidic pH. Thus, the site occupancy of Ni in vernadite may be an indicator of marine vs. continental origin, and in the latter, of the acidity of streams, lakes, or soil pore waters in which the vernadite formed. Zinc is sorbed only in the interlayer at vacant Mn layer sites. It is fully tetrahedral at a Zn/Mn molar ratio of 0.0138, and partly octahedral at a Zn/Mn ratio of 0.1036 consistent with experimental studies showing that the $^{VI}Zn/^{IV}Zn$ ratio increases with Zn loading. Barium is sorbed in a slightly offset position above empty tetrahedral cavities in the interlayer. Arsenic tetrahedra are retained at the ferrihydrite surface by a bidentate-binuclear attachment to two adjacent iron octahedra, as commonly observed. Trace elements in ferromanganese precipitates are partitioned at a few, well-defined, crystallographic sites that have some elemental specificity, and thus selectivity. The relative diversity of sorption sites contrasts with the simplicity of the layer structure of vernadite, in which charge deficit arises only from Mn^{4+} vacancies (i.e., no Mn^{3+} for Mn^{4+} substitution). Therefore, sorption mechanisms primarily depend on physical and chemical properties of the sorbate and competition with other ions in solution, such as protons at low pH for Ni sorption.

1. Introduction

Ferromanganese precipitates, in the form of veins, dendrites, crusts, nodules, concretions, fine grained aggregates, mottles, mineral coatings, and rock varnish, are ubiquitous at the planet's surface (Post, 1999). These precipitates are enriched in trace metal(loid)s (TMs) by many orders of magnitude relative to crustal averages, and have long been recognized as the 'scavengers of the environment' (Goldberg, 1954; Jenne, 1968; Chao and Theobald, 1976; Hudson-Edwards, 2000). A key problem in environmental geochemistry is to determine how TMs are partitioned among and structurally bound to constitutive Fe and Mn (oxyhydr)oxides (hereafter referred to as 'oxides'). Typically, trace elements are incorporated preferentially in one phase due to a conjunction of geochemical, physico-chemical, and structural factors, some being unique to this class of minerals. These factors include the chemical form of the dissolved element (i.e., oxidation state, aqueous speciation), the solution pH and ionic strength, the presence of competitive adsorbates, the contact time, and the crystallographic nature of the sorption site. Geochemical partitioning is the rule regardless of the parameter(s) that control

* Corresponding author. Fax: +33 4 76 82 81 01.
E-mail address: Alain.Manceau@obs.ujf-grenoble.fr (A. Manceau).

0016-7037/$ - see front matter © 2006 Elsevier Inc. All rights reserved.
doi:10.1016/j.gca.2006.08.036

the sorption behavior of the element. Thus, elements that prefer Mn oxides, such as Co, Ni, and Ba can be distinguished from those that prefer Fe oxides, such as V, As, and U. Other TMs such as Cu, Zn, Pb, and Mo, occur in both phases (Nowlan, 1976; Li, 1982; Palumbo et al., 2001; Vaniman et al., 2002; Koschinsky and Hein, 2003; Kuhn et al., 2003; Manceau et al., 2003; Tani et al., 2003; Neaman et al., 2004). How dissolved metal speciation may lead to preferential sorption onto the solid phase is illustrated with the example of lead. Lead is associated with Mn oxides in continental ferromanganese nodules thought to originate from freshwater in which Pb^{2+}(aq) is the dominant species (McKenzie, 1989; Liu et al., 2002; Neaman et al., 2004). In contrast, lead is taken up by both Mn and Fe oxides in marine ferromanganese deposits (Bargar et al., 1998; Byrne, 2002; Koschinsky and Hein, 2003), formed in seawater settings where the dominant lead species are $PbCl^{+}$, $Pb(CO_3)_2^{2-}$, and $PbCO_3^{\circ}$.

Our knowledge of how TMs are partitioned among ferromanganese oxides and other phases in natural systems relies mostly on chemical extractions, in which differences in solubility of solid phases in contact with complexants (e.g. oxalate, citrate) or reductants (e.g. dithionite, hydroxylamine hydrochloride, and ascorbic acid) are used to determine which TMs are associated with which phases (Schwertmann and Pfab, 1994; Trolard et al., 1995; Koschinsky and Hein, 2003; Neaman et al., 2004). This approach has many shortcomings, including incomplete dissolution of target phases, dissolution of nontarget species, and potential redistribution of elemental species among remaining minerals in the sample (Taylor and McKenzie, 1966; McCarty et al., 1998; Ostergren et al., 1999; Gilmore et al., 2001). Alternatively, instrumental microchemical techniques, including scanning transmission electron microscopy (STEM), particle induced X-ray emission (PIXE), and synchrotron-based X-ray radiation fluorescence (SXRF), have been used to determine directly chemical associations at the nanometer to micrometer scale in undisturbed or minimally disturbed samples (Przybylowicz et al., 2001; Manceau et al., 2002b; Sutton et al., 2002; Jeong and Lee, 2003; Utsunomiya et al., 2003). Microprobe applications to trace element geochemistry have been increasing, due to the demand for characterization of environmental samples and the parallel rise in number of nuclear, X-ray and electron elemental mapping capabilities. At this point in time, As–Fe, Ni–Mn, Zn–Mn, Ba–Mn, and Ce–Mn associations, among others, have been imaged with these techniques, and for some elemental associations, statistically significant correlation coefficients have been calculated from the fluorescence information in pixelized elemental maps (Morin et al., 1999, 2001; Duff et al., 2001; Hansel et al., 2001; Hlawatsch et al., 2001; Isaure et al., 2002, 2005; Manceau et al., 2002c, 2003, 2004, 2005; Roberts et al., 2002; Strawn et al., 2002; Vaniman et al., 2002; Marcus et al., 2004b; Voegelin et al., 2005; Kirpichtchikova et al., 2006; van Oort et al., 2006). The large number of spot analyses in a two-dimensional array allows evaluation of not only the covariance of two elements with better precision than with chemical extractions, but also the variability of the ratios of TMs to major element (ME) in the calculation of the correlation coefficient. For example, if the sample contains two populations of the TMs–ME pair with distinct values of the TMs/ME ratio, then the correlation coefficient calculated from microchemical analyses will be one for each population. In contrast, chemical analyses will 'see' only one average population with a large dispersion of the TMs/ME ratios. Thus, any correlation that may exist in a heterogeneous sample containing several chemical populations or species is underestimated by bulk chemical analysis, and may become completely obscured. A spuriously low correlation coefficient may lead to the false conclusion that TMs are associated with more phases than are real.

Once the carrier phases are known, the next step is to determine how they bind TMs at the molecular scale. Extended X-ray absorption fine structure (EXAFS) spectroscopy is indisputably the technique of choice for probing the local atomic environment of TMs in solid matrices. In the last two decades, a plethora of data has been acquired on the sorption mechanism of TMs to model minerals (Brown and Sturchio, 2002), and this vast knowledge base helps investigations of the forms of TMs in real-world systems (Manceau et al., 2002b). In particular, the uptake mechanism of TMs on two-line ferrihydrite (2LFh), the main TMs-bearing Fe phase in ferromanganese precipitates, is well documented. Three main types of complexes have been identified: edge-sharing (EC), double-corner sharing (DC) and single-corner sharing (SC), in proportions that depend on the nature of the sorbate ion, its concentration at the sorbent surface (i.e., surface coverage), and the solution chemistry. Surface complexes can be identified from the EXAFS-derived TM–Fe distance because it increases in the order EC–DC–SC (Charlet and Manceau, 1992; Manceau and Charlet, 1992; Bargar et al., 1997; Spadini et al., 1994). There are two principal motives to structurally resolving the configuration of surface complexes on natural samples. One is that metal stability and partitioning among co-existing phases depend on their binding environment (Peacock and Sherman, 2004). The second is that knowing the type of TMs linkage in natural solids may help design optimized sorbents for remediating the environment.

The polyhedral description of the bonding mechanism of TMs on mineral surfaces also has been applied to minerals from the birnessite family (i.e., buserite, rancieite, vernadite, and birnessite), which are the main TMs-bearing Mn phases in ferromanganese precipitates. All birnessites have a layer structure and a negative layer charge, which is compensated by cation sorption in the interlayer. The symmetry of the manganese layer can be hexagonal or orthogonal (Drits et al., 1997). Birnessites with hexagonal layer symmetry are the most common in nature (Glover, 1977; Bardossy and Brindley, 1978; Chukhrov et al.,

1985; Duff et al., 1999; Bilinski et al., 2002; Manceau et al., 2003, 2004, 2005; Buatier et al., 2004; Marcus et al., 2004b), and they have a structural charge arising predominantly from Mn vacancies and, occasionally from Mn^{3+} for Mn^{4+} substitutions, in the octahedral layer (Chukhrov et al., 1985; Silvester et al., 1997; Lanson et al., 2000; Ertl et al., 2005). Hexagonal birnessites tend to sorb hydrolyzable cations in their interlayer, and retain them at vacancy sites to compensate local charge. When the sorbed cation is too big to enter the octahedral cage (e.g., $^{VI}Zn^{2+}$, $^{VI}Co^{2+}$), or is coordinated tetrahedrally (e.g., $^{IV}Zn^{2+}$), it stays in the interlayer and bonds with the three undersaturated oxygens from the octahedral vacancy, forming a triple corner-sharing complex (TC) (Silvester et al., 1997; Manceau et al., 2000, 2002a, 2003; Leroux et al., 2001; Matocha et al., 2001; Lanson et al., 2002b; Marcus et al., 2004b; Isaure et al., 2005; Toner et al., 2006). If the surface species is octahedral and its size matches the octahedral cage (e.g., Cr^{3+}, Co^{3+}), then it may enter the Mn vacancy site (Manceau and Charlet, 1992; Manceau et al., 1997). Like any lamellar compound, birnessites have variable surface charge from unsaturated ligands (i.e., O atoms) at layer edges. Poorly crystallized birnessites, which are ubiquitous at the earth's surface, have a small size (as low as a few tens of nanometers; Villalobos et al., 2006) and, consequently, a large surface area-to-volume ratio. For these birnessites, such as vernadite (δ-MnO_2), edge sites hold a relatively high proportion of the total particle charge, and thus contribute significantly to ion sorption capacity (Manning et al., 2002; Tournassat et al., 2002; Foster et al., 2003; Villalobos et al., 2005). These publications show that, similarly to ferrihydrite, most of our knowledge on the uptake mechanism of TMs at the birnessite surface has been acquired on model systems. Little is known on the nature of reactive sites and binding environment of TMs in natural specimens.

This work is part of a larger research project aimed at determining how TMs are sequestered at the molecular level in continental settings and marine deposits, with primary emphasis on ferromanganese precipitates, the main sink for TMs. Here, focus is placed on the structural chemistry of metal(loid)s-containing ferrihydrite and vernadite formed naturally at the surface of quartz grains from sand filters used in groundwater treatment plants. These samples were chosen because oxide-coated silica sand commonly is used for water purification due to its high hydraulic conductivity and low cost (e.g., Cheremisinoff, 1995; Bose et al., 2002; Babel and Kurniawan, 2003; Qureshi and Nelson, 2003; Vaishya and Gupta, 2003; Hu et al., 2004a,b) and studied in the laboratory especially for application in household arsenic removal systems (Thirunavukkarasu et al., 2001, 2003; Bose and Sharma, 2002; Yuan et al., 2002; Vaishya and Gupta, 2004; Gupta et al., 2005; Jessen et al., 2005; Kundu and Gupta, 2005; Leupin and Hug, 2005; Newcombe et al., 2006). Fundamental understanding of the structure of the sorbent phases and of the partitioning and retention mechanisms of toxic elements (here, Ni, Zn, As, and Ba, an analogue for Ra) should benefit the design and use of engineered field systems. In addition, dark oxide-coatings on sediment particles in streambeds and aquifers are common and usually enriched in trace elements (Carpenter et al., 1975; Robinson, 1993; Larsen and Postma, 1997; Hudson-Edwards, 2000; Tani et al., 2003). Although such Fe and Mn oxide coatings are some of the most important substrates in the uptake and release of trace metals in surficial waters, they have not been well characterized because they are generally mixed at the nanometer scale. We studied five samples with a large range of Fe/Mn atomic ratio (83.11–0.34) and trace element contents (Table 1) using microfocused X-ray beams which allowed us to sample their chemical heterogeneity, in particular the natural enrichment of Fe and Mn in distinct spatial regions.

The distributions of Ni, Zn, Ba, and As in the sand coatings were imaged by μ-SXRF, to visualize the TMs–Fe and TMs–Mn associations. When the TM/ME ratio was heterogeneous in a single grain, or between grains, μ-EXAFS spectra were taken at points-of-interest (POIs) on the Fe–Mn elemental maps to determine directly the chemical forms of the TM in microsized areas, and to characterize the species heterogeneity in the sample. The average speciation of the four TMs and the nature of the dominant species in mixtures were determined by powder EXAFS spectroscopy.

2. Materials and methods

2.1. Samples

Sand filtration is widely used in North Germany to remove Fe, Mn, and TMs from ground waters. The sand samples were collected from five water works near the cities of Dresden (2SP), Saarbrücken (3SP), Emden (4SP), Lüneburg (5SP), and Karlsruhe (6KR) and oven-dried at mild temperature (40 °C) to not remove structural water. The coatings were detached from the quartz cores by gentle crushing in an agate mortar. The <20 μm fraction was extracted by sieving for chemical, X-ray diffraction and spectroscopic analyses. Thirty-micrometer thick micropolished thin sections of unperturbed quartz grains were prepared for μ-SXRF analysis.

2.2. Chemical analysis

The samples were ignited at 1000 °C with Na metaborate, then dissolved with concentrated HCl. The resulting solutions were analyzed for major and trace elements by inductively coupled plasma-atomic emission spectrometry (ICP-AES, Jobin-Yvon JY 70) and -mass spectrometry (ICP-MS, Perkin-Elmer ELAN 6000), respectively, at the C.R.P.G. (Centre de Recherches Pétrographiques et Géochimiques) analytical laboratory in Nançy, France (Table 1). The cationic composition of the phyllomanga-

Table 1
Chemical composition on a weight basis of sand coatings from several German water works

Origin	Code name	Na_2O (%)	MgO (%)	Al_2O_3 (%)	SiO_2 (%)	P_2O_5 (%)	K_2O (%)	CaO (%)	TiO_2 (%)	MnO (%)	Fe_2O_3 (%)	CoO (ppm)	NiO (ppm)	CuO (ppm)	ZnO (ppm)	As_2O_5 (ppm)	BaO (ppm)	PbO (ppm)	IL[a] %	Total (%)
Dresden	2SP	0.04	0.49	0.50	6.91	0.26	0.22	3.82	b.d.	35.79	30.39	495	578	36	1130	324	3610	1	21.3	100.3
Saarbrücken	3SP	0.04	0.77	0.42	8.38	4.39	0.20	2.69	0.02	35.90	20.79	1450	3300	327	63600	673	11200	21	20.7	102.3
Emden	4SP	b.d.	0.13	b.d.	5.87	1.30	b.d.	1.70	b.d.	0.58	53.47	2	8	b.d.	10	11	349	3	33.2	96.3
Lüneburg	5SP	b.d.	0.22	0.03	5.15	4.62	b.d.	4.63	b.d.	8.50	44.38	3	8	b.d.	34	34	1430	3	30.1	97.8
Karlsruhe	6KR	0.16	0.97	1.20	3.18	0.40	0.12	5.72	b.d.	45.23	16.93	299	571	120	7450	8670	3730	b.d.	23.9	99.8

The standard deviation is lower than 5% for all elements.
b.d., below detection limit.
[a] Loss on ignition at 1000 °C.

nate interlayer (excluding Mn^{2+}) in 2SP, 3SP and 6KR was measured by selectively dissolving the MnO_2 component from the ferromanganese matrix, and analyzing the solution by ICP-AES (Table 2). The MnO_2 was dissolved completely, along with a minor amount of the Fe oxides, by reacting 5 mg of sample with 15 mL of 0.7 mol/L hydroxylammonium chloride (NH_3OHCl, pH 1.9) for one minute. The solution was filtered on a 0.22 μm cellulose acetate membrane, acidified with 5 mL of 10% HNO_3, and diluted with bidistilled water to a total volume of 50 mL for analysis. Selectivity was assessed by comparing the Fe/Mn molar ratios in the initial solid and in the extraction solution. Only 4% (2SP), 10% (6KR), and 11% (3SP) of the initial amounts of Fe were dissolved by this procedure (Table 2).

2.3. Model compounds

The reference materials used for interpreting the Zn-, As-, and Ba-EXAFS data are either pure mineral species or synthetic sorption samples, whose synthesis has been described previously. Their code names and the references of the articles in which they are described are given in the Section 3. Two series of Ni sorbed δ-MnO_2 surrogates were prepared for this study because in previous work on the natural speciation of TMs Ni was associated with lithiophorite, not birnessite. Since lithiophorite has no vacant Mn layer sites, but birnessite does, the possibility of Ni sorption at vacancy sites in the interlayer of phyllomanganates could not be evaluated with the first species. The Na-exchanged δ-MnO_2 used for Ni sorption was prepared according to Villalobos et al. (2003). The δ-MnO_2 suspension was stored at 5 °C for several days in hydrated state at the synthesized solid concentration (21.7 g/L) in polypropylene containers before use. Nickel was sorbed by dropwise addition (0.4 mL/min) of a 5×10^{-4} M $Ni(NO_3)_2$ solution (pH 4) to a rapidly stirred δ-MnO_2 suspension (2 g/L) pre-equilibrated at pH 4 or 7 with an automatic titrator. Samples were prepared at 25 °C in an Ar–gas-saturated solution at constant ionic strength (0.1 mol/L $NaNO_3$). All solutions were prepared from deionized water that had been boiled to remove dissolved CO_2(g), and $[Ni]_{aq}$ in the suspensions was always below the solubility limit of known pure Ni (hydr)oxides. After 12 h of equilibration, the solid was filtered on a 0.1 μm cellulose nitrate membrane, washed with deionized water to prevent the precipitation of metal salt, and freeze-dried. Eight samples were prepared at pH 4 and 7 and variable Ni surface loading. Total Ni and Mn concentrations in the solids were determined by ICP-AES (Perkin-Elmer Optima 3300DV) after dissolution of the dried solids in 10% NH_3OHCl. The pH-4 series has Ni/Mn molar ratios of 0.0023 (NidBi2-4), 0.0107 (NidBi11-4), 0.0499 (NidBi50-4), and 0.1055 (NidBi105-4). The Ni/Mn ratios for the pH-7 series are 0.0025 (NidBi2-7), 0.0107 (NidBi11-7), 0.0565 (NidBi56-7), and 0.1775 (NidBi177-7).

Table 2
Composition of the interlayer of the phyllomanganate species (molar ratios) from selective dissolution analyses

Sample	Na/Mn	K/Mn	Mg/Mn	Ca/Mn	Ba/Mn	Zn/Mn	Fe/Mn-dissolved[a]	Fe/Mn bulk[b]
2SP	0.0047	0.0074	0.0109	0.1373	0.0047	0.0031	0.0326	0.77
3SP	0.0047	0.0064	0.0202	0.0729	0.0143	0.1036	0.0569	0.52
6KR	0.0105	0.0068	0.0266	0.1613	0.0046	0.0138	0.0325	0.34

Ni was not analyzed. The standard deviation on molar ratios is 4.2%.
[a] Fe/Mn molar ratio in the extraction solution.
[b] Fe/Mn molar ratio in the initial solid (calculated from values in Table 1).

2.4. X-ray diffraction

All XRD patterns were recorded at ambient condition with a Bruker D5000 diffractometer equipped with a Cu anode and a Kevex Si(Li) solid state detector. The XRD patterns of samples 2SP, 3SP, and 6KR, which contain higher amounts of Mn, were recorded also *in situ* at 80, 120, and 150 °C in an Anton Paar TTK450 chamber attached to the diffractometer. Samples were heated for two hours before recording the XRD trace. All diffractograms were recorded from 5° to 80° 2θ (i.e., 17.7–1.20 Å in *d*-spacing), 0.04° 2θ step size, and 40 s counting time. The diffuse maximum at about 5.2 Å in all *in situ* patterns is due to X-ray scattering from the sample holder.

2.5. μ-SXRF

The X-ray fluorescence maps were obtained on beamline 10.3.2 at the advanced light source (ALS), Berkeley (Marcus et al., 2004a). The distributions of Mn, Fe, and TMs were imaged by scanning the thin-sections under a monochromatic beam. The incident energy was set at 11.917 keV (i.e., 50 eV above the As K-edge) for 6KR, 10 keV (i.e., 341 eV above the Zn K-edge) for 2SP and 5SP, and 10 and 5250 keV (Ba L_3-edge + 3 eV) for 3SP. The X-ray fluorescence lines were recorded with a seven-element Ge solid-state detector and a counting time of 100–150 ms per pixel. The FWHM beam size and step size were 5 μm (H) × 5 μm (V) and 8–10 μm (H) × 8–10 μm (V) for 2SP, 3SP, and 6KR, and 16 μm (H) × 7 μm (V) and 20 μm (H) × 20 μm (V) for 4SP and 5SP, respectively.

2.6. EXAFS spectroscopy

All Ba L_3-edge EXAFS spectra (sample and references) were recorded on beamline 10.3.2. Several Ni, Zn and As K-edge μ-EXAFS spectra at POIs selected from the μ-SXRF maps also were recorded on 10.3.2 for samples 3SP (Ni and Zn) and 6KR (Zn and As). The average speciation of the three elements, and the spectra from the Ni references, were recorded by bulk EXAFS spectroscopy on beamline FAME at the European synchrotron radiation facility (ESRF) in Grenoble, France (spot size 300 × 150 μm) (Proux et al., 2006). The EXAFS data analysis was carried out using the codes from the WinXAS package (Ressler, 1998). Briefly, the experimental χ(k) EXAFS function was obtained after subtracting the embedded-atom absorption background from the fluorescence-yield signal normalized to the intensity of the incident beam (*I*0), and normalizing the signal by the absorption edge step. EXAFS spectra were Fourier transformed with a Bessel apodization function to real (*R*) space, and backtransformed to *k* space for spectral simulation using phase shifts and amplitude functions calculated by FEFF v.7 (Ankudinov and Rehr, 1997). Multicomponent EXAFS spectra were analyzed by principal component analysis (PCA) and reconstructed with the spectra from pure TMs species (Manceau et al., 2002b).

3. Results

3.1. Chemical composition

Except for 3SP, which is extremely rich in Zn (5.1 wt%) and Ba (1.0 wt%), major elements (>1 wt%) in the sand coatings are Mn (0.45–35.0 wt%), Fe (11.8–37.4 wt%), Si (1.5–3.9 wt%), and Ca (1.2–4.1 wt%) (Table 1). XRD analysis showed that the Si content of at least 2SP and 3SP is overestimated due to contamination by quartz splinters when detaching the Fe–Mn coatings. Qualitative correlation was observed between the Fe/Mn ratio and the optical color of the coated sand, which gradually evolved from brown-black to orange with increasing Fe/Mn. The range in TMs composition is broad and the concentrations of TMs are not proportional to Mn, Fe, or Mn + Fe, both of which probably reflect the variability in composition of the filtered waters. For example, 3SP contains the highest amounts of Ni, Cu, Zn, Ba, and Pb, but has relatively little Fe and is the second richest Mn sample after 6KR. On the other hand, 2SP, which has more Fe and similar Mn as 3SP, is low in TMs.

Samples 2SP, 3SP, and 6KR are the richest in Mn, and also in phyllomanganates (see XRD section), which have foreign cations in their interlayers (Table 2). The Ca/Mn molar ratios measured in solution after dissolution of the Mn oxide (0.1373 in 2SP, 0.073 in 3SP, and 0.161 in 6KR) are similar to the bulk values (0.098, 0.069, and 0.116, respectively), indicating a strong Ca–Mn association. Calcium is likely the dominant interlayer species in 2SP and 6KR, but not in 3SP in which Zn is more abundant. In all samples, Ca prevails over Na + K + Mg, as expected for phyllomanganates of continental origin (Taylor et al., 1964; Glover, 1977; Chukhrov et al., 1980, 1985; McKenzie, 1989; Usui et al., 1997;

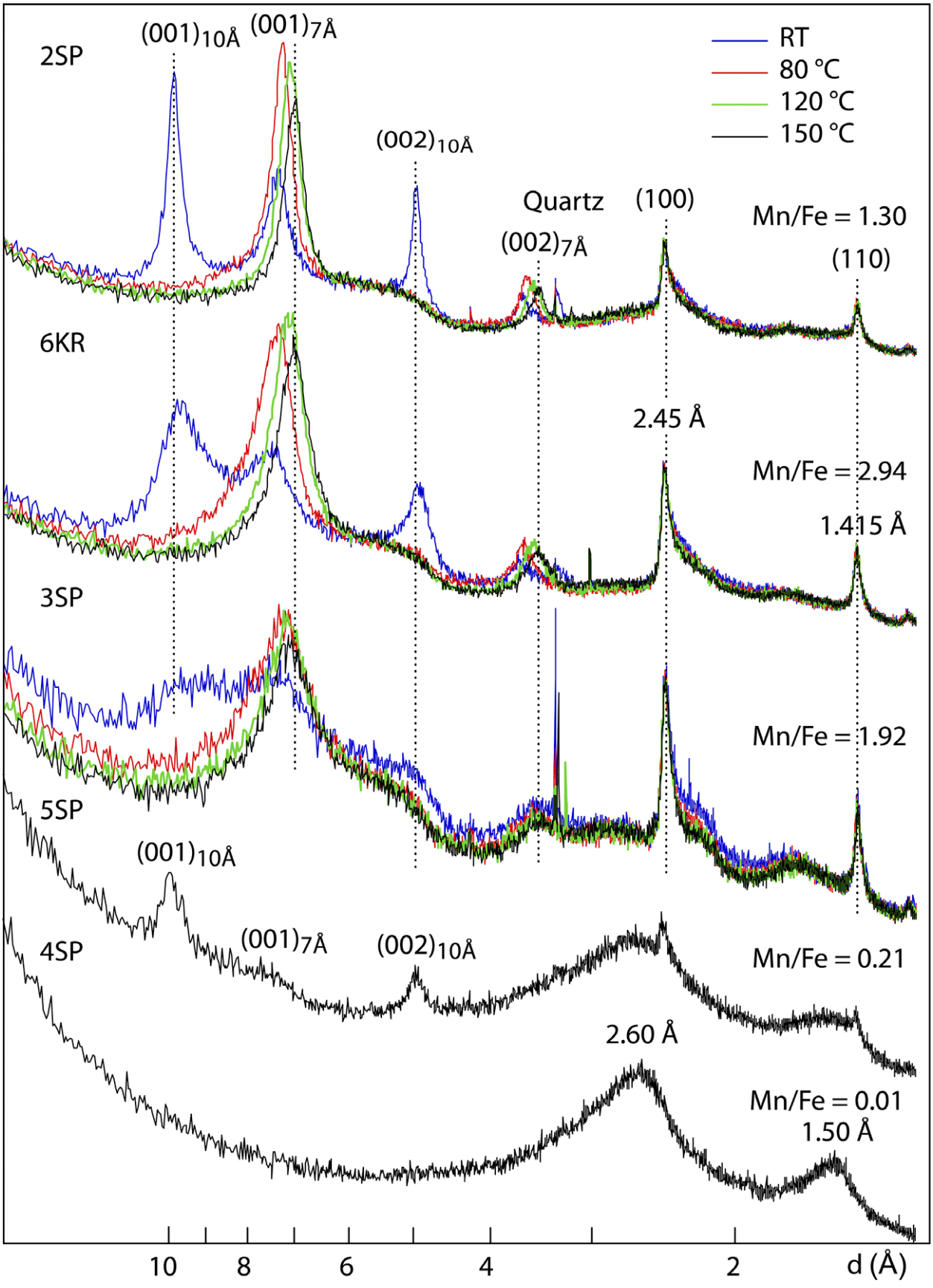
2SP
(001)10Å
(001)7Å
(002)10Å
Quartz
(100)
(002)7Å
(110)
RT
80 °C
120 °C
150 °C
Mn/Fe = 1.30
6KR
2.45 Å
Mn/Fe = 2.94
1.415 Å
3SP
Mn/Fe = 1.92
5SP
(001)10Å
(001)7Å
(002)10Å
Mn/Fe = 0.21
4SP
2.60 Å
Mn/Fe = 0.01
1.50 Å
10
8
6
4
2
d (Å)

Bilinski et al., 2002). Since layer charge originates only from Mn^{4+} vacancies in the octahedral layer (no layer Mn^{3+}, see XRD results), a total of four positive charges are needed to balance the charge deficit created by one octahedral vacancy. Thus, the cationic (Ct) composition of the interlayers can be used to estimate the mole fraction of vacant Mn sites (X_{vac}): $X_{vac} = [\sum_i ([Ct^{n+}/Mn]/n)_i]/[1 + \sum_i ([Ct^{n+}/Mn]/n)_i]$. The X_{vac} values are 0.08 for 2SP, 0.10 for 3SP and 0.11 for 6KR. The proportions of vacant Mn sites derived from chemical analysis are minimum values, because interlayer Mn^{2+} could not be measured, and we know that this ion is often present (Lanson et al., 2000; Villalobos et al., 2006). The layer charge also may be balanced by protons, especially at low pH. Nonetheless, these values compare favorably with those reported for δ-MnO_2 synthesized by biogenic (0.167) and chemical routes (0.06 for dBi and 0.12 for its acid form) (Villalobos et al., 2006). The ratios of total interlayer cations (Na, K, Ca, Ba, and Zn) to Mn (0.157–0.202–0.197) are also consistent with values reported in the literature (1:6–1:7; Usui, 1979; Golden et al., 1986). However, the comparison is approximate because not all phyllomanganates have the same layer stoichiometry, and thus layer charge.

3.2. X-ray diffraction

The XRD trace of the Mn-depleted 4SP sample is characteristic of two-line ferrihydrite (2-Fh), with a broad hump at 2.60 Å asymmetrical on its low 2θ-angle (i.e., high *d*-spacing) side followed by a symmetrical broad band at 1.50 Å (Fig. 1). The asymmetry presumably results from nanometer hematite grains intimately mixed with the hydrous ferric oxide component of ferrihydrite (Drits et al., 1993, 1995). At a Mn/Fe molar ratio of 0.21 (5SP), the XRD trace still is dominated by ferrihydrite, but the 001 and 002 basal reflections at ~9.9 and ~4.9 Å from a two-water-layer (2W) phyllomanganate component and a faint 001 reflection at ~7.3 to 7.4 Å from a one-water-layer (1W) phyllomanganate component are present (Giovanoli et al., 1970, 1975; Giovanoli and Bürki, 1975; Usui and Mita, 1995). The two Mn oxide components prevail over ferrihydrite in 2SP and 3SP, and ferrihydrite is no longer detected in 6KR. XRD does not allow one to conclude whether the two Mn components coexist in the same particles or are physically segregated particles in a phase mixture (Ferrage et al., 2005). The high-angle asymmetrical 100 reflection (2.45 Å) and the 110 reflection (1.415 Å) from random stacked (turbostratic) birnessite are also detected in the Mn-rich samples (Giovanoli and Bürki, 1975; Holland and Walker, 1996). The ratio of the two *d*-spacings is $2.45/1.415 = 1.731 \sim \sqrt{3}$, which indicates that the birnessite layers have hexagonal symmetry with $a = b = 2.830$ Å (Drits et al., 1997). The low value of the layer-cell dimension is an indication that the layers do not contain Mn^{3+} (Manceau et al., 1997). As a comparison, synthetic hexagonal birnessite (HBi) equilibrated at pH 4 has 13% Mn^{3+} in its layer and a *b* parameter of 2.848 Å (Lanson et al., 2000).

The 2W, also denoted by buserite (Giovanoli et al., 1975), and 1W hydrates occur in all Mn samples, but important variations in peak position, intensity and width of the basal reflections are observed. The 9.9 and 7.2–7.3 Å reflections have almost the same widths in 3SP and in 6KR, but the first peak is about 50% narrower in 2SP. In contrast, the width of the two peaks increases, and their intensity decreases, from 2SP to 6KR to 3SP, meaning that the diffracting crystallites contain fewer layers along this sample series. On the basis of XRD calculations performed on phyllomanganates with variable crystallinity, the average number of layers in the diffracting crystallites may be as low as 2–3 in 3SP and as large as 8–10 in 2SP (Manceau et al., 1997; Lanson et al., 2002b; Villalobos et al., 2006).

Evidence for a finer scale of heterogeneity in the distribution of the two layer types comes from the position and symmetry of basal reflections at room temperature and after heating. In 2SP, *d*(001) and *d*(002) of the 2W component are almost rational (9.88 and 4.95 Å, respectively), and the 9.88 Å peak is almost symmetric, which means that the diffracting crystallites contain essentially one type of layer. In contrast, the two basal reflections of the 2W diffracting units are irrational in 6KR (9.67 Å and 4.93 Å), and even more so in 3SP (~9.4 and ~4.9 Å), and the 001 reflections are extremely asymmetrical on their high-angle side. In 6KR and 3SP, the 001 reflection of the 2W component is shifted in the direction of the 7 Å component. The irrationality and shift toward smaller *d* values of the 001 reflections, and their high-angle asymmetry, reveal random interstratification of 1W layers in the 2W component (Reynolds, 1989). The value of *d*(001) represents the interstratification domain and is located between 00*l* reflections of the end-member diffracting units. The exact position of *d*(001) depends on the relative proportions of the end-members. Since the 001 reflection is closer to 10 than 7 Å, the fraction of the 2W layer hydrates in the 2W component is higher than 50%. However, not all 2W diffracting units contain the same proportion of 1W layers, as seen by the tail of the 001 peaks of 6KR and 3SP towards smaller *d* spacings. In fact, the distribution of 2W and 1W layers in the 3SP particles is so broad, that the ~10 and ~7 Å reflections are almost merged. Note that the shifts of the ~10 Å reflections relative to their ideal position cannot be caused by the rising

Fig. 1. X-ray diffraction patterns of quartz coatings having different Mn/Fe ratios. The untreated phyllomanganate contains a two-water-layer (~10 Å) and a one-water-layer (~7 Å) component. The asymmetry of the 10 Å reflections on their right side (lower *d*-spacing; higher 2θ angles) and the asymmetry of the 7 Å reflections on their left side (higher *d*-spacing; lower 2θ angles) are evidence for a mixed-layering of 7 and 10 Å layers in each component. The scattering hump (3SP) and background (2S) to the left-side of the 100 reflection are due to ferrihydrite. The vertical dotted lines are at $d = 9.88$, 6.99, 4.95, 3.50, 2.45, and 1.415 Å.

slope of the Lorentz-polarization and structure factors in the low angle region of the diffractogram, because this effect shifts the low-angle reflections towards even smaller 2θ-angles (Drits and Tchoubar, 1990).

Upon heating, the removal of one water layer caused the ~10 Å reflection to shift to ~7 Å, a distance comparable to the van der Waals diameter of water (2.82 Å) (Usui and Mita, 1995). The ~7 Å reflection progressively collapsed from 7.35 to 7.36 Å to 7.0 Å (2SP, 6KR) and from 7.2 to 7.1 Å (3SP) as the thickness of the interlayers became more uniform. At 150 °C, the 001 and 002 reflections of the 1W component are commensurate (7.00 and 3.50 Å, respectively). Two hypotheses can be proposed for this evolution. The first is random interstratification of some 2W layers in the 1W component, similar to the 2W − 1W mixed-layering described above for the 2W component. The second is that a decrease in the density of water with temperature in the ~7 Å interlayer spaces leads to progressively shorter layer-to-layer distances in the diffracting crystallites, as reported recently for montmorillonite (Ferrage et al., 2005). Although this last effect may exist, it does not completely account for the data because the FWHM of the 001 reflection for the 1W component also decreases with d value, while the FWHM of the 002 reflection remains unchanged. This effect is characteristic of mixed-layering (Reynolds, 1989).

3.3. μ-SXRF

In the SXRF maps (Fig. 2), the presence of Fe and Mn is color-coded with green and blue, respectively. The dominant color in any image can be correlated with the Fe/Mn molar ratio measured by chemical analysis. Grains from 6KR, 3SP, and 2SP are dominantly blue, which is corroborated by Fe/Mn molar ratios of 0.34, 0.52, and 0.77, respectively. Grains from 5SP and 4SP are mostly green with minor blue layers (5SP) or spots (4SP), agreeing with the Fe/Mn ratio of 4.72 and

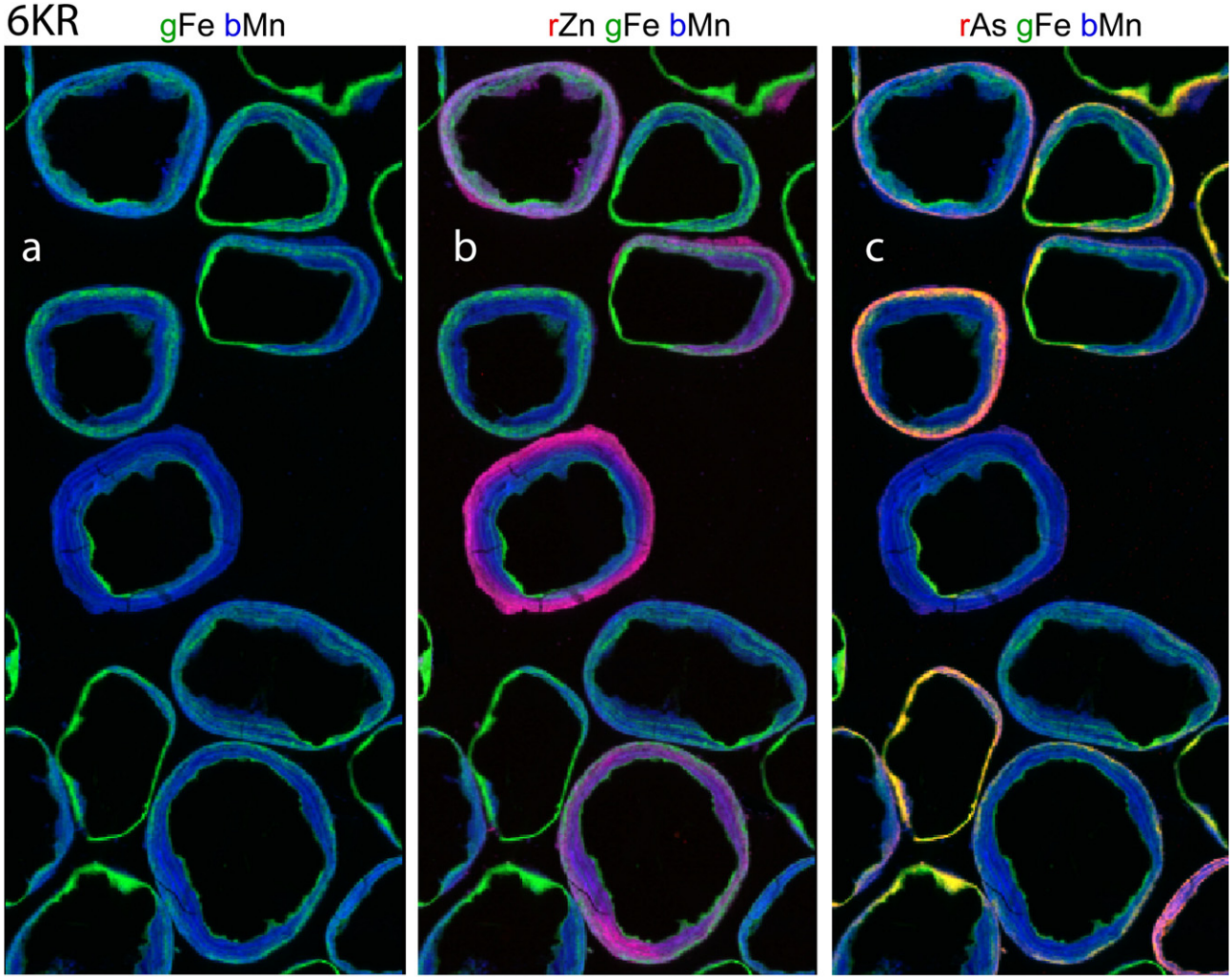

Fig. 2. Two-color (GB) and tricolor (RGB) μ-SXRF maps of quartz coatings. Red codes for trace elements, green for Fe, and blue for Mn. Each pixel is colored in proportion to the trace element Kα, Fe Kβ, and Mn Kα signals. 6KR, size = 2000 H × 4600 V μm^2; resolution 9 × 9 μm^2. 3SP left, size = 2100 H × 2200 V μm^2; resolution 10 × 10 μm^2. 3SP right, size = 1900 H × 1700 V μm^2; resolution 8 × 8 μm^2. 2SP, size = 3500 H × 1575 V μm^2; resolution 8 × 8 μm^2. 5SP, size = 6300 H × 3460 V μm^2, resolution 20 × 20 μm^2. 4SP, size = 4000 H × 3650 V μm^2; resolution 20 × 20 μm^2. H is horizontal (width) and V is vertical (height).

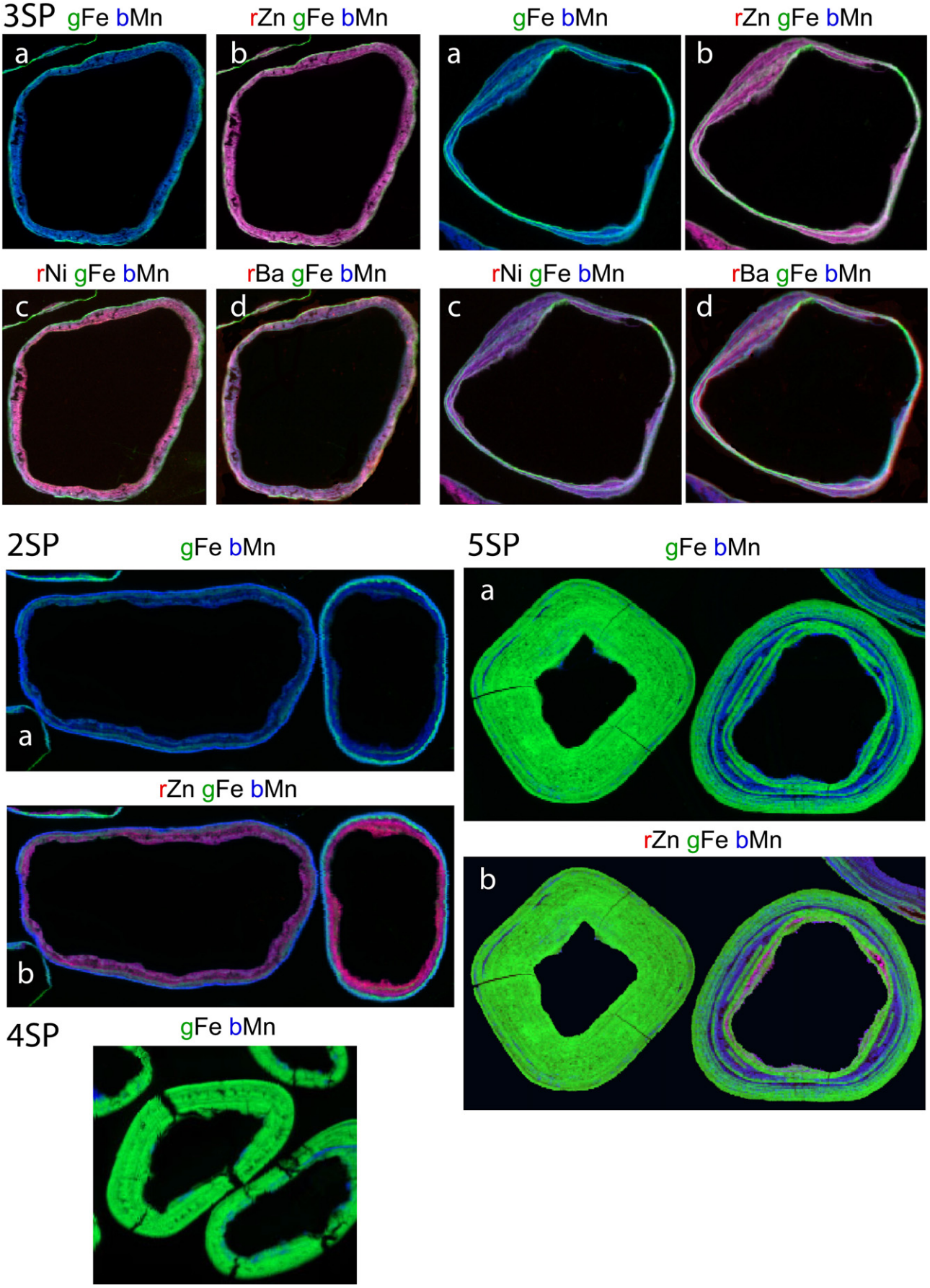

Fig. 2 (*continued*)

83.11. Although any sample is dominantly one color, its grains have different relative amounts of Fe and Mn, as indicated by the color distributions. The relative intensities of the Kα(Mn), Kβ(Mn) + Kα(Fe), and Kβ(Fe) X-ray fluorescence lines measured at grain-scale Fe- and Mn-rich spots were used to estimate Fe/Mn ratios by correcting the intensities for air absorption, Fe and Mn fluorescence yields, and taking $I(K\alpha)/I(K(\beta) = 100/17$. These ratios vary in the range 0.6–25 for 5SP, 0.25–15 for 6KR, 0.45–8 for 3SP, and 0.25–5 for 2SP, indicating that Fe can be more concentrated but is never completely separated from Mn. The richest Mn layers are in 6KR and 2SP. In some cases, Fe and Mn zones occur as alternating continuous layers over the sliced grain surface, and in other cases they are discontinuous laterally. The coatings also appear to have variable thickness. However, not all grains were cut through their equatorial plane, and if layer coverage is uniform, the apparent thickness will be higher for polar sections as seen for 5SP.

When red is added in proportion to the Zn(Kα) signal, some blue areas become violet, indicating a Mn–Zn association (Fig. 2b). When the Zn concentration is low, as in 6KR, 2SP, and 5SP, pure blue areas remain because the distribution of Zn is uneven. In contrast, Mn layers from the high-Zn 3SP sample are permeated with Zn, and the blue color disappears completely. However, even in this case the non-uniformity of the violet hue indicates variation in the Zn/Mn ratio. Distributions of Ba and Ni were recorded in 3SP. They are associated with Mn, also, but the variations in hue are more pronounced than for Zn. The truncated grain at the bottom left of the second map of 3SP has about three times more Ni than the grain at the center of the map, as estimated from the normalized $I(K\alpha)$ values.

Arsenic was imaged in 6KR. Most green layers turned yellow, with however large variations in hue, showing that As is associated with Fe oxides in varying As/Fe ratios. Some layers remained green, due to the absence or low concentration of As, and still other layers turned violet. The fluorescence intensities reveal that Fe and Mn are less separated in the violet areas than in other regions. The Mn(Kα):Fe(Kβ):As(Kα) proportions measured in bright yellow regions are typically 10:40:50, and those measured in the violet region at the lower right of the map are about 45:15:40. While the As signal is similar in the yellow and violet regions, the relative intensities of the Fe(Kβ) and Mn(Kα) signals are reversed, explaining the difference in color. In the violet regions, the Fe signal is weak enough to not visibly change the color. Thus, although As is sorbed on the Fe oxide in these regions, as shown by As K-edge micro-EXAFS spectroscopy, the viewer sees that As is associated with the Mn oxide. When looking at bi- or tri-color maps, it is important to realize that the color contribution from one element can overwhelm that from another, giving a false impression of elemental correlations. Also, just because two elements occur together is no guarantee that they are chemically linked.

3.4. Zn K-EXAFS

We know from the μ-SXRF data that Zn is associated typically with Mn, and from the XRD data that Mn is speciated as birnessite. Therefore, Zn is expected to reside on top of vacant sites in the phyllomanganate layers as observed in natural and synthetic Zn-containing birnessite (Silvester et al., 1997; Lanson et al., 2002b; Manceau et al., 2003; Li et al., 2004; Marcus et al., 2004b; Isaure et al., 2005) (Fig. 3). Zinc can be tetrahedral or octahedral at these sites, depending on the magnitude of the negative charge deficit, and on the type of layer stacking (Manceau et al., 2002a; Toner et al., 2006). EXAFS is highly sensitivity to Zn coordination because Zn undergoes a 20% decrease of its ionic radius when changing from octahedral to tetrahedral coordination. Therefore, the proportion of each complex can be determined with precision. An illustration is given in Fig. 4, which shows EXAFS spectra and FTs of chalcophanite ($^{VI}ZnMn_3O_7{\cdot}3H_2O$), a Zn phyllomanganate in which Zn is fully octahedral, and a

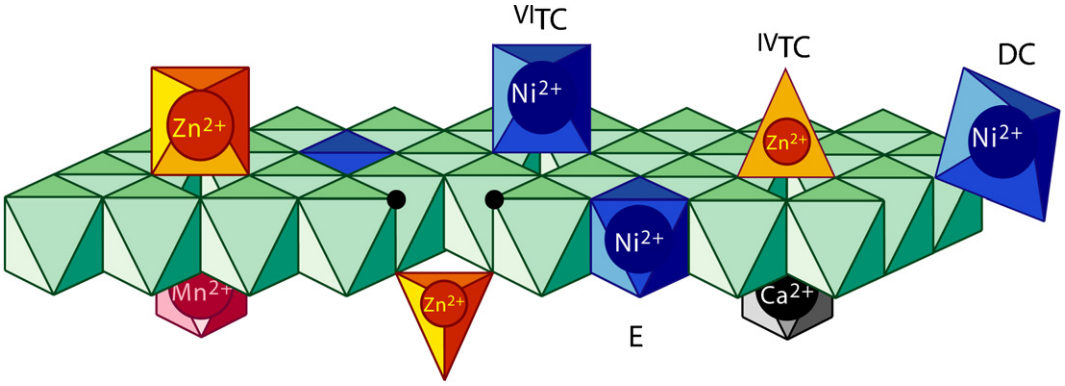

Fig. 3. Structural representation of the uptake mechanisms of Ni and Zn on natural hexagonal birnessite (δ-MnO_2) identified in this study. The residual layer charge deficit after the sorption of Ni and Zn on one side of a Mn^{4+} vacancy can be compensated by protons (small solid circles), calcium, or divalent manganese (Silvester et al., 1997). TC is a triple-corner sharing interlayer complex at the vacancy site, E is an edge-sharing layer complex resulting from isomorphic substitution at the Mn^{4+} layer site, and DC is a double-sharing surface complex at the layer edge.

natural turbostratic Zn-containing birnessite (^{IV}ZndBi) in which Zn is fully tetrahedral (Marcus et al., 2004b). There is a phase shift in both *k* and *R* space such that the functions from the tetrahedral complex have lower frequency in reciprocal *k* space and a shorter distance in real *R* space than chalcophanite. When Zn is in a mixed coordination state, the experimental phase varies linearly with the ^{IV}Zn/^{VI}Zn ratio.

Samples 3SP and 6KR were selected for Zn K-edge analysis because their Zn/Mn molar ratios differ by a factor of 7.5 which offers the opportunity to verify whether or not Zn coordination is a function of surface loading, as observed in the laboratory. Five μ-EXAFS spectra were recorded for each sample. All spectra within each sample are similar, probably because the Zn/Mn ratio varied by at most only a factor of two to three. Powder EXAFS spectra also were recorded and were not different from the point spectra for each sample. The powder spectra of 3SP and 6KR have the same lineshape, indicating that Zn occupies the same type of surface site in the two samples, but the frequencies are not exactly the same (Fig. 5a). The left side of the first oscillation, and the entire second oscillation of the 3SP spectrum are left-shifted, which indicates a substantial amount of octahedral Zn. The phase and shape of ^{IV}ZndBi match the 6KR data fairly well, whereas the ZnBi8 reference (Zn/Mn = 0.008), which has 30 ± 10% of its Zn in octahedral coordination with the rest tetrahedral (Manceau et al., 2002a), best matched the 3SP data (Fig. 5b and c). Thus, nearly all of the Zn is tetrahedral in the medium-Zn 6KR sample, and about 30% is octahedral in the high-Zn 3SP sample.

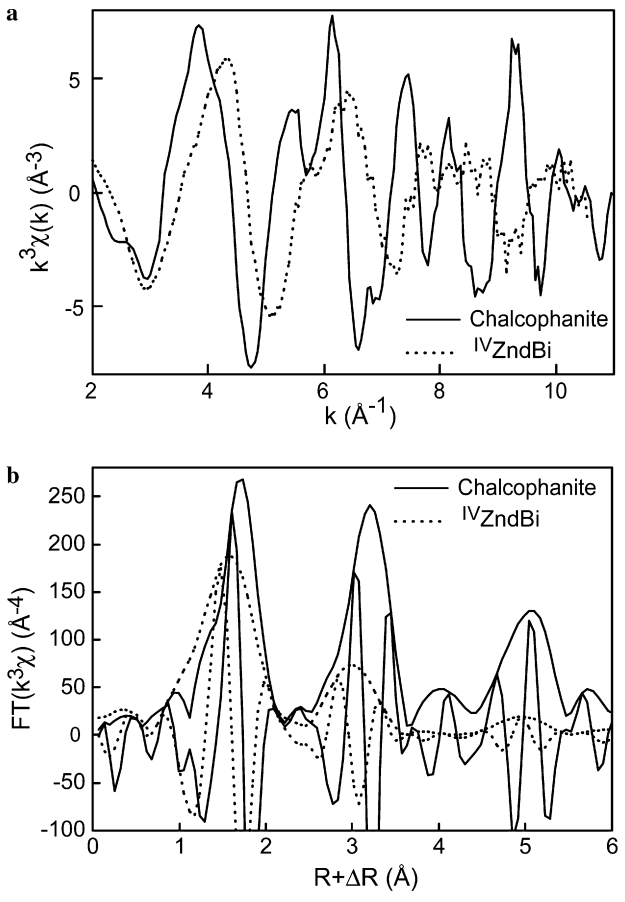

Fig. 4. (a) Zn K-edge EXAFS spectra and (b) modulus and imaginary part of the Fourier transforms (FTs) for two phyllomanganate references: chalcophanite ($^{VI}ZnMn_3O_7{\cdot}3H_2O$) and a natural vernadite (^{IV}ZndBi). The reference data are described in Manceau et al. (2002a) and Marcus et al. (2004b).

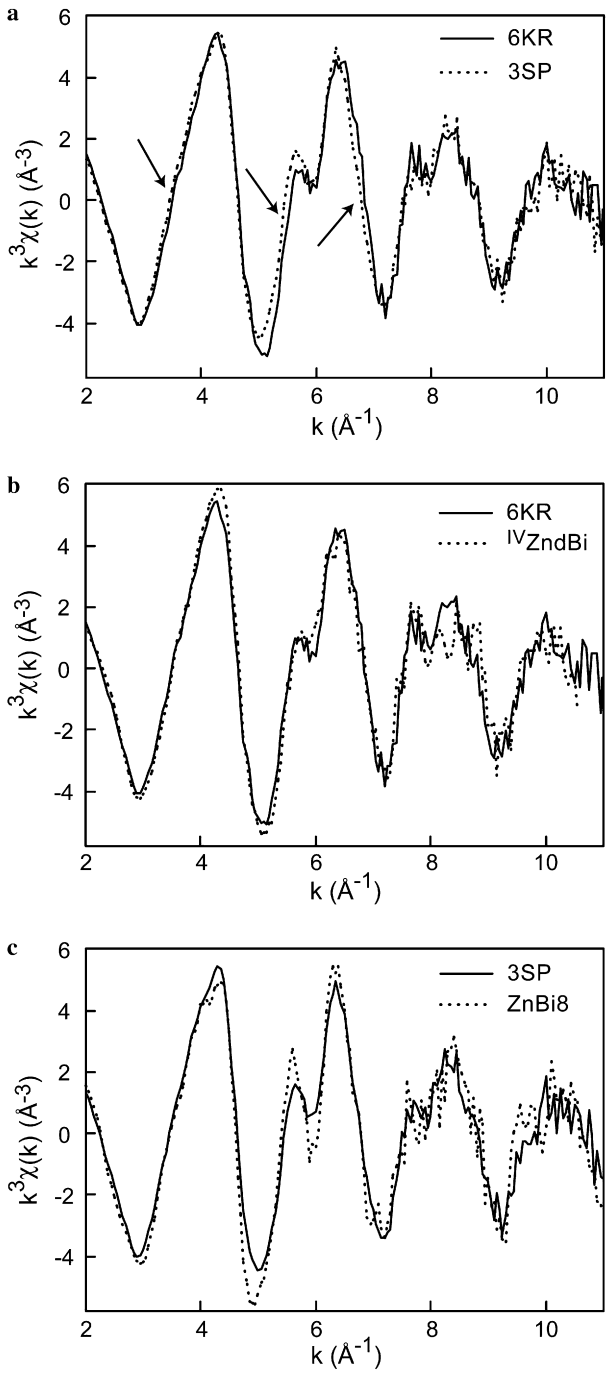

Fig. 5. Comparison of Zn K-edge EXAFS spectra for (a) 6KR and 3SP, (b) 6KR and natural vernadite (^{IV}ZndBi), and (c) 3SP and synthetic hexagonal birnessite (ZnBi8, Zn/Mn = 0.008). The reference data are described in Manceau et al. (2002a) and Marcus et al. (2004b).

3.5. Ni K-EXAFS

3.5.1. Model compounds

The Ni-EXAFS spectra for Ni-sorbed δ-MnO_2 vary as a function of pH and Ni/Mn ratio (Fig. 6a–c). The complete set of data can be described with only three spectra: NidBi2-4 (low Ni/Mn, pH 4), NidBi2-7 (low Ni/Mn, pH 7), and NidBi105-4 or NidBi177-7 (high Ni/Mn) because at high Ni/Mn ratio, the low- and high-pH spectra are statistically indistinguishable (Fig. 6d). The spectral FTs can be compared to determine if each spectrum is from a single or multiple Ni species. Two metal shell peaks at $R + \Delta R = 2.4$–2.5 Å (peak B) and 3.1 Å (peak C) are observed, beyond the Ni–O peak at $R + \Delta R = 1.6$ Å (peak A) (Fig. 7a and b). The variation in magnitude of peaks B and C with pH and Ni/Mn ratio verifies that there are three distinct Ni binding environments. At low loading and pH, the metal shell peak is approximately at the same position as ^{VI}Zn in chalcophanite and birnessite (Fig. 4b), suggesting the formation of a Ni complex at vacant layer sites (^{TC}Ni complex, Fig. 3). The Ni–Mn EXAFS distance and coordination number (*CN*) obtained by least-squares fitting the NidBi11-4 spectrum are 3.49 ± 0.02 Å and 6.5 ± 1.5 ($\sigma = 0.095$ Å), in good agreement with structural data for octahedral ^{TC}Zn on chalcophanite and birnessite (d(Zn–Mn) = 3.48–3.50 Å, $CN = 6$; Post and Appleman, 1988; Manceau et al., 2002a) (Table 3).

At low loading and high pH, the peak from the ^{TC}Ni complex has a lower magnitude than peak B. Peak B is at similar position as the edge-sharing Mn–Mn peak in birnessite (Manceau et al., 1992), a singularity which was reported for Ni-containing lithiophorite (Manceau et al., 2002c) and $LiNi_{0.5}Mn_{0.5}O_2$, a phyllomanaganate used in electrochemistry (Deb et al., 2006). In these solids, Ni substitutes for Mn in the manganese layer with a Ni–Mn distance of 2.91–2.92 Å (^{E}Ni complex). Therefore, the similarity in position and phase (data not shown) of the Mn–Mn and Ni–Mn EXAFS data at $R + \Delta R \sim 2.5$ Å in δ-MnO_2 strongly suggests Ni also occupies vacant layer Mn sites (Fig. 3). This interpretation cannot be verified by plotting the EXAFS spectrum of NidBi2-7 against that of lithiophorite because at high pH the ^{E}Ni complex coexists with the ^{TC}Ni complex. It can, however, be tested by a target transformation to determine if Ni-containing lithiophorite makes up calculated abstract components of the system (Malinowski, 1977; Ressler et al., 2000; Manceau

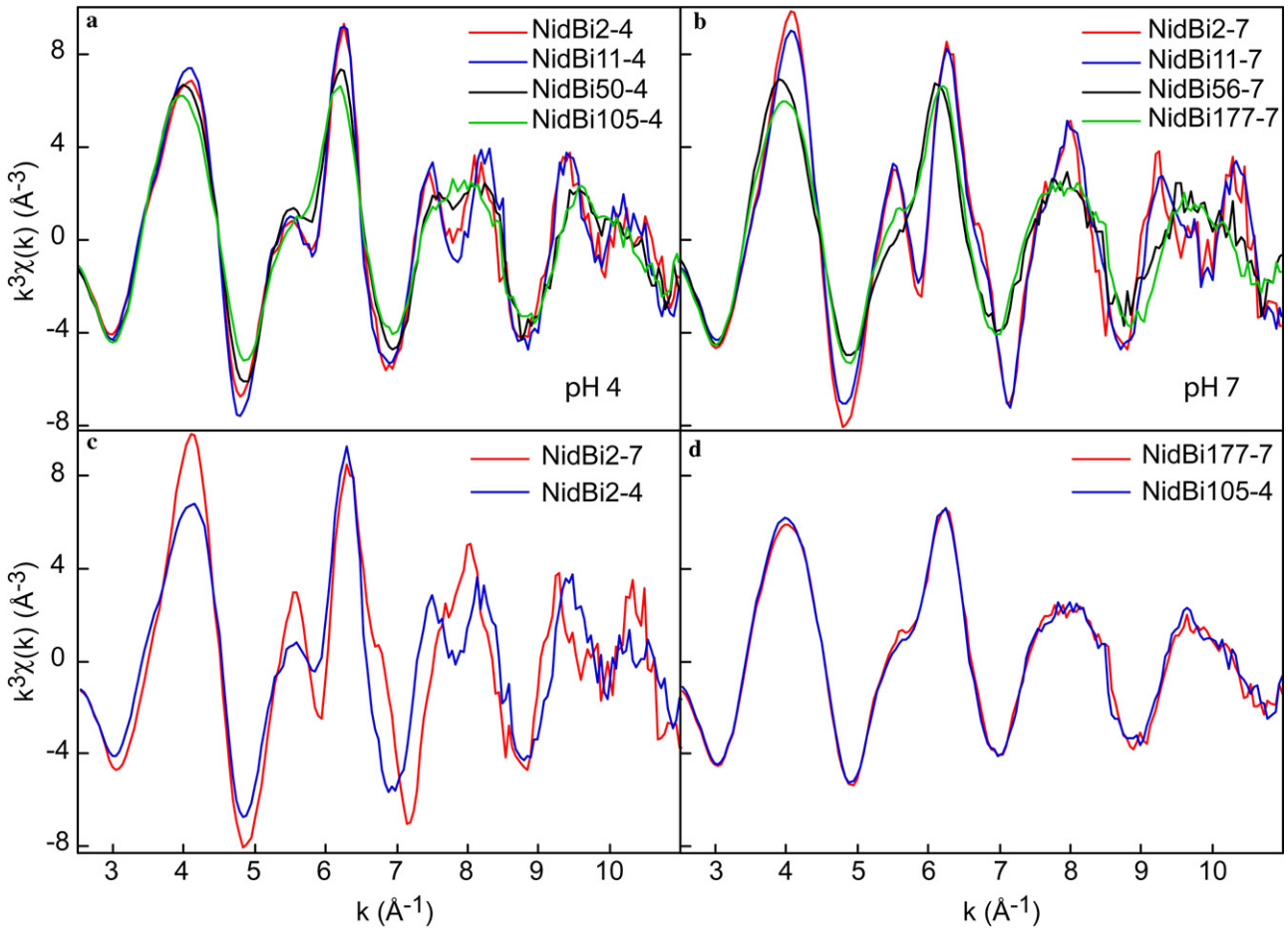

Fig. 6. Ni K-edge EXAFS spectra of Ni-sorbed δ-MnO_2 as a function of pH (4 and 7) and Ni/Mn molar ratio (i.e., surface loading). Spectra were recorded up to 14 $Å^{-1}$, but are plotted up to 11 $Å^{-1}$ for clarity. The number after the NidBi code name is the Ni to Mn mole ratio in parts per thousand. (a) pH 4 series; (b) pH 7 series; (c) comparison of pH 4 and 7 data at low surface loading; (d) comparison of pH 4 and 7 data at high surface loading.

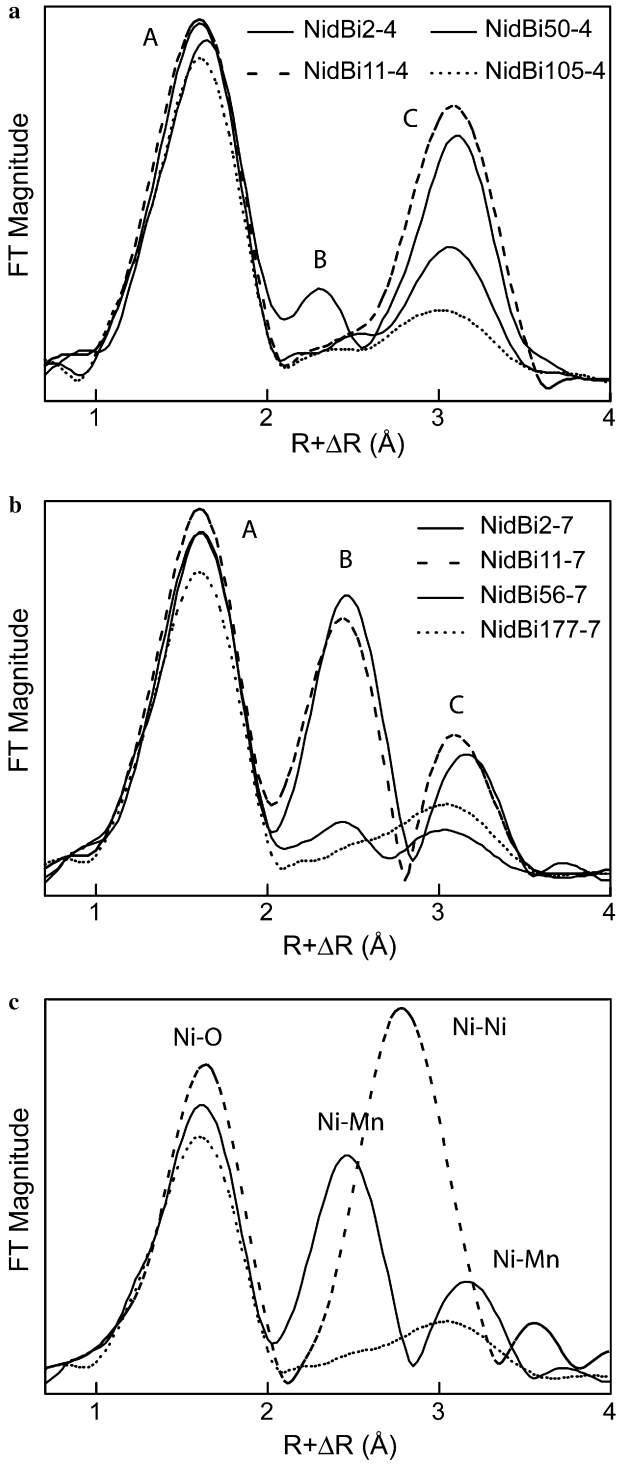

Fig. 7. Magnitude of the Fourier transforms (|FT|) for the Ni-EXAFS spectra presented in Fig. 6a and b, and for NidBi2-7 (solid line), NidBi177-7 (dotted line), and β-$Ni(OH)_2$ (dashed line) (c). In (a), the magnitude of peak C decreases in the order: NidBi11-4, NidBi2-4, NidBi50-4, and NidBi105-4. In (b), the magnitude of peak B decreases in the order: NidBi2-7, NidBi11-7, NidBi56-7, and NidBi177-7.

et al., 2002b). The target-transformed spectrum of lithiophorite calculated with the first three abstract components from the eight Ni references in Fig. 6 matched almost ideally the original spectrum, with an excellent SPOIL value as low as 1.6 (Fig. 8a), (Malinowski, 1978). This result demonstrates that the EXAFS contribution from the ^{E}Ni complex is a component of the data set. Principal component analysis confirms the system's ternary dimension, since the IND parameter reached a local minimum for the third abstract component and a clear cutoff in the marginal decline of the eigenvalues occurred between the third and higher order abstract components (Fig. 8b). Also, visual inspection of the abstract components weighted by eigenvalues showed that the first three resembled real spectra, while additional components indicated only statistical noise. The proportions of the ^{TC}Ni and ^{E}Ni complexes in NidBi2-7 were evaluated independently by *ab initio* FEFF simulation (Table 3, Fig. 9b), and by least-squares fitting of the experimental spectrum with linear combinations of the reference spectra for the ^{E}Ni (lithiophorite) and ^{TC}Ni (NidBi11-4) complexes. These two approaches gave statistically the same amounts for the two complexes: 45% ^{E}Ni and 55% ^{TC}Ni.

Determining the nature of the third Ni surface complex is less straightforward because several hypotheses can be considered. The first and most obvious interpretation is the formation of a nickeloan precipitate at high surface loading. This possibility was tested by target transformation of the selected three abstract components with three Ni hydroxide references: α-$Ni(OH)_2$, β-$Ni(OH)_2$, and poorly crystalline Ni precipitate (Fig. 8a). The last reference was obtained by hydrolyzing a $Ni(NO_3)_2$ solution. The Ni precipitate has $Ni(OH)_2$-like short range order (Defontaine et al., 2003) and is regarded as a good surrogate for Ni precipitated in the supernatant or at the δ-MnO_2 surface. The SPOIL values were between 4 and 8, and can be regarded as poor to unacceptable (Malinowski, 1978). The transformed spectra also missed several significant experimental features. Better agreement (SPOIL = 3.5) was obtained with Ni asbolane, a mixed-layer compound made of alternating MnO_2 and $Ni(OH)_2$ layers (Manceau et al., 1992) but, this solution was not satisfying for the following reason (Fig. 8a). In all nickel hydroxides, regardless of the degree of crystallinity by XRD, Ni is surrounded by approximately six Ni atoms at $R = 3.0$–3.1 Å in an edge-sharing layer. Consequently, their FTs always exhibit an intense Ni-Ni peak at $R + \Delta R = 2.7$–2.8 Å, even when the solid is disordered (Mansour and Melendres, 1998; Defontaine et al., 2003). This Ni–Ni peak is between the Ni–Mn peak of NidBi2-7 and the metal shell peak of NidBi177-7 and NidBi105-4, and its magnitude is higher (Fig. 7c). Also, fitting the NidBi105-4 spectrum to a linear combination of ^{TC}Ni (spectrum NidBi2-4) + $Ni(OH)_2$, and the NidBi177-7 spectrum to a combination of ^{E}Ni (lithiophorite reference) + $Ni(OH)_2$, failed. This failure was predictable because the NidBi105-4 and NidBi177-7 spectra are identical (Fig. 6d) and, thus, cannot be reconstructed with two different combinations of spectra. The identity of the NidBi105-4 and NidBi177-7 spectra implies that $\alpha A + \chi C = \beta B + \delta C$, with A standing for the ^{TC}Ni species spectrum, B for the ^{E}Ni species spectrum, C for $Ni(OH)_2$

Table 3
Results from quantitative analysis of the Ni K-edge EXAFS data

Sample	Ni–O			Ni–Mn			Ni–Mn			ΔE	*Res*
	R (Å)	*CN*	σ (Å)	*R* (Å)	*CN*	σ (Å)	*R* (Å)	*CN*	σ (Å)		
NidBi2-7	2.04	6[a]	0.085	2.88	2.7	0.088	3.48	3.3	0.088[b]	0.2	11.9
NidBi11-4	2.06	6[a]	0.090	—	—	—	3.49	6.5	0.095	0.9	12.5
NidBi105-4	2.05	6[a]	0.095	—	—	—	3.49	2.5	0.11	0.7	15.2
3SP	2.05	6[a]	0.085	2.90	1.6	0.10	3.50	4.4	0.10[b]	2.0	16.0

ΔE, inner potential correction in eV; *Res*, fit residual defined as $\sum\{|\chi_{exp} - \chi_{fit}|\}/\sum\{|\chi_{exp}|\}$; interval of the inverse Fourier transform: 1.05–3.6 Å; $S_0^2 = 0.85$.
[a] Fixed value.
[b] Parameter linked to the value for the first Mn shell during the minimization.

or any other surface precipitate, and α and χ, and β and δ, the fractional amounts of each species in the NidBi105-4 and NidBi177-7 samples. This equation has no general solution because the A and B spectra are different (i.e., they correspond to different surface complexes). Thus, $\alpha \approx \beta \approx 0$. This means that the high coverage data cannot be described as a mixture of one or more than one surface complex with a surface precipitate. At high loading, the contribution from surface complexes to the total EXAFS signal is negligible because their fractional amount is low. Thus, the NidBi105-4 and NidBi177-7 spectra look like pure species spectra, even though they are multi-component.

The only plausible interpretation is the formation at high coverage of another surface complex. Its sorption site must have an elevated surface density (i.e., high sorption capacity) and a relatively low affinity for the sorbed metal (i.e., low surface charge deficit). Also, the sorbed cation should be coordinated to one or two Mn atoms in a corner-sharing configuration to account for the position and low magnitude of peak C in NidNi105-4 and NidBi177-7. We infer that the third site occurs at edges of the MnO_2 layers, and that Ni forms a double-corner surface complex (^{DC}Ni) on these sites. Consistent with this interpretation, a simple two-shell model of 6 O at 2.05 Å and 2.5 Mn at 3.49 Å ($\sigma = 0.11$ Å) correctly described the data (Table 3, Fig. 9c). There was no need to invoke a more complicated model or to add a contribution from the ^{E}Ni or ^{TC}Ni complexes.

3.5.2. Sample 3SP

The powder spectrum for 3SP resembles the δ-MnO_2 spectrum at low Ni concentration and pH (NidBi2-4), albeit with minor differences in shape (Fig. 10a). The FT of 3SP has two metal shell peaks of equal magnitude, whose position and amplitude are characteristic of ^{E}Ni and ^{TC}Ni complexes. The least-squares fit of the data yielded 1.6 Mn at 2.90 Å and 4.4 Mn at 3.50 Å ($\sigma = 0.10$ Å), indicating that about 1/4 of the Ni atoms form the ^{E}Ni complex and 3/4 the ^{TC}Ni complex (Table 3, Fig. 9d). The fraction of Ni at each site was confirmed by reconstructing the 3SP spectrum with a linear combination of the lithiophorite (100% ^{E}Ni complex) and NidBi11-4 (~100% ^{TC}Ni complex) references (Fig. 10c). Optimal fit to the data was obtained with a combination of 24% ^{E}Ni complex + 65% ^{TC}Ni complex (the precision is 10% of total Ni). The inclusion of the ^{E}Ni component decreased the goodness-of-fit parameter from 0.16 (one-component fit) to 0.09 (two-component fit), and resulted in fairly good reproduction of the magnitude of the two metal shell peaks on the FT (Fig. 10d). The inclusion of either NidBi105-4 or NidBi177-7 as a third component resulted in 22% ^{E}Ni + 47% ^{TC}Ni + 25% ^{DC}Ni. This solution is not justified statistically because the goodness-of-fit parameter (0.085) did not improve, despite the higher degree of freedom. Therefore, we conclude that the amount of the ^{DC}Ni complex is <10% of total Ni, and that on average about 1/4 of the Ni is sorbed at the E site and 3/4 at the TC site.

3.6. Ba L3-EXAFS

3.6.1. Model compounds

Two model compounds were selected: hollandite, a 2×2 tunnel structure tectomanganate containing barium inside the tunnels (Byström and Byström, 1950), and Ba-exchanged triclinic birnessite. The second reference was obtained by immersing synthetic triclinic sodium birnessite in 0.3 mol/L $Ba(NO_3)_2$, shaking the suspension for three days, and then centrifuging and rinsing the solid. The operation was repeated once to complete the Ba exchange. In

Fig. 8. (a) Target transformations (dotted lines) of Ni-containing lithiophorite (SPOIL = 1.6; Sum-Sq = 0.083), asbolane (SPOIL = 3.5; Sum-Sq = 0.145), α-$Ni(OH)_2$ (SPOIL = 4.0; Sum-Sq = 0.263), freshly precipitated Ni hydroxide (SPOIL = 5.2; Sum-Sq = 0.344), and β-$Ni(OH)_2$ (SPOIL = 7.8; Sum-Sq = 0.491) (solid lines). The lithiophorite reference is described in Manceau et al. (2002c). Sum-Sq is the sum of the squares of the residuals, normalized to the sum of the squares of the data values. (b) First six abstract components weighted by eigenvalues (λ) of the $k^3\chi(k)$ spectra for the eight Ni references presented in Fig. 6a and b. IND is the Malinowski (1977) indicator. The indicator is a minimum for the third component, suggesting that there are three significant components (i.e., Ni species). The first three components look like EXAFS and the other three like noise and have a similar S/N ratio (i.e., λ value).

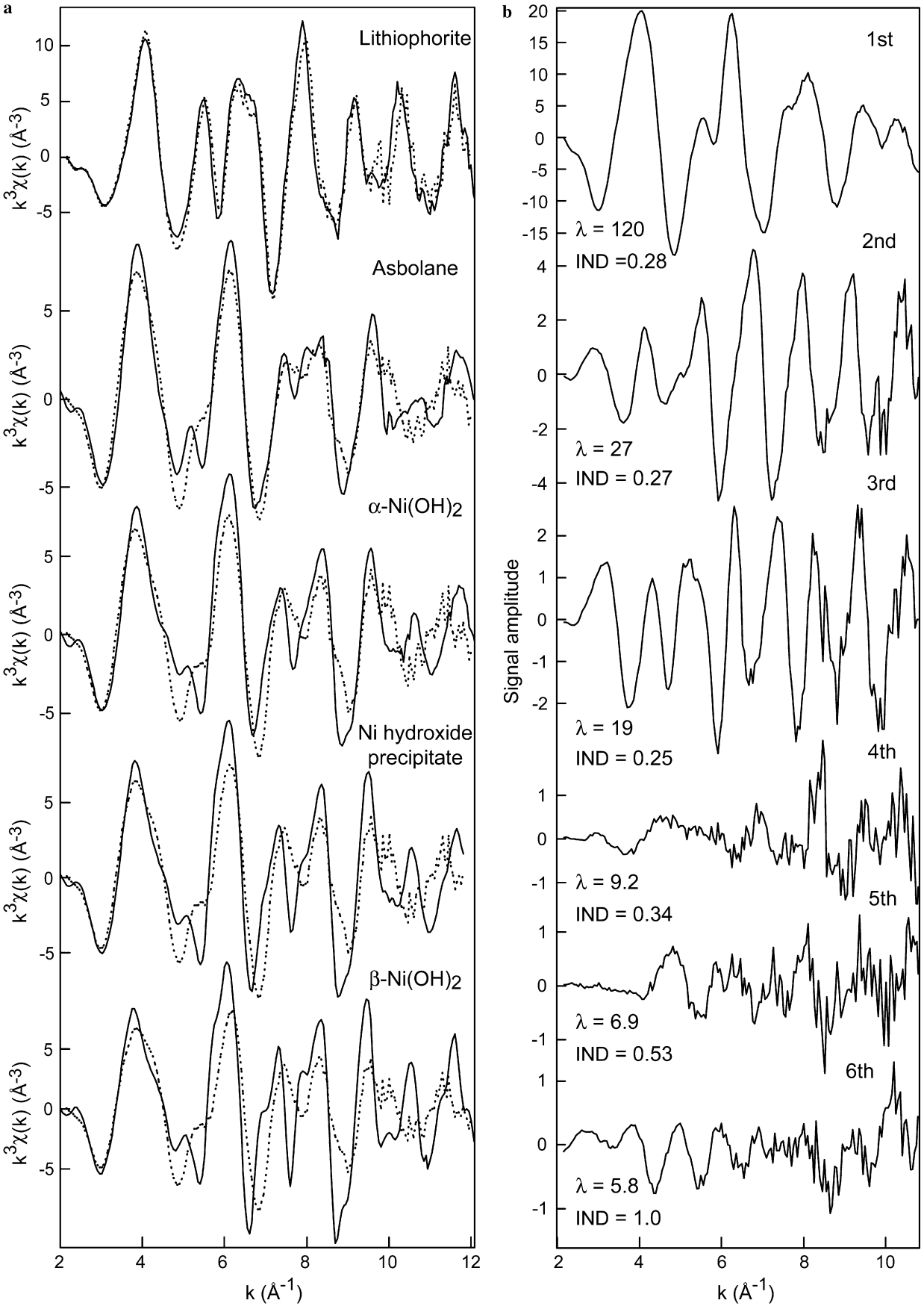
a
Lithiophorite
Asbolane
α-Ni(OH)2
Ni hydroxide precipitate
β-Ni(OH)2
k3χ(k) (Å-3)
k (Å-1)
b
1st
λ = 120
IND =0.28
2nd
λ = 27
IND = 0.27
3rd
λ = 19
IND = 0.25
4th
λ = 9.2
IND = 0.34
5th
λ = 6.9
IND = 0.53
6th
λ = 5.8
IND = 1.0
Signal amplitude
k (Å-1)

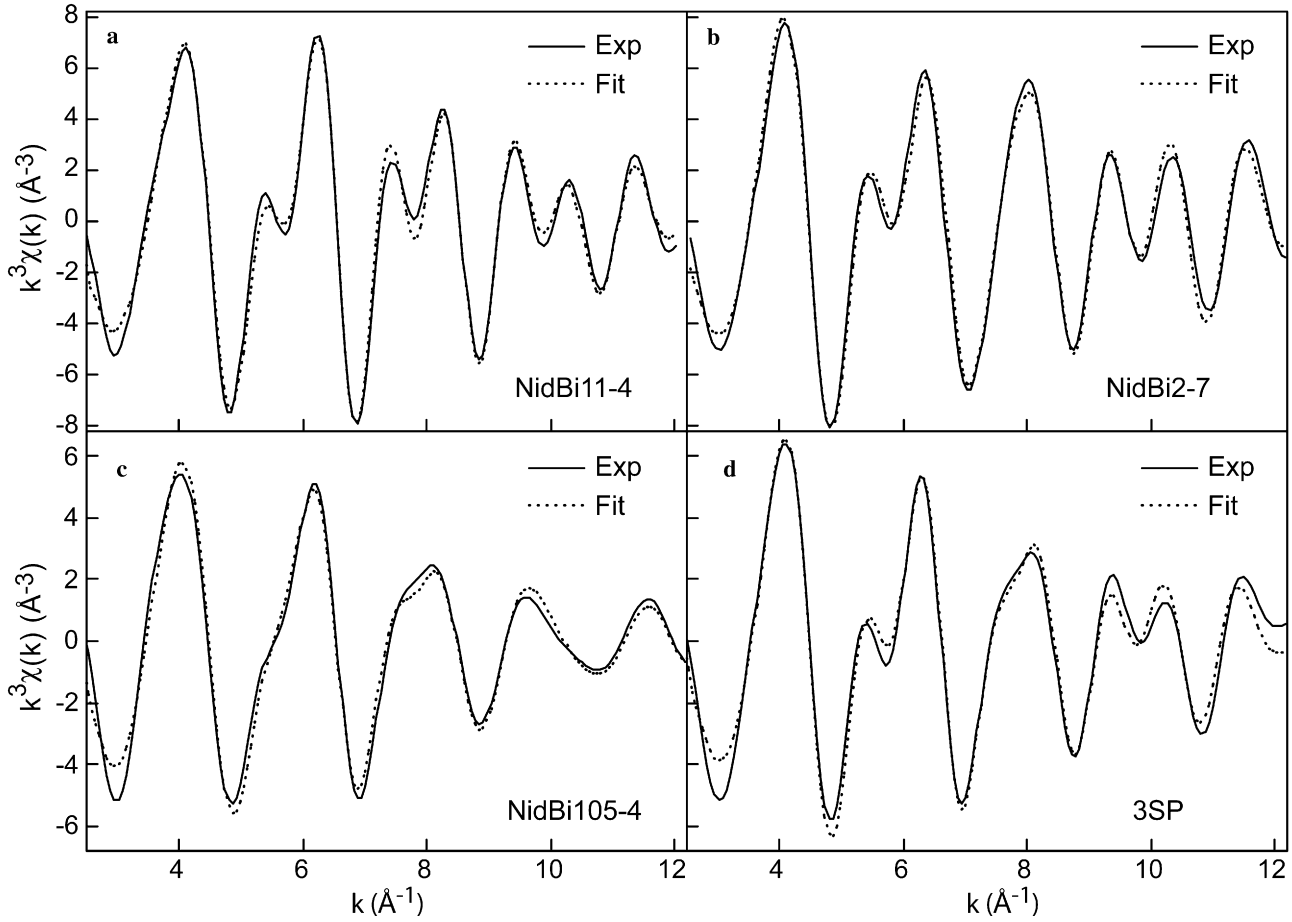

Fig. 9. (a–c) Inverse Fourier transform of Ni references (NidBi11-4, NidBi2-7, and NidBi105-4), and (d) the 3SP quartz coating in the [1.1–3.6 Å] $R + \Delta R$ interval (A + B + C FTs peaks) with spectral simulations. The data are in solid lines, and the models in dotted lines.

hollandite, Ba occupies the center of the 2×2 array of MnO_6 octahedra, and is coordinated to eight oxygens from the Mn walls (two from each wall) (Fig. 11a). This site is energetically favorable because eightfold coordinated Ba is similar in size to the diameter of the tunnels (4.6 Å), and can evenly balance the negative structural charge from the four manganate walls. Barium is octahedrally coordinated to three layer oxygens and three water molecules in the interlayer of birnessite (Gaillot, 2002), in contrast to hollandite. Despite the differences in Ba coordination and framework structures between hollandite and birnessite, Ba is located above the empty tetrahedral cavities in both (Fig. 11a and b), but is displaced slightly toward one of the three O_{layer}–O_{layer} edges. The Ba position is close to that reported for K in high temperature birnessite (Gaillot et al., 2003), and biogenic Mn birnessite synthesized by *Pseudomonas putida* (Villalobos et al., 2006). As a consequence of the displacement, the Mn shells are split and consist of one nearest Mn from the closest octahedral chain (Mn1 shell), two next-nearest Mn from the adjacent chain (Mn2 shell), and two third-nearest Mn from the closest chain (Mn3 shell). Since Ba is framed by four Mn walls in hollandite, the total number of atoms in each shell is four times higher than in birnessite. The Ba–Mn distances are 3.58–3.65 Å (×4), 3.99–4.17 Å (×8), and 4.59–4.64 Å (×8) in hollandite (Miura, 1989), and are unknown in Ba-exchanged triclinic birnessite.

EXAFS spectra of hollandite and birnessite have obvious likenesses and distinctive features (Fig. 12a), such as similar frequency and lineshape, but different amplitude. Similarities and differences are also evident in the FTs, which show that Ba atoms are surrounded by the same types of atoms at comparable distances in the two structures, but to a lesser extent in birnessite (Fig. 12b). Structural fits to the spectra, filtered in the [1.5–5.1 Å] $R + \Delta R$ interval, are displayed in Fig. 13a and b. In agreement with crystallographic data, a four-shell fit consisting of 8 O at 2.90 Å ($\sigma = 0.13$ Å), 4 Mn1 at 3.68 Å ($\sigma = 0.12$ Å), 8 Mn2 at 4.00 Å ($\sigma = 0.17$ Å), and 8 Mn3 at 4.66 Å ($\sigma = 0.13$ Å) reproduced the wave envelope, phase, and amplitude of the hollandite data. A four-shell fit of 6 O at 2.85 Å ($\sigma = 0.13$ Å), 1 Mn1 at 3.62 Å ($\sigma = 0.09$ Å), 2 Mn2 at 4.08 Å ($\sigma = 0.16$ Å), and 2 Mn3 at 4.68 Å ($\sigma = 0.11$ Å) accounted for all spectral features in birnessite. The small differences in interatomic distances between the two references are actually perceptible in the data since the FTs show that the imaginary part of birnessite is shifted to lower $R + \Delta R$ value at 2.2 Å, and to higher $R + \Delta R$ val-

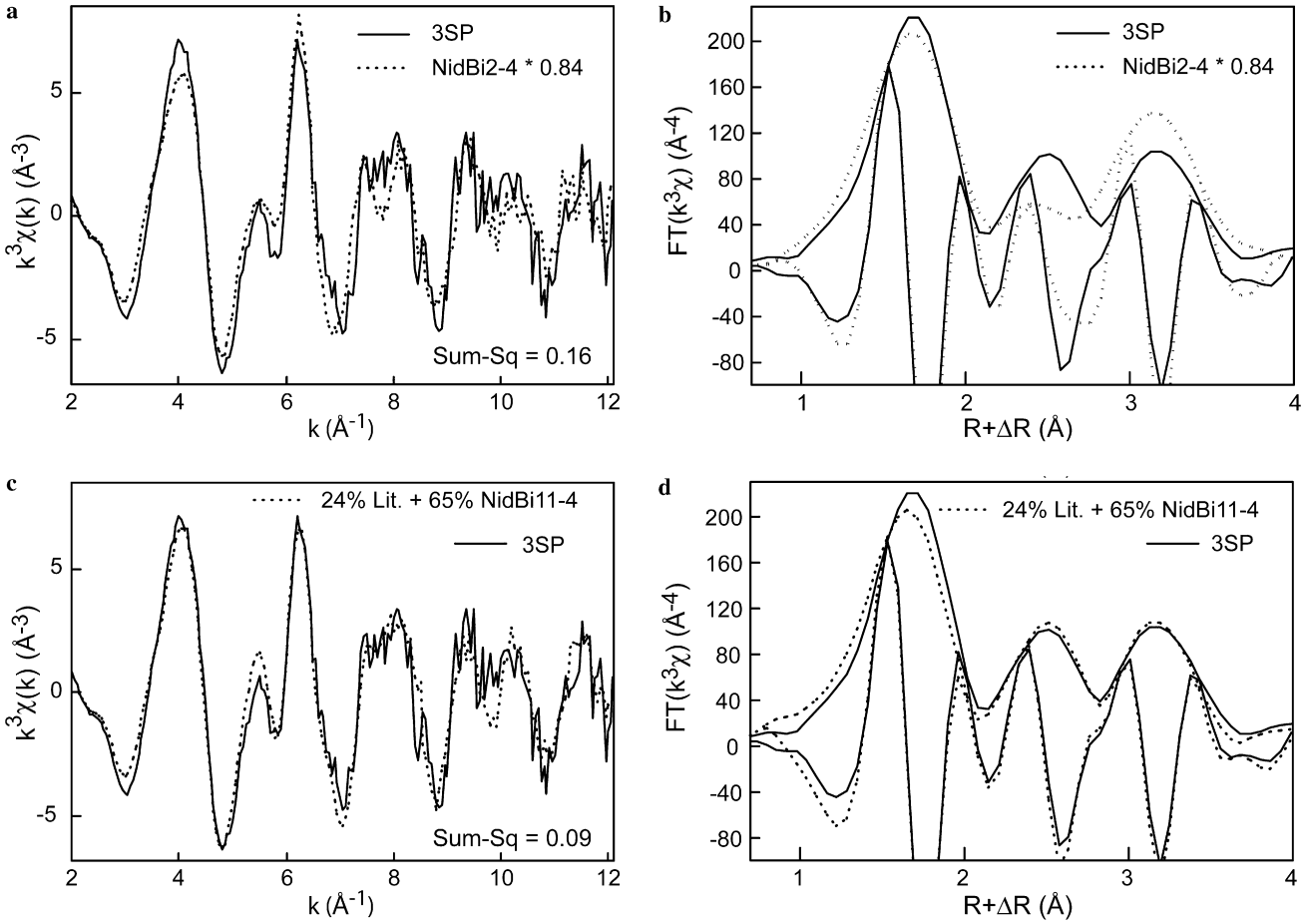

Fig. 10. Ni K-edge EXAFS spectrum (a and c) and its Fourier transform (b and d) for the 3SP quartz coating and their simulations using one (a and b) and two (c and d) components. Sum-Sq is the goodness-of-fit parameter expressed as the sum of the squares of the residuals, normalized to the sum of the squares of the data values.

ue at 4.5 Å relative to hollandite (Fig. 12b). Shortening of the Ba–O distance in birnessite is consistent with octahedral coordination, and the differences in Ba–Mn distances between birnessite and hollandite likely result from the presence of Mn^{3+}-rich rows in the Mn layer of triclinic birnessite (Drits et al., 1997; Lanson et al., 2002a).

3.6.2. Sample 3SP

The spectrum for 3SP is similar to the reference birnessite spectrum from 2 to 4.5 $Å^{-1}$, but differs at higher k values (Fig. 12c). The sample spectrum was truncated at 7.9 $Å^{-1}$ because of the presence of trace La, whose L_3 edge is located 236 eV above the Ba L_3 edge. FEFF simulations showed that the low k region, and in particular the amplitude of the second oscillation peak at 4.1 $Å^{-1}$, is sensitive to Ba coordination, reaching about 4.5 $Å^{-3}$ when Ba is eightfold and 2.7 $Å^{-3}$, when it is sixfold. Using that feature as a fingerprint, along with the reduction in magnitude of the first FT peak for the sample relative to hollandite, Ba is deduced to be sixfold in 3SP. The k region above 4.5 $Å^{-1}$ is primarily sensitive to the contribution from Mn atoms and, in particular, the wave frequency is sensitive to small variations of the Ba–Mn distances.

Optimal fit of the Fourier-filtered Ba–O and Ba–Mn contributions to the sample data in the [1.5–5.1 Å] $R + \Delta R$ range was obtained by taking the structural model of triclinic birnessite and optimizing only the interatomic distances (Fig. 13c). The Ba–O distance was identical to that of the birnessite reference (2.85 Å), confirming that Ba is octahedral in the quartz coating. However, the Ba–Mn1 and Ba–Mn3 distances were lengthened by 0.06 and 0.04 Å, respectively, and the Ba–Mn2 distance shortened by 0.16 Å in 3SP relative to triclinic birnessite. These differences are consistent with the imaginary parts of the FTs (Fig. 12d). Since the Mn1 and Mn3 atoms belong to the same row in the Mn layer, these changes in the Ba–Mn distance indicate that Ba is shifted toward the adjacent row, nearer to the center of the trigonal cavity (Position 1 in Fig. 11c). Barium is not displaced toward one of the three O_{layer} from the tetrahedral cavity (Position 2 in Fig. 11c) because the first cationic shell would contain two Mn atoms, and the second and third shells one, instead of one, two, and two, respectively. Positioning Ba at the exact center of the tetrahedral cavity (Position 3) is not a possibility either, because the three Ba–Mn distances would reduce to two due to the threefold local symmetry of this site

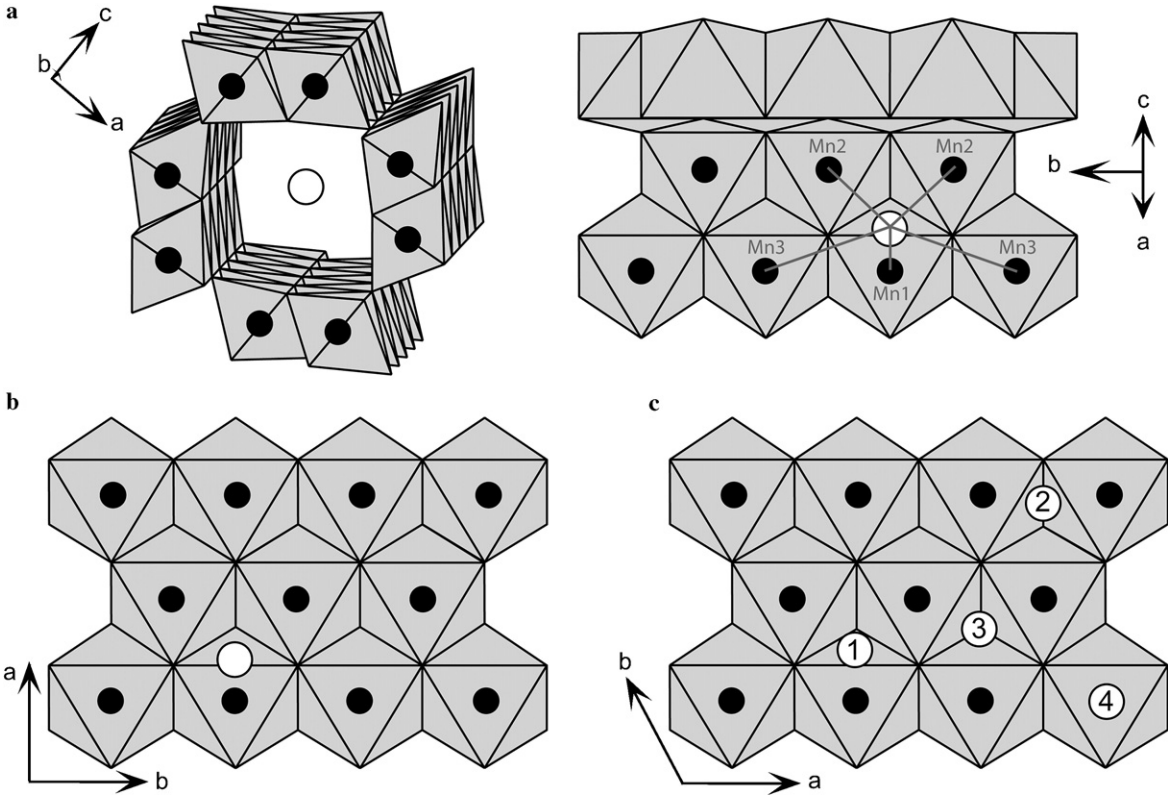

Fig. 11. Binding sites for barium in the tunnel of hollandite (a), and in the interlayer of triclinic (b) and hexagonal (c) birnessite. In all these minerals, Ba is shifted in the layer plane from the center of the tetrahedral cavity formed by the triads of edge-sharing MnO_6 octahedra in the direction of two undersaturated O_{layer} atoms (Position 1 in c). Mn1, Mn2, and Mn3 are the three nearest Mn shells about Ba. Positions 2, 3, and 4 in c are hypothetical interlayer sites for Ba in hexagonal birnessite.

with respect to cationic shells. Finally, if Ba sorbed at a vacant layer site, like Zn and ^{TC}Ni (Position 4), it would be surrounded by a single Mn shell of six atoms, which is inconsistent with the spectral fits and with the presence of Mn peaks at $R + \Delta R \approx 3.4$–3.5 and 4.5 Å on the FT of 3SP.

The sharp resonance at $k = 5.50$ Å^{-1} in the three Ba EXAFS spectra (Fig. 12) has been attributed to a double electronic excitation at the L_3 edge of barium (Almeida et al., 1994; Tressaud et al., 1989). From the agreement between EXAFS and XRD results for hollandite, and the overall consistency in our determination of the site occupation and local structure of Ba in the three analyzed compounds, it appears that this feature does not introduce any detectable bias in the data analysis.

3.7. As -EXAFS

Arsenic K-edge powder EXAFS spectra were collected for the two samples containing the most As, 6KR and 3SP. The spectra were similar to each other and to those for natural and synthetic As-sorbed ferrihydrite (Morin et al., 2002; Sherman and Randall, 2003; Cances et al., 2005). Spectrum 6KR is compared to that of scorodite ($Fe(AsO_4)(H_2O)_2$), which is composed of single Fe octahedra and As tetrahedra linked at corners in such a way that each octahedron shares four oxygens with four different tetrahedra, and each tetrahedron shares its oxygens with four different octahedra (Kitahama et al., 1975; Hawthorne, 1976) (Fig. 14a). In scorodite, the four As–O interatomic distances are almost identical (1.67–1.68 Å), and the four As–Fe distances are similar (3.33–3.39 Å). In agreement with XRD data, the As K-edge FT of scorodite exhibits two prominent peaks at $R + \Delta R \sim 1.4$ and 3.0 Å from the nearest O and Fe shells, and the EXAFS spectrum has the appearance of a two-frequency interference function (Fig. 14b). In contrast, the quartz coating spectrum is a simple sinusoidal As–O wave function, without evidence of significant contribution from higher shells, as confirmed by the low magnitude of the As–Fe peak on the FT. Qualitatively, one may conclude that the As tetrahedra are not connected to as many Fe octahedra in 6KR as in scorodite, and thus are bonded at the surface of ferrihydrite particles or at grain boundaries.

The first and second shell contributions to the scorodite FT were simulated in a two-shell single scattering model with 4.5 O ($\sigma = 0.04$ Å) at 1.68 Å and 4.0 Fe ($\sigma = 0.06$ Å) at 3.36 Å (Fig. 15a). The wave envelope, phase, and amplitude of the data were reproduced, but not the lineshape of the first oscillation. We know that this region of reciprocal space is complicated by the occurrence of multiple scattering (MS) paths of the photoelectron (Foster et al., 1998;

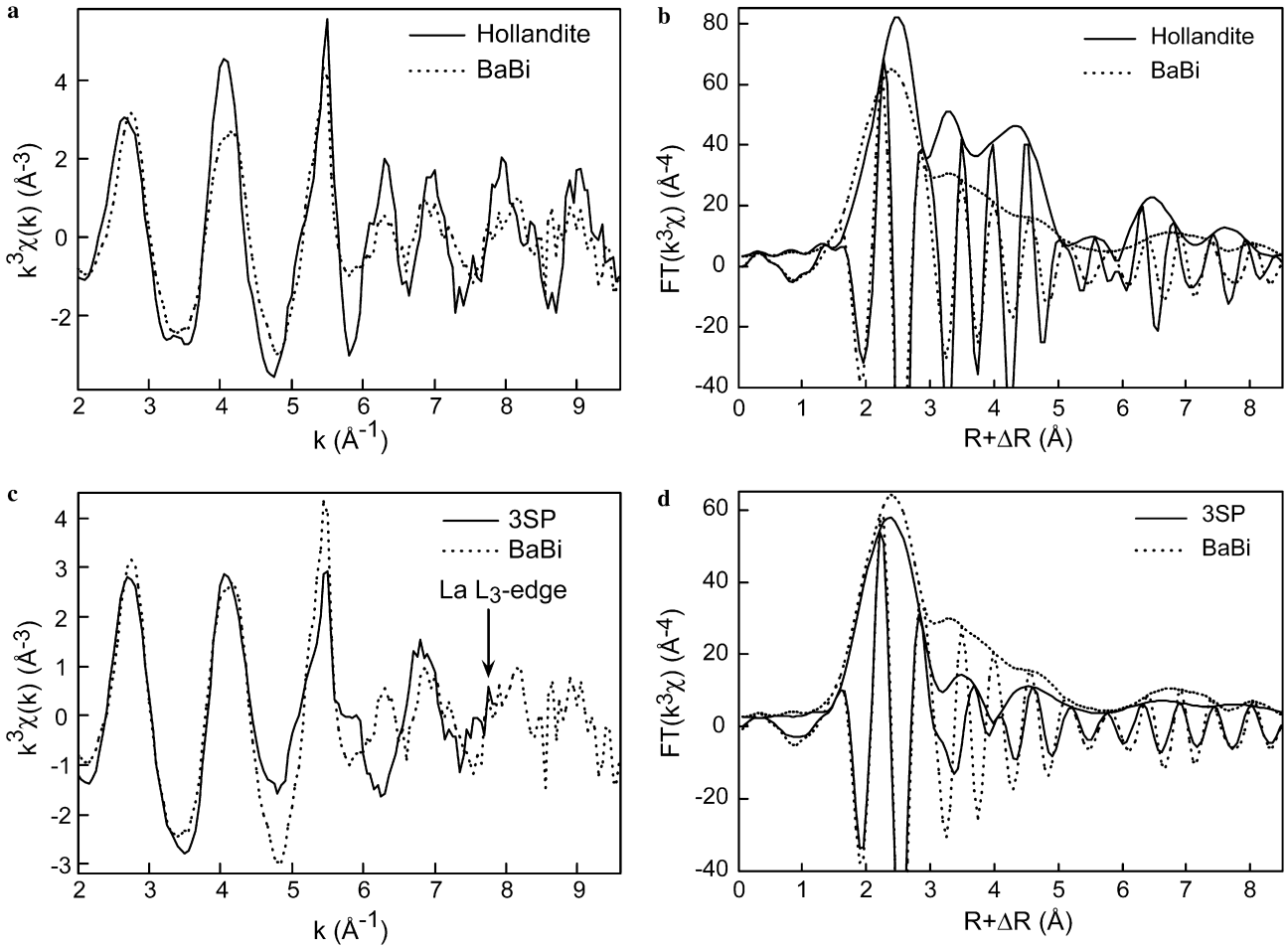

Fig. 12. Ba L_3-edge EXAFS spectra (a and c) and their Fourier transforms (b and d) for the 3SP quartz coating and two references: hollandite with Ba in the tunnels of the tectomanganate structure, and Ba-exchanged triclinic birnessite with Ba in the interlayer of the phyllomanganate structure. (b) FTs performed over the [3.0–9.5 Å^{-1}] k interval. (d) FTs performed over the [3.0–8.0 Å^{-1}] k interval.

Morin et al., 2002; Paktunc et al., 2003, 2004; Sherman and Randall, 2003). The contribution from MS paths manifests itself in the [1.0–3.8 Å] $R + \Delta R$ interval of the scorodite FT by two shoulders on either side of the As–Fe peak (arrows in Fig. 14b). The right shoulder is not detected in the sample FT, but the left shoulder is suggested by the presence of a hump at $R + \Delta R = 2.6$ Å. To elucidate the origin of this feature in the sample FT, MS paths were introduced to the model fit of scorodite. According to FEFF calculations (Ankudinov et al., 1998), the most important MS paths having a maximum half path length of $R = 4.0$ Å fall into four groups: noncollinear double (As–O1–O2, MS2-1) and triple (As–O1–As–O2, MS3-1) scattering paths, collinear triple paths within the AsO_4 tetrahedron (As–O1–As–O1, MS3-2), and an As–O–Fe double path (As–O–Fe, MS2-2) (Fig. 16) (Pandya, 1994; Foster et al., 1998). In scorodite these paths have effective lengths of $R = 3.02$–3.07 Å, 3.35–3.37 Å, 3.34–3.37 Å, and 3.49–3.52 Å, respectively. The associated phase shift and amplitude functions were calculated for a scorodite cluster 9 Å in diameter using FEFF v.7.02 (Ankudinov et al., 1998). All possible combinations of the four paths were tested in the spectral fit of scorodite (Table 4 and Fig. 15). Adding the MS2-1 or MS2-2 paths to the model rendered the first oscillation asymmetric in the direction of the data. Combining the two double paths brought the experimental and theoretical curves even closer (Fig. 15d). Simulations with MS3-1 or MS3-2 paths without double paths were unstable. However, when combined with the MS2-1 and MS2-2 paths, the spectral match improved slightly. Therefore, the contribution of the triple paths to the EXAFS signal is minor.

The same fit strategy was applied to 6KR, except that the raw instead of the Fourier-filtered data were fitted because distant shells from sorption complexes are disordered and contribute less to the EXAFS spectrum. A two-shell fit with 5.3 O ($\sigma = 0.06$ Å) at 1.69 Å and 2.0 Fe ($\sigma = 0.10$ Å) at 3.28 Å reproduced the shape of the spectrum above 6 Å^{-1}, and in particular the asymmetry of the second oscillation, but did not replicate the shape of the first oscillation (Fig. 15f, Table 4). Consistent with the simulations for scorodite and the weak FT magnitude for 6KR beyond 3.2 Å $R + \Delta R$, inclusion of a MS2-1 contribution at 3.11 Å to the single scattering fit model moved the calculated curve to the correct position (Fig. 15g). Adding the MS2-1 path

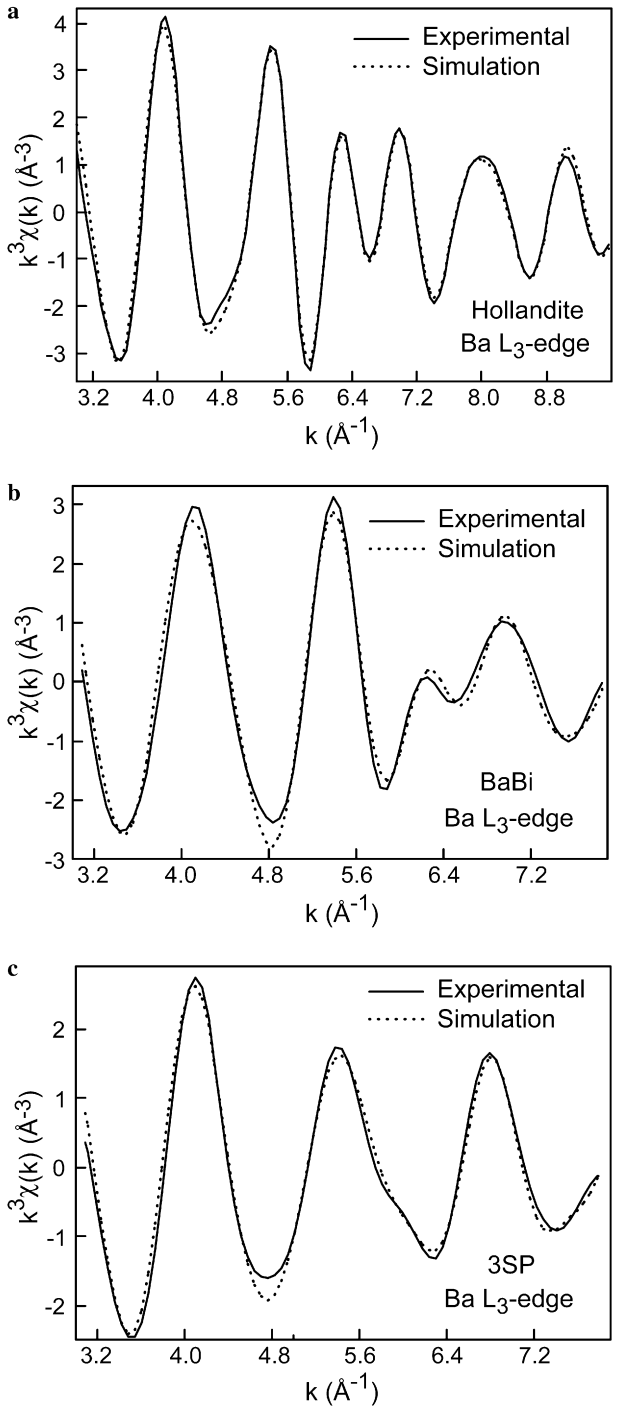

Fig. 13. Inverse Fourier transforms of (a and b) the two Ba references and (c) the 3SP quartz coating in the [1.5–5.1 Å] $R + \Delta R$ interval with spectral simulations. The data are in solid lines, and the models in dotted lines.

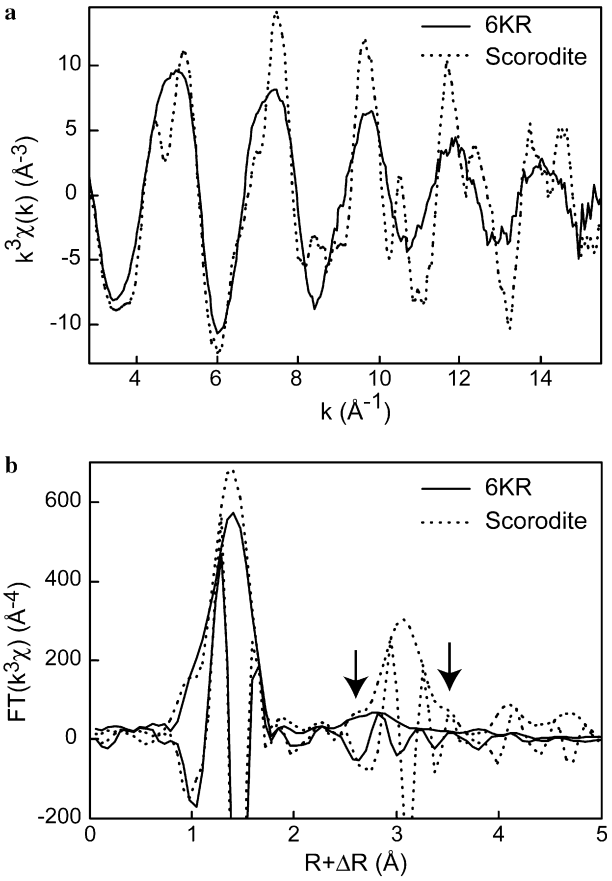

Fig. 14. (a) As K-edge EXAFS spectra and (b) Fourier transforms of the 6KR quartz coating and scorodite ($Fe(AsO_4)(H_2O)_2$).

had little effect on the structural parameters of the Fe shell because MS contributions have a maximum amplitude in the 4.0–5.5 $Å^{-1}$ k interval and do not shift significantly the frequency of the As–Fe contribution. Consideration of the longer-distance MS paths also did not improve the spectral fit significantly. The predominance of triangular multiple-scattering paths over collinear paths (MS3-1 and MS3-2) in the arsenate oxoanion and the low amplitude of the As–O–Fe path reported here are in good agreement with previous studies on the As sorption complex (Morin et al., 2002; Cances et al., 2005). The As–Fe distance of 3.28 Å is consistent with arsenate attached to two adjacent apices of edge-sharing Fe oxyhydroxyl octahedra (i.e., binuclear bidentate complex), the usual bonding configuration of arsenic tetrahedra on Fe (oxyhydr)oxides (Waychunas et al., 1993; Moldovan et al., 2003).

Since in their non-ionized states Fe and Mn differ by only one electron out of 25–26, the data can be fitted indifferently with As–Fe and As–Mn pairs (Teo, 1986). Consistent with theory, simulating the data with As–Mn pairs yielded a distance of 3.29 Å, which is not significantly different from the As–Fe distance. However, this alternative fit model is unrealistic because there is no manganese fer-

Fig. 15. (a–e) Inverse Fourier transform of scorodite in the [1.0–3.7 Å] $R + \Delta R$ interval with spectral simulations. (a) single-scattering model; (b–e) multiple-scattering models. (f and g) EXAFS spectrum of 6KR quartz coating with spectral simulations. (f) single-scattering model; (g) multiple-scattering model with the noncollinear double As–O–Fe path (MS2-1) added to the As–O and As–Fe single-scattering paths. (h) Powder EXAFS spectrum of 6KR and a natural As-containing vernadite. The arrow and the two vertical lines point out the most significant spectral differences. The μ-EXAFS spectra collected in the yellow and violet regions of the RGB map from Fig. 2c were statistically undistinguishable from the 6KR powder spectrum.

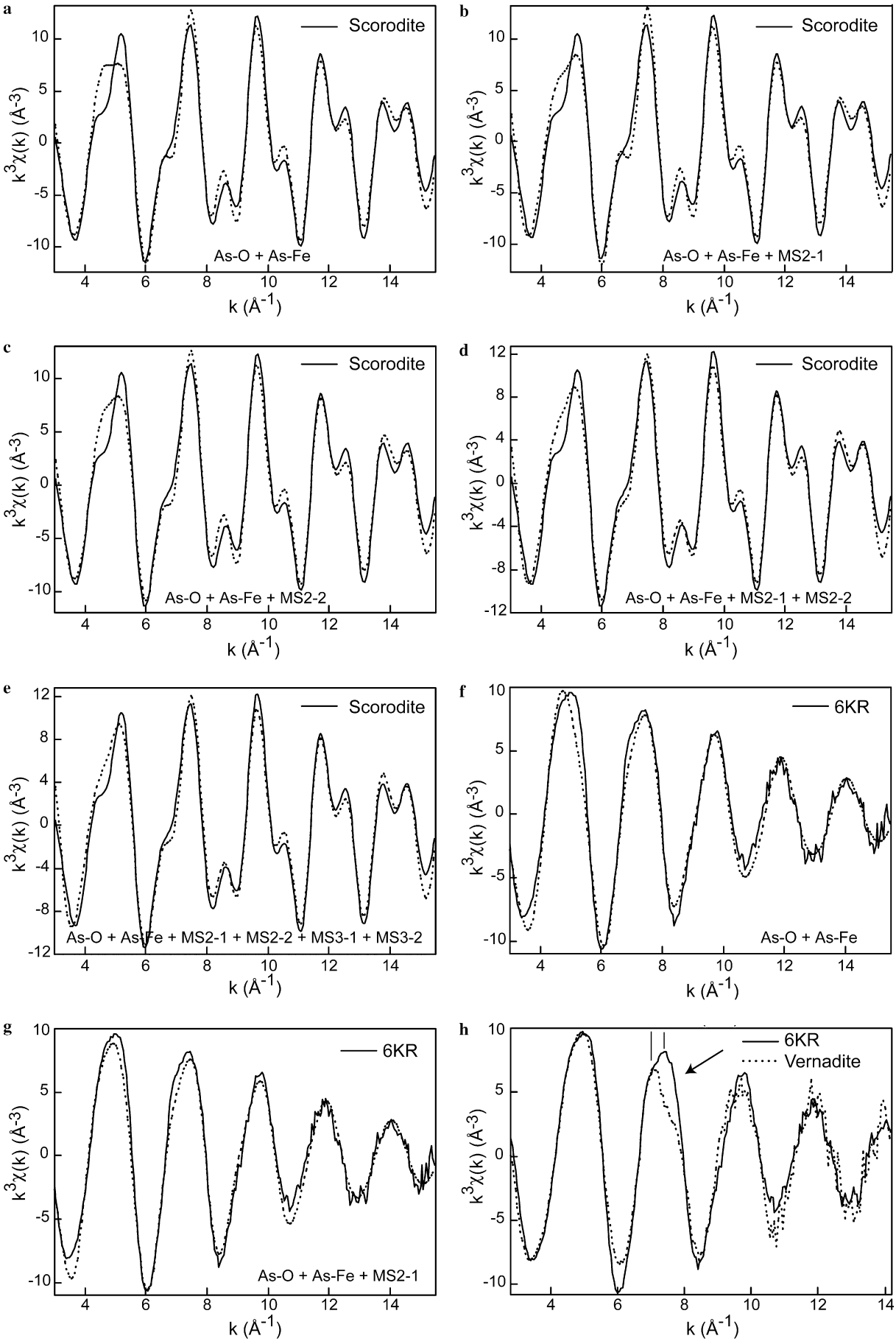
a
Scorodite
As-O + As-Fe
b
Scorodite
As-O + As-Fe + MS2-1
c
Scorodite
As-O + As-Fe + MS2-2
d
Scorodite
As-O + As-Fe + MS2-1 + MS2-2
e
Scorodite
As-O + As-Fe + MS2-1 + MS2-2 + MS3-1 + MS3-2
f
6KR
As-O + As-Fe
g
6KR
As-O + As-Fe + MS2-1
h
6KR
Vernadite
k³χ(k) (Å⁻³)
k (Å⁻¹)

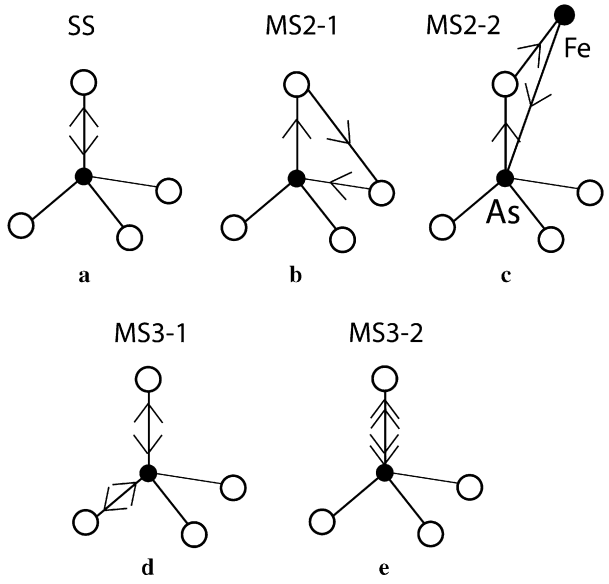

Fig. 16. Schematic representation of the various scattering paths for an AsO_4 tetrahedron. Each path originates and terminates at the central As atom. (a) Single-scattering (SS) path by an oxygen atom. (b) noncollinear double scattering by two distinct oxygens (As–O1–O2 sequence, MS2-1). (c) noncollinear double scattering by an oxygen and an iron atom (As–O–Fe sequence, MS2-2). (d) noncollinear triple scattering by two oxygens and one arsenic atom (As–O1–As–O2 sequence, MS3-1). (e) collinear triple scattering by an oxygen and an arsenic atom (As–O1–As–O1 sequence, MS3-2). The photolectron is scattered by an oxygen atom twice via the arsenic atom.

rihydrite in Nature. Thus, the possibility of As complexation to the vernadite component of the quartz coating was examined by comparing the μ-EXAFS and powder EXAFS data with those from a natural As-containing vernadite reference (Fig. 15h) (Allard et al., 1999). One distinct difference between the quartz coating and vernadite spectra is the shape of the second oscillation, which peaks at 7.4 $Å^{-1}$ in the sample spectrum vs. 7.1 $Å^{-1}$ in vernadite, where it is followed by a shoulder at 7.6 $Å^{-1}$, as reported by others (Manning et al., 2002; Foster et al., 2003). Using these features as a fingerprint for As–Mn and As–Fe bonds, the maximum fraction of As bonded to the phyllomanganate component in 6KR was estimated to be 20%, in agreement with μ-SXRF results. Our vernadite reference has an As–Mn distance of 3.21 Å, close to the 3.22 Å distance reported by Manning et al. (2002) for binuclear bidentate As complexation on synthetic vernadite. The reduction of 0.06 Å of the As-sorbent metal distance from ferrihydrite to vernadite for the same type of surface complex is smaller than that calculated from the effective ionic radii of Fe^{3+} (0.64 Å) and Mn^{4+} (0.53 Å) because the As^{5+}–Mn^{4+} pair has a higher repulsive electrostatic force than the As^{5+}–Fe^{3+} pair. Still, this reduction in distance is high enough to modify the shape of EXAFS, and to justify using this technique as a fingerprint to mineral host and chemical bonding in metal(loid) speciation studies (Manceau et al., 1996, 2002b).

Table 4
Results from the quantitative analysis of the As K-edge EXAFS data

Sample and model fit	As–O SS			As–Fe SS			As–O1–O2 MS2-1			As–O1–As–O2 MS3-1			As–O1–As–O1 MS3-2			As–O–Fe MS2-2			ΔE	*Res*
	R (Å)	*CN*	σ (Å)	*R* (Å)	*CN*	σ (Å)	*R* (Å)	*CN*	σ (Å)	*R* (Å)	*CN*	σ (Å)	*R* (Å)	*CN*	σ (Å)	*R* (Å)	*CN*	σ (Å)		
Scorodite-1	1.68	4.0	0.04	3.36	4[a]	0.06													9.8	20.2
Scorodite-2	1.68	4.0	0.04	3.36	4[a]	0.06	3.15	12[a]	0.08										10.0	20.5
Scorodite-3	1.68	4.0	0.04	3.36	4[a]	0.06										3.47	8[a]	0.07	10.5	19.6
Scorodite-4	1.68	4.0	0.04	3.36	4[a]	0.06	3.13	12[a]	0.05[b]							3.49	8[a]	0.05[b]	10.5	18.6
Scorodite-5	1.68	4.0	0.04	3.36	4[a]	0.06	3.09	12[a]	0.05[b]	3.34[c]	12[a]	0.05[b]	3.34[c]	4[a]	0.05[b]	3.49	8[a]	0.05[b]	10.5	18.4
6KR-1	1.69	5.3	0.06	3.28	2.0	0.10													9.2	20.2
6KR-2	1.69	5.3	0.06	3.27	1.7	0.10	3.11	12[a]	0.06										9.4	17.9

SS, single scattering path; MS2-1, noncollinear double path; MS3-1, noncollinear triple path; MS3-2, collinear triple paths within the AsO_4 tetrahedron; MS2-2: As–O–Fe double path; ΔE, inner potential correction in eV; *Res*, fit residual defined as $\sum\{|\chi_{exp} - \chi_{fit}|\}/\sum\{|\chi_{exp}|\}$; S_0^2 was fixed at 1.0.

[a] *CN* fixed to the structural value (SS) or to the degeneracy of the path (MS).

[b] Constrained to be identical.

[c] Constrained to be identical.

4. Discussion

4.1. Mineral nomenclature

In this article, we use the term vernadite to describe a turbostratic variety of birnessite, and a structural and compositional analogue to synthetic δ-MnO_2 (Giovanoli et al., 1970; Giovanoli, 1980). Originally, vernadite and birnessite were given two names because the first mineral lacked basal reflections at 7.0–7.2 and 3.5–3.6 Å and, thus, was not regarded to have a layer structure (Chukhrov et al., 1979, 1980, 1987). However, XRD simulations have shown that basal reflection should occur even when the diffracting crystallites average only 2–3 layers (Villalobos et al., 2006). The non-detection of basal reflection in earlier studies may be explained by the poorer performance of older diffractometers, or the presence of Fe in the form of ferrihydrite or feroxyhite, as in Fe–vernadite (Manceau and Combes, 1988; Varentsov et al., 1991; Vodyanitskii et al., 2003, 2004). In Fe–vernadite, the Mn and Fe oxides are intermixed on a fine scale (Manceau and Combes, 1988; Manceau et al., 1992), and perhaps epitaxially intergrown (Burns and Burns, 1979), likely as a result of the heterogeneous oxidation of either Fe^{2+} at the phyllomanganate surface or Mn^{2+} at the hydrous Fe oxide surface (Krishnamurti and Huang, 1987; Wehrli, 1990; Stumm, 1997). Since ferrihydrite and feroxyhite do not have a layer structure, the intimate association of Fe nanoparticles with Mn layers probably disrupts the parallelism of the layers, weakening or even extinguishing the basal reflections. In the quartz coatings examined here, the ferrihydrite and vernadite components are not mixed at the nanometer-scale and, consequently, basal reflections are detected.

The term buserite, which designates a 10 Å phyllomanganate with exchangeable cations and an expanding and contracting interlayer spacing (Giovanoli et al., 1975; Giovanoli and Bürki, 1975; Giovanoli and Brütsch, 1979; Tejedor-Tejedor and Paterson, 1979; Golden et al., 1986; Paterson et al., 1986) is not used here because buserite is a two-layer hydrate form of birnessite and vernadite. Today it appears that there is no fundamental structural difference between buserite and its dehydration product and, consequently, the names birnessite (Jones and Milne, 1956) and vernadite (Betekhtin, 1940), which date back to long before buserite, are preferred.

4.2. Chemical and structural heterogeneity of natural vernadite

Natural vernadite is a complex mineral despite its apparent simplicity in elemental composition and chemistry (Mn is the only major cation and is uniquely tetravalent) and structure (i.e., stacking of octahedral layers). In addition to having a nanometer dimension due to its high defect density, in most samples no two particles are identical. The extent of this heterogeneity is apparent in the XRD data. As mentioned in Section 3, XRD cannot distinguish between intra- and inter-particle heterogeneity because 7 and 10 Å diffracting crystallites can exist either within the same particle or else as distinct particles. Nonetheless, indirect evidence for inter-particle heterogeneity exists when there is mixed-layering of 10 Å layers in the 7 Å component and of 7 Å layers in the 10 Å component. The probability is slim that two particles have the same number of diffracting layers (i.e., size of coherent scattering domains in the *c* direction), degree of interstratification (i.e., fraction of each layer type), and layer sequence. Thus, the heterogeneity of individual crystallites makes the sample inhomogeneous at higher scales, and adequate quantification of the structure of the bulk sample requires a large number of particles, as is necessary for powder XRD. Sample 3SP is the most heterogeneous and can be viewed as an assemblage of different particles which exhibit a quasi-continuous distribution in the proportions of 10 and 7 Å layers. In this highly defective sample, the centroid of the broad 001 reflection is at ~8 Å. Similar peak position and broad asymmetrical lineshape were reported for a 10 Å manganate coating on pebble surfaces taken from a streambed after heating to 110 °C (Tani et al., 2003) and also for the biogenic phyllomanganate (δ-MnO_2) produced by the spores of *Bacillus* SG-1, either after heating at 100–150 °C (Mandernack et al., 1995) or aging for 77 days (Bargar et al., 2005). These results can be interpreted as an interstratification of 10 Å layers having varying degrees of collapsibility and, consequently, chemical composition. In support of this structural interpretation, after 77 days of Mn(II) reaction with the spores of *Bacillus* SG-1, the precipitate was a mixture of two phyllomanganate components, one biogenic and another abiotic formed by the oxidation of Mn(II) at the surface of the biogenic oxide.

In general, homoionic layer compounds owe their variability in hydration to variation in the layer charge density (Newman, 1987). They lose their ability to swell when there is either no layer charge, as in talc, or a high layer charge, as in mica, and they exhibit swelling properties in between these two end-member cases. When the layers in a crystallite have different charges a mixed-layer structure is formed, as in the clay mineral illite–smectite (Reynolds, 1989). Therefore, by analogy with clay minerals, and since 2SP and 6KR are nearly homoionic (i.e., calcic), the 10 and 7 Å layers presumably have different surface charge density. This interpretation is reinforced by the fact that layer charge heterogeneities also exist in synthetic birnessite (Lanson et al., 2000). In the absence of layer Mn^{3+} cations, the layer charge of birnessite originates from vacant layer octahedra (Gaillot et al., 2003; Villalobos et al., 2006). So, here, the layers are unlikely to have the same amounts and distributions of octahedral vacancies and, hence, the same amounts and distributions of interlayer cations and water molecules. The nature of interlayer species also may vary from layer to layer since the ion selectivity of these compounds depends on the layer charge (Newman, 1987).

The interlayer cationic composition influences the density of interlayer water, and in particular the proportions of di-hydrated and mono-hydrated layers, as demonstrated for phyllosilicates.(Ferrage et al., 2005). Calcium, which has a high ionic potential (2.0) and a highly negative enthalpy of hydration (-1577 ± 10 kJ/mol; Smith, 1977), tends to retain its hydration spheres when located in the interlayer forming mixed mono- and di-hydrated states, as observed here. Fully hydrated Zn, like Ca, is octahedrally coordinated to water with an even more negative enthalpy of hydration (-2046 kJ/mol; Smith, 1977). However, tetrahedrally coordinated Zn^{2+} that is bonded to three surface oxygens has less residual positive charge to be compensated by water molecules and should not retain a second hydration shell as strongly. Therefore, the Ca-rich crystallites are expected to be more hydrated than the ^{IV}Zn-rich crystallites. In support of this hypothesis, samples 2SP and 6KR, with an interlayer Ca/Zn ratio of 44 and 12, respectively, have a much higher proportion of 10 Å particles ($I[d(001)_{10\ Å}]/I[d(001)_{7\ Å}] \approx 2$) than sample 3SP ($I[d(001)_{10\ Å}]/I[d(001)_{7\ Å}] < 1$), with a Ca/Zn ratio of 0.7.

The higher proportion of metals (mostly Zn) in the interlayer of 3SP is evident from the shape of the 100 reflection, which is more symmetrical and has a better defined shoulder at ~2.2 Å than in 2SP and 6KR (Fig. 17). This structural interpretation is supported by calculations, which showed that the lineshape of this reflection is sensitive to the nature, location and amount of cationic species in the interlayer (Villalobos et al., 2006). The broad hump at higher angle is more pronounced in 3SP and is significantly shifted to smaller *d* values (1.66–1.67 Å) relative to its position in the two other samples (1.72–1.73 Å). The modulation of the diffracted intensity in this region of the XRD pattern is sensitive to the position of water molecules (Villalobos et al., 2006).

4.3. Elemental associations and distribution

X-ray microfluorescence showed that Ni, Zn and Ba are associated with Mn and As is associated with Fe. The strong Zn–Mn correlation is clearly visible in 5SP, which has thin lens-like Zn–Mn layers between pure Fe layers. The selective association of Ni, Zn and Ba with Mn oxides on ferromanganese pebble coatings, and of As with Fe oxides has been reported in many other studies (e.g., Nowlan, 1976; Pierce and Moore, 1982; Buckley, 1989; DeVitre et al., 1991; Foster et al., 1998; Jambor and Dutrizac, 1998; Savage et al., 2000; Kneebone et al., 2002; Morin et al., 2002; Strawn et al., 2002; Tani et al., 2003; Utsunomiya et al., 2003; Cances et al., 2005; Frau et al., 2005). The low TMs levels in the two Fe-rich 4SP and 5SP coatings occurred because the concentration of TMs is low at the water works of Emden (4SP) and Lüneburg (5SP), otherwise As would have sorbed on Fe oxides and the toxic metals on Mn oxides. The low amount of Mn in the Fe-rich coatings was not a limiting factor to metal sorption because in 5SP the majority of the Mn layers do not contain Zn. From mineralogical and crystallographic standpoints, more metal could have sorbed onto these samples.

None of the major (Fe, Mn) and trace (Ba, Ni, Zn, and As) elements are uniformly distributed among quartz

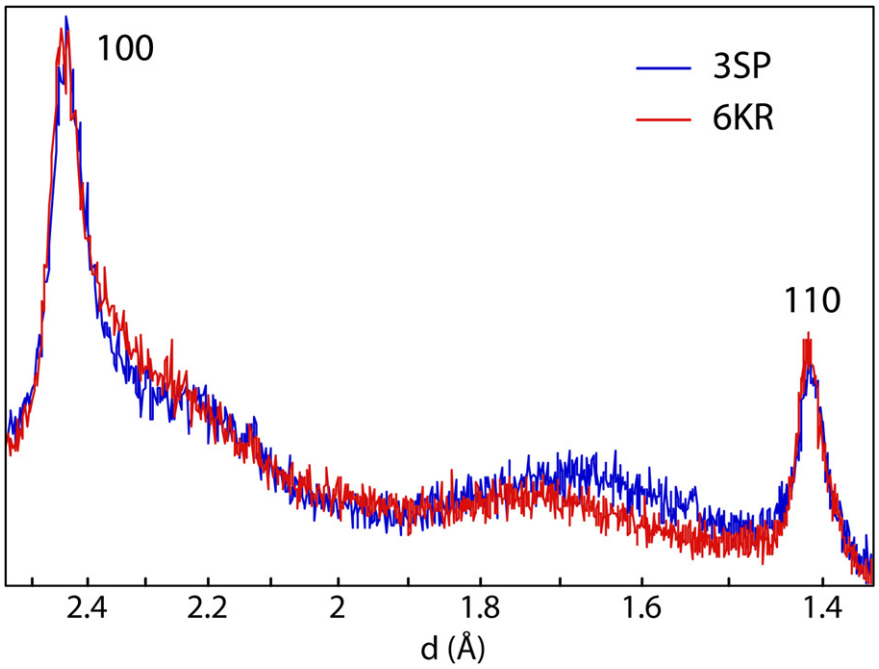

Fig. 17. XRD traces of 3SP and 6KR in the high 2θ-angle region. 2SP has a similar profil as 6KR.

grains from a single sample. Tani et al. (2003) arrived at the same conclusion on chemical heterogeneities based on ICP-MS analyses of coatings on individual submerged pebbles and boulders in streambeds. They reported Mn concentrations from 4.8 to 18 wt% with lesser concentrations of Fe from 3.0 to 9.4 wt%. Here, we showed that major and trace elements are also unevenly distributed at the micrometer-scale at the surface of individual grains. Fe and Mn layers alternate in some, but not all, grains. The first oxide layer in contact with quartz is ferruginous on some grains and manganiferous on other grains, and this variability can occur on a single grain surface. What causes these variable heterogeneities? Alternating Fe- and Mn-rich layers on rock or mineral surfaces are common in nature and considered to reflect redox conditions since the Mn^{4+}/Mn^{2+} couple has a higher redox potential than the Fe^{3+}/Fe^{2+} couple (e.g.,.Hlawatsch et al., 2002). Here, the variations may have been seasonal as shallow waters are depleted in oxygen in the summer and enriched in the winter. Apparent simultaneous formation of Fe and Mn oxides in different regions of a grain or among grains may be explained by micrometer-scale variation of the contact time of solutes with quartz surfaces as a result of preferential flow paths in the micropores of sand beds. This factor may also account for the variability of the TMs/Fe and TMs/Mn ratios at a given depositional time, and for the variability in coating thickness. Some effect of surface heterogeneity of the original quartz grains on the chemical composition of coatings is also possible since silica sand is a pretty heterogeneous material when it is put into service. The origin of the variability of the TMs/Fe and TMs/Mn ratios is probably not structural because according to XRD Fe is speciated only as ferrihydrite and Mn as hexagonal *c*-disordered birnessite. There is no evidence that the affinity of these two phases for TMs varies to the degree of not sorbing any TMs in some regions (blue and green regions in RGB representation) and large quantities in other regions. This discussion on possible physico-chemical factors controlling the formation of the quartz coating does not presuppose their biotic or abiotic origin (Czekalla et al., 1985; Tani et al., 2003; Jessen et al., 2005).

4.4. Structural chemistry of Zn

Our data indicate that in the medium-Zn 6KR sample (Zn/Mn = 0.0138) Zn forms a tridentate corner-sharing tetrahedral complex with three O atoms of the Mn oxide layers at octahedral site vacancies (Fig. 3). In the high-Zn 3SP sample (Zn/Mn = 0.1036), the vacant Mn layer sites are capped by tetrahedral and octahedral Zn, in the proportions 70% ^{IV}Zn + 30% ^{VI}Zn (±10%). The medium-Zn birnessite species has been identified in soil (Isaure et al., 2005) and marine ferromanganese nodules (Marcus et al., 2004b), and a mixed tetrahedral–octahedral Zn–Mn oxide species was identified previously in soil ferromanganese nodules (Manceau et al., 2003). The Zn/Mn ratios of these natural samples were not always available, making direct comparisons difficult. In contrast, the comparison with literature data on Zn sorbed on synthetic birnessite, obtained by chemical or biogenic routes, provides context for Zn coordination as a function of the Zn/Mn ratio obtained in this study.

Zn-sorption on *c*-ordered hexagonal birnessite with layer formula $[{Mn^{4+}}_{0.74}\ {Mn^{3+}}_{0.10}\ vac_{0.17}]$ (vac stands for a vacant site) was studied at pH 4 and within a sorption range of 0.008–0.128 mol Zn mol^{-1} Mn (Drits et al., 2002; Lanson et al., 2002b; Manceau et al., 2002a). At low surface loading (sample ZnBi8, Zn/Mn molar ratio 0.008), 70% Zn was tetrahedral and 30% octahedral. The fraction of octahedrally coordinated species increased with surface loading, reaching 75% at 0.128 mol Zn mol^{-1} Mn. At pH 6.9, biogenic δ-MnO_2 of layer formula $[{Mn^{4+}}_{0.833}, vac_{0.167}]$ produced by *P. putida* sorbed all Zn as a tetrahedral complex at low loading (0.06 mol Zn mol^{-1} Mn), and as a mixture of 37% ^{IV}Zn + 63% ^{VI}Zn (± 10%) at high loading (0.37 mol Zn mol^{-1} Mn) (Toner et al., 2006). These studies show that Zn coordination at vacant layer Mn sites depends on surface-loading in all birnessites examined so far, regardless of their origin. As discussed in Manceau et al. (2002a), the tetrahedral Zn complex probably forms on most undersaturated surface oxygen sites, since the formal charge transferred to a bonded oxygen is $2^+/4 = 0.5$ v.u. in fourfold coordination compared to $2^+/6 = 0.33$ v.u. in sixfold coordination. Thus, the ^{IV}Zn/^{VI}Zn ratio at a given loading depends on the fractional amount of the so-called, high-energy and low-energy surface sites. In the biogenic sample studied by Toner et al. (2006) and in 3SP, the origin of the supplementary surface charge deficit at the high-energy sites is unknown, as these compounds have no layer Mn^{3+} cation (i.e., all O_{layer} atoms at the borders of a vacant Mn site are theoretically equivalent).

4.5. Structural chemistry of Ni

Three Ni surface complexes were identified on δ-MnO_2: an edge-sharing complex at Mn sites in the octahedral layer (^{E}Ni), a triple-corner sharing complex at vacant Mn layer sites in the interlayer (^{TC}Ni), and a double-corner sharing complex at layer edges (^{DC}Ni). The variation of their proportions as a function of pH and surface coverage allows one to better understand how Ni interacts with birnessite. From the compilation of all data available on the structure and surface reactivity of δ-MnO_2, and the bonding environment of Ni at its surface, the following mechanistic description can be proposed:

- At low pH and Ni/Mn = 0.0023, 90 ± 10% of Ni is sorbed as the ^{TC}Ni complex and 10 ± 10% as the ^{E}Ni complex. Since δ-MnO_2 contains 6% vacant Mn layer sites (Villalobos et al., 2006), Ni may migrate from the interlayer to layer sites. A possible explanation for the low fraction of ^{E}Ni is the high activity of protons at low pH, which, in addition to Na and Ni, can balance

the charge deficit (−4.0 v.u.) of the vacancy sites in the manganese layer. This charge is distributed evenly over the six oxygens of an octahedral vacancy with two of the negative charges in the three undersaturated oxygens on each side of the layer. When the concentration of protons is high, the charge deficit is balanced by the sorption of divalent or trivalent cations on one side of the vacancy and one or two protons on the other side (Manceau et al., 1997; Silvester et al., 1997; Lanson et al., 2000, 2002b). This sorption mechanism, which was described previously for Mn^{2+}, Mn^{3+}, Zn^{2+}, and Co^{2+}, probably applies also to Ni^{2+}.

- At low pH and Ni/Mn = 1.07%, all of the spectroscopically detectable Ni is sorbed as the ^{TC}Ni complex. The ^{E}Ni fraction seen at lower surface coverage is no longer detected, meaning that Ni atoms sorbed in the range $0.0023 < Ni/Mn < 0.0107$ remained in the interlayer.
- At low pH and $Ni/Mn > 0.0107$, ^{DC}Ni complex is detected at the expense of the ^{TC}Ni complex.
- At circumneutral pH and $Ni/Mn \leqslant 0.0107$, $55 \pm 10\%$ of Ni is sorbed as the ^{TC}Ni complex and $45 \pm 10\%$ as the ^{E}Ni complex. The higher amount of Ni in layer sites can be explained by the lower activity of protons and the weak affinity of Na for the TC site (i.e., absence of ^{TC}Ni-vac-^{TC}Na pairs).
- At circumneutral pH and $Ni/Mn > 0.0107$, ^{DC}Ni complex is again progressively detected but this time at the expense of both the ^{E}Ni and ^{TC}Ni complexes.

In sample 3SP from the water works, $65 \pm 10\%$ of the Ni atoms occupy interlayer sites and $24 \pm 10\%$ occupy layer sites. There is no evidence for the presence of Ni on layer edges. The ratio of interlayer Ni to layer Mn, calculated from the total Ni/Mn ratio in the solid determined by chemical analysis (0.0093) and from the Ni occupancy at the interlayer site ($65/(65+24) = 0.73$), is $0.0093 \times 0.73 = 0.0068$. This amount is 1/13 of the value of the minimum proportion of vacant layer sites (0.089) estimated from the interlayer composition (cf. Section 3.1). The partitioning of Ni between layer and interlayer sites is influenced by the nature and concentration of all interlayer species. For example, when ^{TC}Ni faces a sodium on the opposite side of the vacancy, the weak strength of the Na–O bond may not prevent Ni from migrating into the vacancy. In contrast, when a vacancy is capped on each side by two divalent cations, or one divalent cation and two protons, the local charge deficit (−4.0 v.u.) is fully balanced and the configuration is stable, as in chalcophanite (^{TC}Zn-vac-^{TC}Zn configuration; Wadsley, 1955). Consequently, the ^{E}Ni/^{TC}Ni ratio in a sample may be an indicator of the pH and composition of the solution or interlayer. In the marine environment, hexagonal birnessite is expected to have a high proportion of ^{E}Ni because seawater is alkaline (pH ~8.3) and the concentration of alkali metals (Na, K) is high. In contrast, the geochemistry of the majority of continental formations (acidic pH, high concentration of alkaline earth divalent cations) is more favorable for the formation of the ^{TC}Ni complex. This is the case for sample 3SP as its interlayer contains 19.08% divalent cations (excluding Ni) and 1.11% monovalent cations in proportion to Mn (Table 2). The presence of ^{TC}Ca (Chukhrov et al., 1985) and ^{TC}Zn complexes may have prevented the migration of Ni into the layer.

Ni does not seem to have a strong chemical preference for either the layer or interlayer site in hexagonal birnessite, as its partitioning appears to depend on the activity of the other chemical species in the interlayer. When there is no interlayer cation, and hence no TC site, as in lithiophorite, Ni occupies only the layer site (Manceau et al., 2002c). In soils, the ^{E}Ni complex is dominant because Ni is associated primarily with lithiophorite, not birnessite (Manceau et al., 2004, 2005). Therefore, the predominance of the ^{E}Ni complex in soils seems to contradict the low selectivity of Ni for either site in birnessite. A possible explanation is the good steric match between Ni^{2+} and Mn^{3+} ($r(Ni^{2+}) = 0.70$ Å, $r(Mn^{3+}) = 0.65$ Å, $r(Mn^{4+}) = 0.54$ Å) and the fact that lithiophorite contains as much as 1/3 Mn^{3+} in its layer. As a result, the strain energy resulting from the Ni^{2+} for Mn substitution is probably lower in lithiophorite than in birnessite. This discussion shows that the affinity of Ni for the layer site also depends on the chemical composition of the octahedral layer. In general, this affinity should be higher in Mn^{3+}-containing phyllomanganates because they have a larger layer dimension ($a = b = 2.925$ Å in lithiophorite; Post and Appleman, 1994) than pure Mn^{4+} phyllomanganates ($a = b = 2.838$ Å in δ-MnO_2; Villalobos et al., 2006).

The preferential uptake of Ni by birnessite, and not ferrihydrite, in the quartz coatings reported here is consistent with results from a detailed study on the fate of nickel in sandy aquifer sediments in Denmark (Larsen and Postma, 1997; Appelo and Postma, 1999; Kjoller et al., 2004). By combining field measurements with laboratory experiments and thermodynamic modeling, these authors concluded that Ni is preferentially sorbed in Mn oxides rather than Fe oxides on the coated sand, and that Ni remained strongly sorbed on the sediment at low pH, but not when the Mn oxide was dissolved by the surface catalyzed oxidation of Fe^{2+} in the aquifer. The strong affinity of Ni for Mn oxides in sandy sediments has been reported in other studies (Young and Harvey, 1992; Tessier et al., 1996), and is interpreted by the formation of a pH-dependent inner-sphere sorption complex (Kjoller et al., 2004). The formation of a weak complex by ion exchange also was considered in the study by Kjoller et al. (2004), but this sorption mechanism failed to reproduce the depth profile of the Ni concentration in the field.

The conclusion published from the field studies and the results presented here calls into question the reality of the outer-sphere complexation of Ni at the δ-MnO_2 surface proposed in a previous study (Trivedi et al., 2001). A difference in data is not the reason for the

diverging interpretations because their spectra are similar to those reported here at low pH and low Ni concentration. Their Fourier transforms also had two main peaks, one at short distance attributed to the nearest O shell at 2.07 Å from solvated Ni and a second at $R + \Delta R \sim 3$ Å attributed to a second hydration shell at 3.35 Å. In the present study, the second peak has been assigned to Mn atoms from the octahedral layer at ~3.50 Å (i.e., ^{TC}Ni complex). To clarify the ambiguity, we Fourier-filtered the second peak of NidBi11-4 and were able to simulate the electronic wave with either an oxygen or a manganese shell (Fig. 18). The phase was reproduced equally by the two models, but not the wave envelope. The experimental wave has a maximum between 6 and 7 $Å^{-1}$, i.e., at a k value typical of backscattering by transition metals. (Teo and Lee, 1979). Instead, oxygen atoms have a scattering amplitude which decreases monotonically over the whole experimental k range. Therefore, according to EXAFS theory only Mn atoms are able to replicate the experimental envelope, which is what the simulations demonstrate. The misfit in amplitude at $k = 3$–4 $Å^{-1}$ in the Ni–Mn model (Fig. 18b) is due mostly to the contribution from higher oxygen shells from the sorbent (~3.4–3.7 Å) (Manceau and Combes, 1988; Schlegel et al., 2001; Villalobos et al., 2006). Part of the missing amplitude can be attributed also to multiple scattering. Therefore, if distant oxygen atoms from some minor fraction of outer-sphere Ni complex contributes to the amplitude at low k, this is at least a third order effect which is beyond the sensitivity of the method.

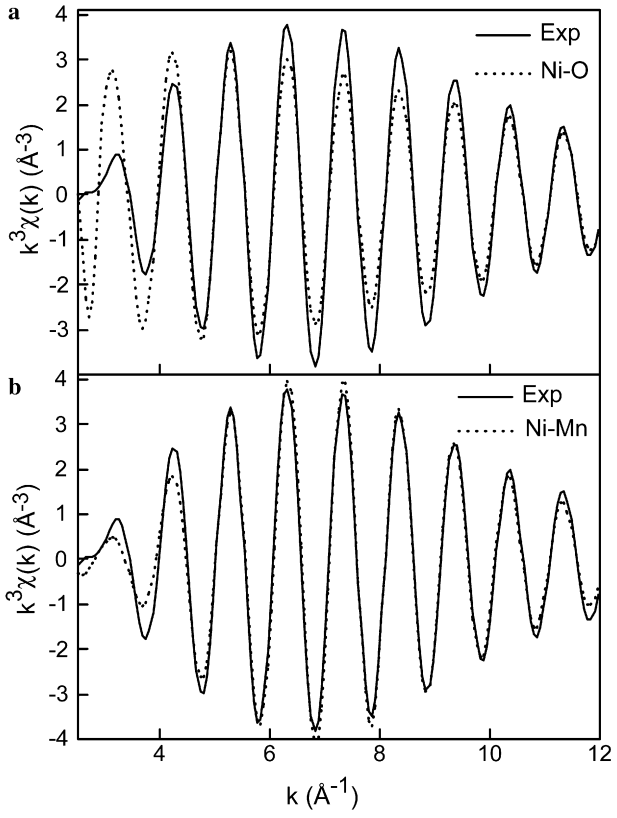

Fig. 18. Inverse Fourier transform of NidBi11-4 in the [2.5–3.6 Å] $R + \Delta R$ interval and spectral simulation with oxygen atoms (outer-sphere complexation model from Trivedi et al., 2001) (a), and manganese atoms (inner-sphere complex) (b).

4.6. Structural chemistry of Ba

This study reveals that EXAFS spectroscopy is sensitive to Ba coordination and site occupation in natural minerals, even when spectra are recorded at room temperature. This finding was far from obvious initially, because thermal disorder at alkaline earth cation sites in sorption samples is generally high, and the detection of the contribution from sorbent cationic shells may require collecting EXAFS spectra at low temperature (Axe et al., 1998, 2000; Sahai et al., 2000; Zhang et al., 2001). In the three studied tectomanganate and phyllomanganate compounds, Ba is sorbed above the empty tetrahedral cavities formed by the O_{layer} atoms from the triads of edge-sharing MnO_6 octahedra. Barium is systematically shifted in the direction of the nearest O_{layer}–O_{layer} edge of the Mn layer over this cavity (Position 1 in Fig. 11) to balance the uneven distribution of O_{layer} charges resulting from Mn^{3+} for Mn^{4+} substitutions (hollandite and triclinic birnessite) and vacant layer Mn octahedra (hexagonal birnessite), but apparently in an amount that depends on the layer charge.

Potassium and calcium are sorbed at similar crystallographic positions as Ba in Ca-exchanged triclinic birnessite (Drits et al., 1998), in high temperature birnessite, $K_{0.231}Mn^{3+}{}_{0.077}$ $(Mn^{4+}{}_{0.885}$ $vac_{0.115})O_2 \cdot 0.60$ H_2O (Gaillot et al., 2003), and in the acid form of δ-MnO_2 (Villalobos et al., 2006). This similarity in position indicates common structural principles for the sorption of alkali and alkaline earth cations on manganates despite differences in chemical properties of the cations or structure and conditions of formation of the manganates. The similarity in position also provides a structural explanation to the high partitioning of cations into Mn oxides at the earth's surface (Kuhn et al., 2003). Our structural results may be extended to radium, since barium is an analogue for radium, a short half-life (ranging from 3.6 days to 1600 years) radioactive product of the decay of uranium and thorium. The geochemical affinity of Ra for Mn oxides is well documented and some authors estimate that 0.5% of Mn oxides in an oxidized aquifer would suffice to control Ra mobility (Herczeg et al., 1988). This affinity has been used in pilot- and full-scale experiments for Ra removal from contaminated waters by manganese green sand (Qureshi and Nelson, 2003). Because of the extremely low amount of Ra in natural solid samples (concentrations related inversely to the half-life), studies on Ra interactions with mineral surfaces have remained of a macroscopic nature (e.g., leaching experiments, sequential filtrations), and no structural investigations have been performed. Our results on Ba shed light on the structural mechanism responsible for the tremendous Ra–Mn oxide partitioning in the environment.

4.7. Structural chemistry of As

The combination of SXRF, XRD, and EXAFS data showed that the main form of As is an As(V) inner-sphere complex sorbed at the surface of ferrihydrite. This result agrees with the well-known affinity of As(V) for the surfaces of iron oxides reported in natural samples (Belzile and Tessier, 1990; Korte, 1991; Bowell, 1994; Foster et al., 1998; La Force et al., 2000; Savage et al., 2000; Pichler et al., 2001; Rancourt et al., 2001; Smedley and Kinniburgh, 2002; Carlson et al., 2002; Morin et al., 2002; Jeong and Lee, 2003; Utsunomiya et al., 2003; Cances et al., 2005). The As complex is coordinated on average to 2 Fe octahedra at 3.27–3.28 Å, compared to 4 Fe at 3.36 Å in scorodite (Table 4). The reduction of interatomic distance is interpreted as a bidentate–binuclear attachment of the arsenate tetrahedra to the apices of two adjacent iron octahedra (i.e., double corner-sharing, DC, linkage) (Waychunas et al., 1993; Moldovan et al., 2003). No bidentate (i.e., edge-sharing, E, linkage) nor monodentate (i.e., single-corner, SC, linkage) mononuclear complex were detected as these configurations yield As–Fe distances of 2.85–2.90 and 3.6 Å, respectively (Waychunas et al., 1993; Manceau, 1995; Fendorf et al., 1997; Morin et al., 2002; Paktunc et al., 2003). The absence of an SC complex is unquestionable because the FTs of the two samples (6KR and 3SP) have weak magnitude in the 3.2–3.4 Å $R + \Delta R$ interval (Fig. 14b). In contrast, examination of the sample FTs alone is inconclusive about the presence of the E complex, because the second FT peak has a composite shape that may arise from a mixture of either E and DC complexes, or the DC complex and multiple scattering paths. When the data are examined in k space, the MS contribution occurs at 4–6 $Å^{-1}$ and the node resulting from the interference between the 2.85–2.90 Å (E complex) and 3.25–3.30 (DC complex) As–Fe waves occurs at 11–13 $Å^{-1}$ (Manceau, 1995). No compelling evidence for the presence of a wave node in the high k region was apparent in our data, indicating the absence of an E complex. In contrast, adding the As–O1–O2 (MS2-1) triangular multiple-scattering path to the spectral fit was necessary and sufficient to replicate the shape of the first oscillation. In scorodite, both the MS2-1 and As–O–Fe (MS2-2) contributions had to be added to reproduce the shape of the first oscillation. In this mineral, multiple scattering involving iron atoms is significant because each As atom is linked to four Fe atoms with approximately the same As–O–Fe dihedral angle (132–136°) (Kitahama et al., 1975; Hawthorne, 1976). The low amplitude of this path in As-sorbed ferrihydrite can be explained by the disruption of the Fe oxide structure at the surface (i.e., lower number of Fe neighbors) and the bonding of As to ligands of different strengths (e.g., O, OH; disorder effect). In both the reference and natural sample the inclusion of MS paths in the model fits did not, or only moderately, modified the As–Fe EXAFS distance. This means that their omission in the data analysis, as often observed in the literature, does not lead to erroneous structural interpretation, even when the amplitude of the As–Fe single-scattering path is weak, as in a sorption complex.

4.8. Implications

The results of this study elucidate how TMs are taken up in Fe–Mn coated sands, which are important natural sorbents in the surface and subsurface, and which are being used more frequently as a low-cost sorbent for wastewater treatment. The high retention capacity of ferromanganese coatings for Ni, Zn and Ba results from the high affinity of these metals for vernadite, to which they selectively bind. In contrast, As is selectively associated with ferrihydrite. Consequently, the removal efficiency of TMs depends on the chemical composition of the coating. Even if As is the only TM to be removed, the presence of vernadite can cause oxidation of As(III) to As(V), which is sorbed more efficiently in natural waters (Manning et al., 1998; Meng et al., 2002).

Although sand coatings can maintain a high sorption capacity in wastewater applications for decades, there is a potential risk of releasing TMs by desorption reactions and transformation or dissolution of the Mn and Fe oxides in response to changing chemical conditions. For example, arsenic can be desorbed if there is sufficient phosphate derived from fertilizers because the two oxyanions compete for the same binding sites on Fe oxides (O'Reilly et al., 2001; Jessen et al., 2005). In contrast, protons should have little effect on the mobility of TMs because the arsenate complex on ferrihydrite and metal cation complexes on vernadite are stable over a large range of pH (Gadde and Laitinen, 1974; Pierce and Moore, 1982). As a case in point, Christensen et al. (1996) showed that Ni is sorbed quantitatively at pH 4 on sandy aquifer sediments, a result which was interpreted by sorption on Mn oxides.(Larsen and Postma, 1997; Kjoller et al., 2004). Ferrihydrite is thermodynamically unstable and recrystallizes with time to more stable phases, mainly goethite. This transformation decreases the surface area, and surface-bound species such as arsenic are mostly expelled during ageing (Houben, 2003). However, ferrihydrite can maintain its reactivity if recrystallization to goethite is inhibited by impurities, such as Si, P, and also Ca (Jambor and Dutrizac, 1998), but only in the absence of vernadite because Ca has a higher affinity for the phyllomanganate. In the presence of Mg, vernadite may transform into todorokite (Golden et al., 1986, 1987), a large tunnel structure tectomanganate with reduced affinity for heavy metals relative to vernadite. Finally, reductive dissolution of vernadite and ferrihydrite may cause a major release of TMs. Since Mn oxides are more reducible than Fe oxides, cations would be released first in anoxic conditions. Also, heterogeneous reduction of Mn oxides under oxidizing conditions may occur by surface catalyzed oxidation of aqueous Fe^{2+} and by organic reductants, such as ascorbic acid (Young and Harvey, 1992).

Acknowledgments

B. Lanson is thanked for fruitful discussions on the XRD section of the manuscript. M.A. Marcus and S. Fakra from the ALS, and J.L. Hazemann and O. Proux from the ESRF are thanked for their assistance during measurements at the two synchrotron facilities. The quartz coating samples were kindly provided by D. Stüben, and the natural As-containing vernadite reference by T. Allard. The final version of the manuscript benefited from the careful reviews by D. Paktunc and two anonymous referees. The ALS and the CNRS, which supports the French-CRG program at ESRF, are acknowledged for the provision of beamtime. This research was funded by the GdR-TRANSMET program from the CNRS. The ALS is supported by the Director, Office of Energy Research, Office of Basic Energy Sciences, Materials Sciences Division of the U.S. Department of Energy, under Contract No. DE-AC02-05CH11231.

Associate editor: Garrison Sposito

References

Allard, T., Ildefonse, P., Beaucaire, C., Calas, G., 1999. Structural chemistry of uranium associated with Si, Al, Fe gels in a granitic uranium mine. *Chem. Geol.* **158**, 81–103.

Almeida, R.M., de Barros Marques, M.I., Gonçalves, M.C., 1994. EXAFS study of Ba and La structural environments in fluorozirconate glasses. *J. Non-Cryst. Solids* **168**, 144–149.

Ankudinov, A.L., Rehr, J.J., 1997. Relativistic calculations of spin-dependent X-ray-absorption spectra. *Phys. Rev.* **B56**, 1712–1716.

Ankudinov, A.L., Ravel, B., Rehr, J.J., Conradson, S.D., 1998. Real space multiple scattering calculation of XANES. *Phys. Rev.* **B58**, 7565–7576.

Appelo, C.A.J., Postma, D., 1999. A consistent model for surface complexation on birnessite and its application to a column experiment. *Geochim. Cosmochim. Acta* **63**, 3039–3048.

Axe, L., Bunker, G.B., Anderson, P.R., Tyson, T.A., 1998. An XAFS analysis of strontium at the hydrous ferric oxide surface. *J. Colloid Interface Sci.* **199**, 44–52.

Axe, L., Tyson, T., Trivedi, P., Morrison, T., 2000. Local structure analysis of strontium sorption to hydrous manganese oxide. *J. Colloid Interface Sci.* **224**, 408–416.

Babel, S., Kurniawan, T.A., 2003. Low-cost adsorbents for heavy metals uptake from contaminated water: a review. *J. Hazard. Mater.* **97**, 219–243.

Bardossy, G., Brindley, G.W., 1978. Rancieite associated with a karstic bauxite deposit. *Am. Miner.* **63**, 762–767.

Bargar, J.R., Brown Jr., G.E., Parks, G.A., 1997. Surface complexation of Pb(II) at oxide–water interfaces: II. XAFS and bond-valence determination of mononuclear and polynuclear Pb(II) sorption products on iron oxides. *Geochim. Cosmochim. Acta* **61**, 2639–2652.

Bargar, J.R., Brown Jr., G.E., Parks, G.A., 1998. Surface complexation of Pb(II) at oxide–water interfaces: III. XAFS determination of Pb(II) and Pb(II)-chloro adsorption complexes on goethite and alumina. *Geochim. Cosmochim. Acta* **62**, 193–207.

Bargar, J.R., Tebo, B.M., Bergmann, U., Webb, S.M., Glatzel, P., Chiu, V.Q., Villalobos, M., 2005. Biotic and abiotic products of Mn(II) oxidation by spores of the marine *Bacillus* sp. strain SG-1. *Am. Miner.* **90**, 143–154.

Belzile, N., Tessier, A., 1990. Interactions between arsenic and iron oxyhydroxides in lacustrine sediments. *Geochim. Cosmochim. Acta* **54**, 103–109.

Betekhtin, A.G., 1940. South Urals manganese deposits as a raw material base for the Magnitogorsk mettallurgic plant. *Trudi Inst. Geol. Scien. Acad. Sci. USSR, Ore deposit Ser.* No 4.

Bilinski, H., Giovanoli, R., Usui, A., Hanzel, D., 2002. Characterization of Mn oxides in cemented streambed crusts from Pinal Creek, Arizona, USA, and in hot-spring deposits from Yuno-Taki falls, Hokkaido, Japan. *Am. Mineral.* **87**, 580–591.

Bose, P., Bose, M.A., Kumar, S., 2002. Critical evaluation of treatment strategies involving adsorption and chelation for wastewater containing copper, zinc and cyanide. *Adv. Environ. Res.* **7**, 179–195.

Bose, P., Sharma, A., 2002. Role of iron in controlling speciation and mobilization of arsenic in subsurface environment. *Water Res.* **36**, 4916–4926.

Bowell, R.J., 1994. Sorption of arsenic by iron oxides and oxyhydroxides in soils. *Appl. Geochem.* **9**, 279–286.

Brown Jr., G.E., Sturchio, N.C., 2002. An overview of synchrotron radiation applications to low temperature geochemistry and environmental science. In: Fenter, P.A., Rivers, M.L., Sturchio, N.C., Sutton, S.R. (Eds.), *Applications of Synchrotron Radiation in Low-Temperature Geochemistry and Environmental science*, vol. 49. Mineralogical Society of America, pp. 1–116.

Buatier, M.D., Guillaume, D., Wheat, C.G., Hervé, L., Adatte, T., 2004. Mineralogical characterization and genesis of hydrothermal Mn oxides from the flank of the Juan the Fuca Ridge. *Am. Miner.* **89**, 1807–1815.

Buckley, A., 1989. An electron microprobe investigation of the chemistry of ferromanganese coatings on freshwater sediments. *Geochim. Cosmochim. Acta* **53**, 115–124.

Burns, R.G., Burns, V.M., 1979. Manganese oxides. In: Burns, R.G. (Ed.), *Marine Minerals*. Mineralogical Society of America, pp. 1–46.

Byrne, R.H., 2002. Inorganic speciation of dissolved elements in seawater: the influence of pH on concentration ratios. *Geochem. Trans.* **3**, 11–16.

Byström, A., Byström, A.M., 1950. The crystal structure of hollandite, the related manganese oxide minerals, and α-MnO_2. *Acta Cryst.* **3**, 146–154.

Cances, B., Juillot, F., Morin, G., Laperche, V., Alvarez, L., Proux, O., Hazemann, J.L., Brown Jr., G.E., Calas, G., 2005. Evidence of As(V) association with iron oxyhydroxides in a contaminated soil at a former arsenical pesticide processing plant. *Environ. Sci. Technol.* **39**, 9398–9405.

Carlson, L., Bigham, J.M., Schwertmann, U., Kyek, A., Wagner, F., 2002. Scavenging of As from acid mine drainage by schwertmannite and ferrihydrite: a comparison with synthetic analogues. *Environ. Sci. Technol.* **36**, 1712–1719.

Carpenter, R.H., Pope, T.A., Smith, R.L., 1975. Fe–Mn oxide coatings in stream sediment geochemical surveys. *J. Geochem. Explor.* **4**, 349–363.

Chao, T.T., Theobald, J., 1976. The significance of secondary iron and manganese oxides in geochemical exploration. *Econ. Geol.* **71**, 1560–1569.

Charlet, L., Manceau, A., 1992. X-ray absorption spectroscopic study of the sorption of Cr(III) at the oxide/water interface. II Adsorption, coprecipitation and surface precipitation on ferric hydrous oxides. *J. Colloid Interface Sci.* **148**, 25–442.

Cheremisinoff, P., 1995. *Handbook of Water and Wastewater Treatment Technology*. Marcel Dekker, New York (Basel).

Christensen, T.H., Lehmann, N., Jackson, T., Holm, P.E.J., 1996. Cadmium and nickel distribution coefficients for sandy aquifer materials. *J. Contam. Hydrol.* **24**, 75–84.

Chukhrov, F.V., Gorshkov, A.I., Berezovskaya, V.V., Sivtsov, A.V., 1979. Contributions to the mineralogy of authigenic manganese phases from marine manganese deposits. *Mineral. Deposita* **14**, 249–261.

Chukhrov, F.V., Gorshkov, A.I., Rudnitskaya, Y.S., Berezovskaya, V.V., Sivtsov, A.V., 1980. Manganese minerals in clays: a review. *Clays Clay Miner.* **28**, 154–346.

Chukhrov, F.V., Sakharov, B.A., Gorshkov, A.I., Drits, V.A., Dikov, Y.P., 1985. Crystal structure of birnessite from the Pacific Ocean. *Inter. Geol. Rev.* **27**, 1082–1088 (translated from Investiya Akademie Nauk, SSSR, Seriya Geologicheskaya, 8, 66–73) 27, 1082–1088.

Chukhrov, F.V., Drits, V.A., Gorshkov, A.I., Sakharov, B.A., Dikov, Y.P., 1987. Structural models for vernadite. *Int. Geol. Rev.* **29**, 1337–1347.

Czekalla, C., Mevius, W., Hanert, H., 1985. Quantitative removal of iron and manganese by microorganisms in rapid sand filters (in situ investigations). *Water Supply* **3**, 111–123.

Deb, A., Bergmann, U., Cramer, S.P., Cairns, E.J., 2006. Local structure of $LiNi_{0.5}Mn_{0.5}O_2$ cathode material probed by in situ X-ray absorption spectroscopy. *J. Appl. Phys.* **99**, 063701.

Defontaine, G., Michot, L., Bihannic, I., Ghanbaja, J., Briois, V., 2003. Synthesis of NiGa layered double hydroxides. A combined extended X-ray absorption fine structure, small-angle X-ray scattering, and transmission electron microscopy study. 1. Hydrolysis in the pure Ni^{2+} system. *Langmuir* **19**, 10588–10600.

DeVitre, R., Belzile, N., Tessier, A., 1991. Speciation and adsorption of arsenic on diagenetic iron oxyhydroxides. *Limnol. Oceanogr.* **36**, 1480–1485.

Drits, V.A., Tchoubar, C., 1990. *X-ray Diffraction by Disordered Lamellar Structures: Theory and Applications to Microdivided Silicates and Carbons*. Springer Verlag, Berlin.

Drits, V.A., Sakharov, B.A., Salyn, A.L., Manceau, A., 1993. Structural model for ferrihydrite. *Clay Mineral.* **28**, 185–208.

Drits, V.A., Gorshkov, A.I., Sakharov, B.A., Salyn, A.L., Manceau, A., 1995. Ferrihydrite and its phase transitions during heating in the oxidizing and reducing environments. *Lithol. Mineral Resour.* **1**, 68–75 (translated from Litologiya, 1, 76–84, 1995).

Drits, V.A., Silvester, E., Gorshkov, A.I., Manceau, A., 1997. The structure of synthetic monoclinic Na-rich birnessite and hexagonal birnessite. Part 1. Results from X-ray diffraction and selected area electron diffraction. *Am. Mineral.* **82**, 946–961.

Drits, V.A., Lanson, B., Gorshkov, A.I., Manceau, A., 1998. Sub- and super-structure of four-layer Ca-exchanged birnessite. *Am. Mineral.* **83**, 97–118.

Drits, V.A., Lanson, B., Bougerol-Chaillout, C., Gorshkov, A.I., Manceau, A., 2002. Structure of heavy metal sorbed birnessite. Part 2. Results from electron diffraction. *Am. Mineral.* **87**, 1646–1661.

Duff, M.C., Hunter, D.B., Triay, I.R., Bertsch, P.M., Reed, D.T., Sutton, S.R., Shea-McCarthy, G., Kitten, J., Eng, P., Chipera, S.J., Vaniman, D.T., 1999. Mineral associations and average oxidation states of sorbed Pu on tuff. *Environ. Sci. Technol.* **33**, 2163–2169.

Duff, M.C., Hunter, D.B., Triay, I.R., Bertsch, P.M., Kitten, J., Vaniman, D.T., 2001. Comparison of two micro-analytical methods for detecting the spatial distribution of sorbed Pu on geologic materials. *J. Cont. Hydrol.* **47**, 211–218.

Ertl, A., Pertlik, F., Prem, M., Post, J.E., Kim, S.J., Brandstatter, F., Schuster, R., 2005. Rancieite crystals from Friesach, Carinthia, Austria. *Eur. J. Mineral.* **17**, 163–172.

Fendorf, S., Eick, M.J., Grossl, P., Sparks, D.L., 1997. Arsenate and chromate retention mechanisms on goethite. 1. Surface structure. *Environ. Sci. Technol.* **31**, 315–320.

Ferrage, E., Lanson, B., Sakharov, B.A., Drits, V.A., 2005. Investigation of smectite hydration properties by modeling experimental X-ray diffraction patterns: Part I. Montmorillonite hydration properties. *Am. Mineral.* **90**, 1358–1374.

Foster, A.L., Brown Jr., G.E., Tingle, T.N., Parks, G.A., 1998. Quantitative arsenic speciation in mine tailings using X-ray absorption spectroscopy. *Am. Miner.* **83**, 553–568.

Foster, A.L., Brown Jr., G.E., Parks, G.A., 2003. X-ray absorption fine structure study of As(V) and Se(IV) sorption complexes on hydrous Mn oxides. *Geochim. Cosmochim. Acta* **67**, 1937–1953.

Frau, F., Rossi, A., Ardau, C., Biddau, R., Da-Pelo, S., Atzei, D., Licheri, C., Cannas, C., Capitani, G., 2005. Determination of arsenic speciation in complex environmental samples by the combined use of TEM and XPS. *Microchim. Acta* **151**, 189–201.

Gadde, R.R., Laitinen, H.A., 1974. Studies of heavy metals adsorption by hydrous iron and manganese oxides. *Anal. Chem.* **46**, 2022–2026.

Gaillot, A.C. 2002. *Caractérisation structurale de la birnessite : Influence du protocole de synthèse*. Ph.D. Thesis, Univ. J. Fourier, Grenoble, France, p. 353.

Gaillot, A.C., Flot, D., Drits, V.A., Burghammer, M., Manceau, A., Lanson, B., 2003. Structure of synthetic K-rich birnessites obtained by high-temperature decomposition of $KMnO_4$. I. Two-layer polytype from a 800 °C experiment. *Chem. Mater.* **15**, 4666–4678.

Gilmore, E.A., Evans, G.J., Ho, M.D., 2001. Radiochemical assessment of the readsorption and redistribution of lead in the SM&T sequential extraction procedure. *Anal. Chim. Acta* **439**, 139–151.

Giovanoli, R., Stähli, E., Feitknecht, W., 1970. Über oxidhydroxide des vierwertigen mangans mit schichtengitter. 2. Mangan(III)–manganat(IV). *Helv. Chim. Acta* **53**, 454–464.

Giovanoli, R., Bürki, P., 1975. Comparison of X-ray evidence of marine manganese nodules and non-marine manganese ore deposits. *Chimia* **29**, 266–269.

Giovanoli, R., Bürki, P., Giuffredi, S., Stumm, W., 1975. Layer structured manganese oxide hydroxides. IV: The buserite groups; structure stabilization of transition elements. *Chimia* **29**, 517–520.

Giovanoli, R., Brütsch, R., 1979. Uber oxihydroxide des Mn(IV) mit schichtengitter. 5. Mitteilung: Stöchiometrie, austauschverhalten und die rolle bei der bildung von tiefsee-mangankonkretionen. *Chimia* **33**, 372–376.

Giovanoli, R., 1980. Vernadite is random-stacked birnessite. *Mineral. Deposita* **15**, 251–253.

Glover, E.D., 1977. Characterization of a marine birnessite. *Am. Miner.* **62**, 278–285.

Goldberg, E.D., 1954. Marine geochemistry. I. Chemical scavengers of the sea. *J. Geol.* **62**, 249–265.

Golden, D.C., Chen, C.C., Dixon, J.B., 1986. Synthesis of todorokite. *Science* **231**, 717–719.

Golden, D.C., Chen, C.C., Dixon, J.B., 1987. Transformation of birnessite to buserite, todorokite, and manganite under mild hydrothermal treatment. *Clays Clay Miner.* **35**, 271–280.

Gupta, V.K., Saini, V.K., Jain, N., 2005. Adsorption of As(III) from aqueous solutions by iron oxide-coated sand. *J. Colloid Interface Sci.* **288**, 55–60.

Hansel, C.M., Fendorf, S., Sutton, S., Newville, M., 2001. Characterization of Fe plaque and associated metals on the roots of mine-waste impacted aquatic plants. *Environ. Sci. Technol.* **35**, 3863–3868.

Hawthorne, F.C., 1976. The hydrogen positions in scorodite. *Acta Cryst.* **B32**, 2891–2992.

Herczeg, A.L., Simpson, H.J., Anderson, R.F., Trier, R.M., Mathieu, G.G., Deck, B.L., 1988. Uranium and radium mobility in groundwaters and brines within the Delaware Basin, southeastern New Mexico, U.S.A. *Chem. Geol.* **72**, 181–196.

Hlawatsch, S., Kersten, M., Garbe-Schönberg, C.D., Lechtenberg, F., Manceau, A., Tamura, N., Kulik, D.A., Harff, J., Suess, E., 2001. Trace metal fluxes to ferromanganese nodules from the western Baltic Sea as a record for long-term environmental changes. *Chem. Geol.* **182**, 697–710.

Hlawatsch, S., Neumann, T., van den Berg, C.M.G., Kersten, M., Harff, J., Suess, E., 2002. Fast-growing, shallow-water ferro-manganese nodules from the western Baltic Sea: origin and modes of trace element incorporation. *Mar. Geol.* **182**, 373–387.

Holland, K.L., Walker, J.R., 1996. Crystal structure modeling of a highly disordered potassium birnessite. *Clays Clay Mineral.* **44**, 744–748.

Houben, G.J., 2003. Iron oxide incrustrations in wells. Part 1: genesis, mineralogy and geochemistry. *Appl. Geochem.* **18**, 927–939.

Hu, P.Y., Hsieh, Y.H., Chen, J.C., Chang, C.Y., 2004a. Adsorption of divalent manganese ion on manganese-coated sand. *J. Water Supply Res. Technol.* **53**, 151–158.

Hu, P.Y., Hsieh, Y.H., Chen, J.C., Chang, C.Y., 2004b. Characteristics of manganese-coated sand using SEM and EDAX analysis. *J. Colloid Interface Sci.* **272**, 308–313.

Hudson-Edwards, K.A., 2000. Heavy metal-bearing Mn oxides in river channel and floodplain sediments. In: Cotter-Howells, J.D., Campbell,

L.S., Valsami-Jones, E., Batchelder, M. (Eds.), *Environmental Mineralogy: Microbial Interactions, Anthropogenic Influences, Contaminated Land and Waste Management*, vol. 9. Mineralogical Society of Great Britain and Irland.

Isaure, M.P., Laboudigue, A., Manceau, A., Sarret, G., Tiffreau, C., Trocellier, P., Hazemann, J.L., Chateigner, D., 2002. Quantitative Zn speciation in a contaminated dredged sediment by μPIXE, μSXRF, EXAFS spectroscopy and principal component analysis. *Geochim. Cosmochim. Acta* **66**, 1549–1567.

Isaure, M.P., Manceau, A., Geoffroy, N., Laboudigue, A., Tamura, N., Marcus, M.A., 2005. Zinc mobility and speciation in soil covered by contaminated dredged sediment using micrometer-scale and bulk-averaging X-ray fluorescence, absorption and diffraction techniques. *Geochim. Cosmochim. Acta* **69**, 1173–1198.

Jambor, J.L., Dutrizac, J.E., 1998. Occurrence and constitution of natural and synthetic ferrihydrite, a widespread iron oxyhydroxide. *Chem. Rev.* **98**, 2549–2585.

Jenne, E.A. 1968. Controls on Mn, Fe, Co, Ni, Cu and Zn concentrations in soils and water: the significant role of hydrous Mn and Fe oxides. In: Gould, R.F. (Ed.), *Trace Inorganics in Water*, vol. 73, Am. Chem. Soc. Adv. Chem. Ser., pp. 337–387.

Jeong, G.Y., Lee, B.Y., 2003. Secondary mineralogy and microtextures of weathered sulfides and manganoan carbonates in mine waste-rock dumps, with implications for heavy-metal fixation. *Am. Mineral.* **88**, 1933–1942.

Jessen, S., Larsen, F., Koch, C.B., Arvin, E., 2005. Sorption and desorption of arsenic to ferrihydrite in a sand filter. *Environ. Sci. Technol.* **39**, 8045–8051.

Jones, L.H.P., Milne, A., 1956. Birnessite, a new manganese oxide mineral from Aberdeenshire, Scotland. *Mineral Mag.* **31**, 283–288.

Kirpichtchikova, T., Manceau, A., Spadini, L., Panfili, F., Marcus, M.A., Jacquet, T., 2006. Speciation and solubility of heavy metals in contaminated soil using X-ray microfluorescence, EXAFS spectroscopy, chemical extraction, and thermodynamic modelling. *Geochim. Cosmochim. Acta* **70**, 2163–2190.

Kitahama, K., Kiriyama, R., Baba, Y., 1975. Refinement of the crystal structure of scorodite. *Acta Cryst.* **B31**, 322–324.

Kjoller, C., Postma, D., Larsen, F., 2004. Groundwater acidification and the mobilization of trace metals in a sandy aquifer. *Environ. Sci. Technol.* **38**, 2829–2835.

Kneebone, P.E., O'Day, P.A., Jones, N., Hering, J.G., 2002. Deposition and fate of arsenic in iron- and arsenic-enriched reservoir sediments. *Environ. Sci. Technol.* **36**, 381–386.

Korte, N., 1991. Naturally occurring arsenic in groundwaters of the midwestern United States. *Environ. Geol. Water Sci.* **18**, 137–141.

Koschinsky, A., Hein, J.R., 2003. Uptake of elements from seawater by ferromanganese crusts: solid-phase associations and seawater speciation. *Mar. Geol.* **198**, 331–351.

Krishnamurti, G.S.R., Huang, P.M., 1987. The catalytic role of birnessite in the transformation of iron. *Can. J. Soil Sci.* **67**, 533–543.

Kuhn, T., Bostick, B.C., Koschinsky, A., Halbach, P., Fendorf, S., 2003. Enrichment of Mo in hydrothermal Mn precipitates: possible Mo sources, formation process and phase associations. *Chem. Geol.* **199**, 29–43.

Kundu, S., Gupta, A.K., 2005. Analysis and modeling of fixed bed column operations on As(V) removal by adsorption onto iron oxide-coated cement (IOCC). *J. Colloid Interface Sci.* **290**, 52–60.

La Force, M.J., Hansel, C.M., Fendorf, S., 2000. Arsenic speciation, seasonal transformations, and co-distribution with iron in a mine waste-influenced palustrine emergent wetland. *Environ. Sci. Technol.* **34**, 3937–3943.

Lanson, B., Drits, V.A., Silvester, E.J., Manceau, A., 2000. Structure of H-exchanged hexagonal birnessite and its mechanism of formation from Na-rich monoclinic buserite at low pH: New data from X-ray diffraction. *Am. Mineral.* **85**, 826–835.

Lanson, B., Drits, V.A., Feng, Q., Manceau, A., 2002a. Crystal structure determination of synthetic Na-rich birnessite: evidence for a triclinic one-layer cell. *Am. Mineral.* **87**, 1662–1671.

Lanson, B., Drits, V.A., Gaillot, A.C., Silvester, E., Plançon, A., Manceau, A., 2002b. Structure of heavy metal sorbed birnessite. Part I. Results from X-ray diffraction. *Am. Mineral.* **87**, 1631–1645.

Larsen, F., Postma, D., 1997. Nickel mobilization in a groundwater well field: release by pyrite oxidation and desorption from manganese oxides. *Environ. Sci. Technol.* **31**, 2589–2595.

Leroux, F., Le Gal La Salle, A., Guyomard, D., Piffard, Y., 2001. Interleaved oxovanadium cations in the rancieite manganese oxide δ-MnO_2. *J. Mater. Chem.* **11**, 652–656.

Leupin, O.X., Hug, S.J., 2005. Oxidation and removal of arsenic (III) from aerated groundwater by filtration through sand and zero-valent iron. *Water Res.* **39**, 1729–1740.

Li, X.L., Pan, G., Qin, Y.W., Hu, T.D., Wu, Z.Y., Xie, Y.N., 2004. EXAFS studies on adsorption–desorption reversibility at manganese oxide–water interfaces. II. Reversible adsorption of zinc on δ-MnO_2. *J. Colloid Interface Sci.* **271**, 35–40.

Li, Y.H., 1982. Interelement relationship in abyssal Pacific ferromanganese nodules and associated pelagic sediments. *Geochim. Cosmochim. Acta* **46**, 1053–1060.

Liu, F., Colombo, C., Adamo, P., He, J.Z., Violante, A., 2002. Trace elements in manganese-iron nodules from a Chinese Alfisol. *Soil Sci. Soc. Am. J.* **66**, 661–670.

Malinowski, E.R., 1977. Determination of the number of factors and the experimental error in a data matrix. *Anal. Chem.* **49**, 612–617.

Malinowski, E.R., 1978. Theory of error for target factor analysis with applications to mass spectrometry and nuclear magnetic resonance spectrometry. *Anal. Chim. Acta* **103**, 354–359.

Manceau, A., Combes, J.M., 1988. Structure of Mn and Fe oxides and oxyhydroxides: a topological approach by EXAFS. *Phys. Chem. Mineral.* **15**, 283–295.

Manceau, A., Charlet, L., 1992. X-ray absorption spectroscopic study of the sorption of Cr(III) at the oxide/water interface. I Molecular mechanism of Cr(III) oxidation on Mn oxides. *J. Colloid Interface Sci.* **148**, 443–458.

Manceau, A., Gorshkov, A.I., Drits, V.A., 1992. Structural chemistry of Mn, Fe, Co, and Ni in Mn hydrous oxides. II. Information from EXAFS spectroscopy, electron and X-ray diffraction. *Am. Mineral.* **77**, 1144–1157.

Manceau, A., 1995. The mechanism of anion adsorption on Fe oxides: evidence for the bonding of arsenate tetrahedra on free $Fe(O,OH)_6$ edges. *Geochim. Cosmochim. Acta* **59**, 3647–3653.

Manceau, A., Boisset, M.C., Sarret, G., Hazemann, J.L., Mench, M., Cambier, P., Prost, R., 1996. Direct determination of lead speciation in contaminated soils by EXAFS spectroscopy. *Environ. Sci. Technol.* **30**, 1540–1552.

Manceau, A., Drits, V.A., Silvester, E., Bartoli, C., Lanson, B., 1997. Structural mechanism of Co(II) oxidation by the phyllomanganate, Na-buserite. *Am. Mineral.* **82**, 1150–1175.

Manceau, A., Lanson, B., Schlegel, M.L., Hargé, J.C., Musso, M., Eybert-Bérard, L., Hazemann, J.L., Chateigner, D., Lamble, G.M., 2000. Quantitative Zn speciation in smelter-contaminated soils by EXAFS spectroscopy. *Am. J. Sci.* **300**, 289–343.

Manceau, A., Lanson, B., Drits, V.A., 2002a. Structure of heavy metal sorbed birnessite. Part III. Results from powder and polarized extended X-ray absorption fine structure spectroscopy. *Geochim. Cosmochim. Acta* **66**, 2639–2663.

Manceau, A., Marcus, M.A., Tamura, N., 2002b. Quantitative speciation of heavy metals in soils and sediments by synchrotron X-ray techniques. In: Fenter, P.A., Rivers, M.L., Sturchio, N.C., Sutton, S.R. (Eds.), *Applications of Synchrotron Radiation in Low-Temperature Geochemistry and Environmental Science*, vol. 49. Mineralogical Society of America, pp. 341–428.

Manceau, A., Tamura, N., Marcus, M.A., MacDowell, A.A., Celestre, R.S., Sublett, R.E., Sposito, G., Padmore, H.A., 2002c. Deciphering Ni sequestration in soil ferromanganese nodules by combining X-ray fluorescence, absorption and diffraction at micrometer scales of resolution. *Am. Mineral.* **87**, 1494–1499.

Manceau, A., Tamura, N., Celestre, R.S., MacDowell, A.A., Geoffroy, N., Sposito, G., Padmore, H.A., 2003. Molecular-scale speciation of Zn and Ni in soil ferromanganese nodules from loess soils of the Mississippi basin. *Environ. Sci. Technol.* **37**, 75–80.

Manceau, A., Marcus, M.A., Tamura, N., Proux, O., Geoffroy, N., Lanson, B., 2004. Natural speciation of Zn at the micrometer scale in a clayey soil using X-ray fluorescence, absorption, and diffraction. *Geochim. Cosmochim. Acta* **68**, 2467–2483.

Manceau, A., Tommaseo, C., Rihs, S., Geoffroy, N., Chateigner, D., Schlegel, M., Tisserand, D., Marcus, M.A., Tamura, N., Chen, Z.S., 2005. Natural speciation of Mn, Ni and Zn at the micrometer scale in a clayey paddy soil using X-ray fluorescence, absorption, and diffraction. *Geochim. Cosmochim. Acta* **69**, 4007–4034.

Mandernack, K.W., Post, J., Tebo, B.M., 1995. Manganese mineral formation by bacterial spores of the marine *Bacillus*, strain SG-1: evidence for the direct oxidation of Mn(II) to Mn(IV). *Geochim. Cosmochim. Acta* **59**, 4393–4408.

Manning, B.A., Fendorf, S.E., Goldberg, S., 1998. Surface structures and stability of arsenic(III) on goethite: spectroscopic evidence for inner-sphere complexes. *Environ. Sci. Technol.* **32**, 2383–2388.

Manning, B.A., Fendorf, S.E., Bostick, B.C., Suarez, D.L., 2002. Arsenic(III) oxidation and arsenic(V) adsorption reactions on synthetic birnessite. *Environ. Sci. Technol.* **36**, 976–981.

Mansour, A.N., Melendres, C.A., 1998. Analysis of X-ray absorption spectra of some nickel oxycompounds using theoretical standards. *J. Phys. Chem.* **A102**, 65–81.

Marcus, M.A., MacDowell, A.A., Celestre, R., Manceau, A., Miller, T., Padmore, H.A., Sublett, R.E., 2004a. Beamline 10.3.2 at ALS: a hard X-ray microprobe for environmental and materials sciences. *J Synchrotron Radiat* **11**, 239–247.

Marcus, M.A., Manceau, A., Kersten, M., 2004b. Mn, Fe, Zn and As speciation in a fast-growing ferromanganese marine nodule. *Geochim. Cosmochim. Acta* **68**, 3125–3136.

Matocha, C.J., Elzinga, E.J., Sparks, D.L., 2001. Reactivity of Pb(II) at the Mn(III,IV) (oxyhydr)oxide–water interface. *Environ. Sci. Technol.* **35**, 2967–2972.

McCarty, D.K., Moore, J.N., Marcus, W.A., 1998. Element association in an acid mine drainage iron oxide precipitate; comparison of selective extractions. *Appl. Geochem.* **13**, 165–176.

McKenzie, R.M., 1989. Manganese oxides and hydroxides. In: Dixon, J.B., Weed, S.B. (Eds.), *Minerals in Soil Environments*. Soil Science Society of America, Madison, pp. 439–465.

Meng, X., Korfiatis, G.P., Bang, S., Bang, K.W., 2002. Combined effects of anions on arsenic removal by iron hydroxides. *Toxicol. Lett.* **133**, 103–111.

Miura, H., 1989. The crystal structure of Hollandite. *Mineral. J.* **13**, 119–129.

Moldovan, B.J., Jiang, D.T., Hendry, M.J., 2003. Mineralogical characterization of arsenic in uranium mine tailings precipitated from iron-rich hydrometallurgical solutions. *Environ. Sci. Technol.* **37**, 873–879.

Morin, G., Ostergren, J.D., Juillot, F., Ildefonse, P., Calas, G., Brown Jr., G.E., 1999. XAFS determination of the chemical form of lead in smelter-contaminated soils and mine tailings: Importance of adsorption processes. *Am. Mineral.* **84**, 420–434.

Morin, G., Juillot, F., Ildefonse, P., Calas, G., Samama, J.C., Chevallier, P., Brown Jr., G.E., 2001. Mineralogy of lead in a soil developed on a Pb-mineralized sandstone (Largentière, France). *Am. Mineral.* **86**, 92–104.

Morin, G., Lecocq, D., Juillot, F., Calas, G., Ildefonse, P., Belin, S., Briois, V., Dillmann, P., Chevallier, P., Gauthier, C., Sole, A., Petit, P.E., Borensztajn, S., 2002. EXAFS evidence of sorbed arsenic(V) and pharmacoside rite in a soil overlying the Echassieres geochemical anomaly, Allier, France. *Bull. Soc. Géol. France* **173**, 281–291.

Newcombe, R.L., Hart, B.K., Moller, G., 2006. Arsenic removal from water by moving bed active filtration. *J. Environ. Eng.* **132**, 5–12.

Newman, A.C.D., 1987. Chemistry of clays and clay minerals. *Mineralogical Society*.

Neaman, A., Mouele, F., Trolard, F., Bourrie, G., 2004. Improved methods for selective dissolution of Mn oxides: applications for studying trace element associations. *Appl. Geochem.* **19**, 973–979.

Nowlan, G.A., 1976. Concretionary manganese-iron oxides in streams and their usefulness as a sample medium for geochemical prospecting. *J. Geochem. Explor.* **6**, 193–210.

O'Reilly, S., Strawn, D.G., Sparks, D.L., 2001. Residence time effects on arsenate adsorption/desorption mechanisms on goethite. *Soil Sci. Soc. Am. J.* **65**, 67–77.

Ostergren, J.D., Brown Jr., G.E., Parks, G.A., Tingle, T.N., 1999. Quantitative lead speciation in selected mine tailings from Leadville, CO. *Environ. Sci. Technol.* **33**, 1627–1636.

Paktunc, D., Foster, A.L., Laflamme, G., 2003. Speciation and characterization of arsenic in Ketza river mine tailings using X-ray absorption spectroscopy. *Environ Sci. Technol.* **37**, 2067–2074.

Paktunc, D., Foster, A., Heald, S., Laflamme, G., 2004. Speciation and characterization of arsenic in gold ores and cyanidation tailings using X-ray absorption spectroscopy. *Geochim. Cosmochim. Acta* **68**, 969–983.

Palumbo, B., Bellanca, A., Neri, R., Roe, M.J., 2001. Trace metal partitioning in Fe–Mn nodules from Sicilian soils, Italy. *Chem. Geol.* **173**, 257–269.

Pandya, K.I., 1994. Multiple-scattering effects in X-ray-absorption fine structure: chromium in a tetrahedral configuration. *Phys. Rev.* **B50**, 15509–15515.

Paterson, E., Clark, D.R., Russell, J.D., Swaffield, R., 1986. Cation exchange in synthetic manganates: I. Alkylammonium exchange in a synthetic phyllomanganate. *Clay Mineral.* **21**, 949–956.

Peacock, C.L., Sherman, D.M., 2004. Vanadium(V) adsorption onto goethite (α-FeOOH) at pH 1.5–12: a surface complexation model based on *ab initio* molecular geometries and EXAFS spectroscopy. *Geochim. Cosmochim. Acta* **68**, 1723–1733.

Pichler, T., Hendry, M.J., Hall, G.E.M., 2001. The mineralogy of arsenic in uranium mine tailings at the Rabbit Lake in-pit Facility, northern Saskatchewan, Canada. *Environ. Geol.* **40**, 495–506.

Pierce, M., Moore, C., 1982. Adsorption of arsenite and arsenate on amorphous iron hydroxide. *Water Res.* **16**, 1247–1253.

Post, J.E., Appleman, D.E., 1988. Chalcophanite, $ZnMn_3O_7{:}3H_2O$: new crystal-structure determination. *Am. Mineral.* **73**, 1401–1404.

Post, J.E., Appleman, D.E., 1994. Crystal structure refinement of lithiophorite. *Am. Mineral.* **79**, 370–374.

Post, J.E., 1999. Manganese oxide minerals: crystal structures and economic and environmental significance. *Proc. Natl. Acad. Sci. USA* **96**, 3447–3454.

Proux, O., Nassif, V., Prat, A., Ulrich, O., Lahera, E., Biquard, X., Menthonnex, J.J., Hazemann, J.L., 2006. Feedback system of a liquid-nitrogen-cooled double-crystal monochromator: design and performances. *J Synchrotron Radiat* **13**, 59–68.

Przybylowicz, W.J., Mesjasz-Przybylowicz, J., Pineda, C.A., Churms, C.L., Ryan, C.G., Prozesky, V.M., Frei, R., Slabbert, J.P., Padayachee, J., Reimold, W.U., 2001. Elemental mapping using proton-induced X-rays. *X-ray Spectrom.* **30**, 156–163.

Qureshi, N., Nelson, S., 2003. Radium removal by HMO and manganese greensand. *J. Am. Water Works Assoc.* **95**, 101–108.

Rancourt, D.G., Fortin, D., Pichler, T., Thibault, P.J., Lamarche, G., Morris, R.V., Mercier, P.H.J., 2001. Mineralogy of a natural As-rich hydrous ferric oxide coprecipitate formed by mixing of hydrothermal fluid and seawater: Implications regarding surface complexation and color banding in ferrihydrite deposits. *Am. Mineral.* **86**, 834–851.

Ressler, T., 1998. WinXAS: a program for X-ray absorption spectroscopy data analysis under MS-Windows. *J Synchrotron Radiat* **5**, 118–122.

Ressler, T., Wong, J., Roos, J., Smith, I., 2000. Quantitative speciation of Mn-bearing particulates emitted from autos burning (methylcyclopentadienyl)manganese tricarbonyl-added gasolines using XANES spectroscopy. *Environ. Sci. Technol.* **34**, 950–958.

Reynolds Jr., R.C., 1989. Diffraction by small and disordered crystals. In: Bish, D.L., Post, J.E. (Eds.), *Modern Powder Diffraction*, vol. 20. Mineralogical Society of America, pp. 145–181.

Roberts, D.R., Scheinost, A.C., Sparks, D.L., 2002. Zinc speciation in a smelter-contaminated soil profile using bulk and microscopic techniques. *Environ. Sci. Technol.* **36**, 1742–1750.

Robinson, G.D., 1993. Major-element chemistry and micro-morphology of Mn-oxide coatings on stream alluvium. *Appl. Geochem.* **8**, 633–642.

Sahai, N., Carroll, S.A., Roberts, S., O'Day, P.A., 2000. X-ray absorption spectroscopy of strontium(II) coordination. II. Sorption and precipitation at kaolinite, amorphous silica, and goethite surfaces. *J. Colloid Interface Sci.* **222**, 198–212.

Savage, K.S., Tingle, T.N., O'Day, P.A., Waychunas, G.A., Bird, D.K., 2000. Arsenic speciation in pyrite and secondary weathering phases, Mother Lode Gold District, Tuolumne County, California. *Appl. Geochem.* **15**, 1219–1244.

Schlegel, M.L., Manceau, A., Charlet, L., Hazemann, J.L., 2001. Adsorption mechanism of Zn on hectorite as a function of time, pH, and ionic strength. *Am. J. Sci.* **301**, 798–830.

Schwertmann, U., Pfab, G., 1994. Structural vanadium in synthetic geothite. *Geochim. Cosmochim. Acta* **58**, 4349–4352.

Sherman, D.M., Randall, S.R., 2003. Surface complexation of arsenic(V) to iron(III) (hydr)oxides: Structural mechanism from *ab initio* molecular geometries and EXAFS spectroscopy. *Geochim. Cosmochim. Acta* **67**, 4223–4230.

Silvester, E., Manceau, A., Drits, V.A., 1997. The structure of synthetic monoclinic Na-rich birnessite and hexagonal birnessite. Part 2. Results from chemical studies and EXAFS spectroscopy. *Am. Mineral.* **82**, 962–978.

Smedley, P.L., Kinniburgh, D.G., 2002. A review of the source, behaviour and distribution of arsenic in natural waters. *Appl. Geochem.* **17**, 517–568.

Smith, D.W., 1977. Ionic hydration enthalpies. *J. Chem. Educ.* **54**, 540–541.

Spadini, L., Manceau, A., Schindler, P.W., Charlet, L., 1994. Structure and stability of Cd^{2+} surface complexes on ferric oxides. I. Results from EXAFS spectroscopy. *J. Colloid Interface Sci.* **168**, 73–86.

Strawn, D., Doner, H., Zavarin, M., McHugo, S., 2002. Microscale investigation into the geochemistry of arsenic, selenium and iron in soil developed in pyritic shale materials. *Geoderma* **108**, 237–257.

Stumm, W., 1997. Catalysis of redox processes by hydrous oxide surfaces. *Croat. Chem. Acta* **70**, 71–93.

Sutton, S.R., Bertsch, P.M., Newville, M., Rivers, M., Lanzirotti, A., Eng, P., 2002. Microfluorescence and microtomography analyses of heterogeneous earth and environmental materials. In: Fenter, P.A., Rivers, M.L., Sturchio, N.C., Sutton, S.R. (Eds.), *Applications of Synchrotron Radiation in Low-Temperature Geochemistry and Environmental Science*, vol. 49. Mineralogical Society of America, pp. 429–478.

Tani, Y., Miyata, N., Iwahori, K., Soma, M., Tokuda, S.I., Seyama, H., Theng, B.K.G., 2003. Biogeochemistry of manganese oxide coatings on pebble surfaces in the Kikukawa River System, Shizuoka, Japan. *Appl. Geochem.* **18**, 1541–1554.

Taylor, R.M., McKenzie, R.M., Norrish, K., 1964. The mineralogy and chemistry of manganese in some Australian soils. *Aust. J. Soil Res.* **2**, 235–248.

Taylor, R.M., McKenzie, R.M., 1966. The association of trace elements with manganese minerals in Australian soils. *Aust. J. Soil Res.* **4**, 29–39.

Tejedor-Tejedor, M.I., Paterson, E., 1979. Reversibility of lattice collapse in synthetic buserite. In: Mortland, M.M., Farmer, V.C. (Eds.), *Proceedings of the International Clay Conference*, 1978, pp. 501–508.

Teo, B., Lee, P.A., 1979. *Ab initio* calculation of amplitude and phase functions for extended X-ray absorption fine structure spectroscopy. *J. Am. Chem. Soc.* **101**, 2815–2822.

Teo, B.K., 1986. *EXAFS: Basic Principles and Data Analysis*. Springer-Verlag, Berlin.

Tessier, A., Fortin, D., Belzile, N., Devitre, R.R., Leppard, G.G., 1996. Metal sorption to diagenetic iron and manganese oxyhydroxides and associated organic matter: Narrowing the gap between field and laboratory measurements. *Geochim. Cosmochim. Acta* **60**, 387–404.

Thirunavukkarasu, O.S., Viraraghavan, T., Subramanian, K.S., 2001. Removal of arsenic in drinking water by iron oxide-coated sand and ferrihydrite—Batch studies. *Water Qual. Res. J. Canada* **36**, 55–70.

Thirunavukkarasu, O.S., Viraraghavan, T., Subramanian, K.S., 2003. Arsenic removal from drinking water using iron oxide-coated sand. *Water Air Soil Poll.* **142**, 95–111.

Toner, B., Manceau, A., Webb, S.M., Sposito, G., 2006. Zinc sorption to biogenic hexagonal–birnessite particles within a hydrated bacterial biofilm. *Geochim. Cosmochim. Acta* **70**, 27–43.

Tournassat, C., Charlet, L., Bosbach, D., Manceau, A., 2002. Arsenic(III) oxidation by birnessite and precipitation of manganese(II) arsenate. *Environ. Sci. Technol.* **36**, 493–500.

Tressaud, A., Demortain, G., Tanguy, B., Portier, J., Hagenmuller, P., 1989. EXAFS study of hyperquenched amorphous fluorides belonging to the $Ba_{1-x}Mn_xF_2$ system. *J. Non-Crystall. Sol.* **109**, 114–120.

Trivedi, P., Axe, L., Tyson, T., 2001. XAS studies of Ni and Zn sorbed to hydrous manganese oxide. *Environ. Sci. Technol.* **35**, 4515–4521.

Trolard, F., Bourrie, G., Jeanroy, E., Herbillon, A.J., Martin, H., 1995. Trace metals in natural iron oxides from laterites: a study using selective kinetic extraction. *Geochim. Cosmochim. Acta* **59**, 1285–1297.

Usui, A., 1979. Nickel and copper accumulations as essential elements in 10-Å manganite of deep-sea manganese nodules. *Nature* **279**, 411–413.

Usui, A., Mita, N., 1995. Geochemistry and mineralogy of a modern buserite deposit from a hot spring in hokkaido, Japan. *Clays Clay Mineral.* **43**, 116–127.

Usui, A., Bau, M., Yamazaki, T., 1997. Manganese microchimneys buried in the Central Pacific pelagic sediments: evidence of intraplate water circulation? *Mar. Geol.* **141**, 269–285.

Utsunomiya, S., Peters, S.C., Blum, J.D., Ewing, R.C., 2003. Nanoscale mineralogy of arsenic in a region of New Hampshire with elevated As-concentrations in the groundwater. *Am. Miner.* **88**, 1844–1852.

Vaishya, R.C., Gupta, S.K., 2003. Coated sand filtration: an emerging technology for water treatment. *J. Water Supply Res. Technol.* **52**, 299–306.

Vaishya, R.C., Gupta, S.K., 2004. Modeling arsenic(V) removal from water by sulfate modified iron-oxide coated sand separation. *Sci. Technol.* **39**, 645–666.

van Oort, F., Jongmans, A.G., Citeau, L., Lamy, I., Chevallier, P., 2006. Microscale Zn and Pb distribution patterns in subsurface soil horizons: an indication for metal transport dynamics. *Eur. J. Soil Sci.* **57**, 154–166.

Vaniman, D.T., Chipera, S.J., Bish, D.L., Duff, M.C., Hunter, D.B., 2002. Crystal chemistry of clay-Mn oxide associations in soils, fractures, and matrix of the Bandelier Tuff, Pajarito Mesa, New Mexico. *Geochim. Cosmochim. Acta* **66**, 1349–1374.

Varentsov, I.M., Drits, V.A., Gorshkov, A.I., Sivtsov, A.V., Sakharov, B.A., 1991. Me-Fe oxyhydroxide crusts from Krylov Sea mount (Eastern Atlantic): Mineralogy, geochemistry and genesis. *Marin. Geol.* **96**, 53–70.

Villalobos, M., Toner, B., Bargar, J., Sposito, G., 2003. Characterization of the manganese oxide produced by *Pseudomonas putida* strain MnB1. *Geochim. Cosmochim. Acta* **67**, 2649–2662.

Villalobos, M., Bargar, J., Sposito, G., 2005. Mechanisms of Pb(II) sorption on a biogenic manganese oxide. *Environ. Sci. Technol.* **39**, 569–576.

Villalobos, M., Lanson, B., Manceau, A., Toner, B., Sposito, G., 2006. Structural model for the biogenic Mn oxide produced by *Pseudomonas putida*. *Am. Mineral.* **91**, 489–502.

Vodyanitskii, Y.N., Lesovaya, S.N., Sivtsov, A.V., 2003. Iron hydroxidogenesis in forest and steppe soils of the Russian Plain. *Eur. Soil Sci.* **36**, 420–429.

Vodyanitskii, Y.N., Vasilev, A.A., Lesovaya, S.N., Sataev, E.F., Sivtsov, A.V., 2004. Formation of manganese oxides in soils. *Eur. Soil Sci.* **37**, 572–584.

Voegelin, A., Pfister, S., Scheinost, A.C., Marcus, M.A., Kretzschmar, R., 2005. Changes in zinc speciation in field soil after contamination with zinc oxide. *Environ. Sci. Technol.* **39**, 6616–6623.

Wadsley, A.D., 1955. The crystal structure of chalcophanite, $ZnMn_3O_7.3H_2O$. *Acta Cryst.* **8**, 1165–1172.

Waychunas, G.A., Rea, B.A., Fuller, C.C., Davis, J.A., 1993. Surface chemistry of ferrihydrite: Part 1. EXAFS studies of the geometry of coprecipitated and adsorbed arsenate. *Geochim. Cosmochim. Acta* **57**, 2251–2269.

Wehrli, B., 1990. Redox reactions of metal ions at mineral surfaces. In: Stumm, W. (Ed.), *Aquatic Chemical Kinetics*. Wiley, pp. 311–336.

Young, L.B., Harvey, H.H., 1992. The relative importance of manganese and iron oxides and organic matter in the sorption of trace metals by superficial lake sediments. *Geochim. Cosmochim. Acta* **56**, 1175–1186.

Yuan, T., Hu, J.Y., Ong, S.L., Fang, Q.F., Ng, W.J., 2002. Arsenic removal from household drinking water by adsorption. *J. Environ. Sci. Health* **A37**, 1721–1736.

Zhang, P.C., Brady, P.V., Arthur, S.E., Zhou, W.Q., Sawyer, D., Hesterberg, D.A., 2001. Adsorption of barium(II) on montmorillonite: an EXAFS study. *Coll. Surf. Physicochem. Engineer. Aspects* **190**, 239–249.